Precision measurement of parity nonconservation in cesium

C.S. Wood, S.C. Bennett, J.L. Roberts, D. Cho, and C.E. Wieman

Abstract: The measurement of parity nonconservation (PNC) in atomic cesium is discussed in detail. With a spin-polarized atomic beam, this experiment achieves a fractional uncertainty of 0.35% in the measurement of the PNC amplitude for the transition between the 6S and 7S states of cesium, the lowest uncertainty of atomic PNC to date. By comparing the PNC amplitude on two hyperfine transitions, we measure for the first time the nuclear-spin-dependent contribution that arises from the nuclear anapole moment. A major portion of this paper describes the characterization and elimination of systematic errors.

PACS Nos.: 32.80.Ys, 11.30.Er, 12.15.Ji, 32.10.Dk

Résumé: Nous analysons en détail la mesure de la non-conservation de la parité (NCP) dans le césium atomique. Utilisant un faisceau atomique avec polarisation du spin, cette expérience réussit à atteindre une incertitude fractionnaire de 0.35% pour la mesure de la NCP dans la transition entre les états 6S et 7S du césium, la plus basse imprécision jamais atteinte en NCP. En comparant l'amplitude NCP de deux transitions hyperfines, nous mesurons pour la première fois la conribution du spin nucléaire qui est due au moment anapolaire du noyau. Une partie importante de cet article est consacrée à la caractérisation et à l'élimination des erreurs systématiques.
[Traduit par la rédaction]

1. Introduction

Over the past 24 years, there have been increasingly precise measurements of parity nonconservation (PNC) in atoms [1–7]. The primary incentive for these measurements has been to test the standard model of elementary particle physics at low energy. Specifically, this standard model predicts the existence of a parity-violating, weak neutral current interaction between atomic electrons and quarks. The effect of this PNC interaction is to slightly mix ($\sim 10^{-11}$) the S and P states in the atom. This mixing induces a small, electric dipole (E1) transition amplitude between states of the same parity, such as the 6S and 7S states of cesium.

Atomic PNC measurements determine a set of model-independent, electron–quark, electroweak, coupling constants that differ from those probed by high-energy experiments [8,9]. Thus, increasing the precision of atomic PNC measurements provides a unique improved test for "new physics" beyond the standard model. High-precision atomic PNC measurements also offer a different approach to exploring

Received March 7, 1998. Accepted December 18, 1998.

C.S. Wood, S.C. Bennett, J.L. Roberts, D. Cho, and C.E. Wieman.[1] JILA, University of Colorado and National Institute of Standards and Technology, and Department of Physics, University of Colorado, Boulder, CO 80309-0440, U.S.A.

[1] Corresponding author: **Telephone:** (303) 492-6963, **FAX:** (303) 492-5235, **e-mail:** cwieman@jila.colorado.edu

 © 1999 NRC Canada

the effects of parity violation in atomic nuclei through measurement of the nuclear anapole moment, which was done for the first time in this work.

The existence of the anapole moment was predicted in 1957 [10]; it was expected to result from a combination of parity violation and electric charges. More recently, the nuclear anapole moment was examined in the context of atomic PNC [11] and predicted to give a small, nuclear-spin-dependent, second-order correction term to the predicted PNC transition amplitude. Moreover, it was recognized that since this correction term would depend on the nuclear spin, it could be determined by the difference in the PNC transition amplitudes for different atomic hyperfine transitions. However, estimates of the size of this correction term have varied widely because of uncertainties about the basic nuclear parity-violating force [12, 13]. Thus, it was recognized that in addition to providing direct evidence for the existence of an anapole moment, measurement of such a difference in PNC transition amplitudes for different hyperfine transitions would provide valuable information on the basic nuclear parity-violating force.

To test the standard model, we must compare our measured value of atomic PNC with the corresponding value predicted by the standard model. Prediction of this value requires precise knowledge of the mass of the Z boson, presently known to 77 parts per million, which is sufficiently accurate for this purpose. Prediction of this value also requires knowledge of atomic structure, the accuracy of which depends on the particular atom. The (heavy) atom with the most accurately known structure is cesium, because as an alkali atom it has a single valence electron outside a tightly bound core.

In 1974, the Bouchiats [1] recognized that the forbidden transition between the 6S and 7S states of cesium was a good candidate for observing PNC effects, for not only was atomic theory relatively accurate for these states, but the available dye-laser technology at that time was sufficient to produce light at the transition wavelenghth (540 nm) and cesium was convenient to work with. Since then, the situation for cesium has only improved. A plethora of accurate measurements exist that can be used to test atomic theory, and diode laser technology allows manipulation of the cesium hyperfine states and magnetic sublevels. PNC was first measured in cesium by the Paris group with a fractional uncertainty of about 20% [14–16]. This was subsequently improved to about 12% by the Paris group [15, 16] and then 2% by the Boulder group [2, 17].

Conceptually, our present experiment is similar to our two previous experiments [2, 17]. As a beam of Cs atoms passes through a region of mutually perpendicular electric and magnetic fields, a laser beam excites the highly forbidden 6S–7S transition. By reversing either the direction of one of the fields or the handedness of the laser polarization, we reverse the handedness of this region. Since parity-violating interactions cause a small contribution to the 6S–7S transition rate that depends on the handedness of this region, we detect parity violation as the modulation of the 6S–7S transition rate that is synchronous with each of these reversals.

The main improvements of our present experiment over our previous experiments include more 540 nm light, a spin-polarized cesium beam [18–20], and a more efficient detection method. These modifications result in an increase in signal-to-noise by a factor of 7, and thus a corresponding increase in the precision of our measurement. However, this new level of precision also reveals the presence of many new systematic errors. Thus, the majority of our experimental effort here is devoted to characterizing and eliminating these new systematic errors so that the uncertainty in our final result is predominantly statistical. This characterization and elimination of systematic errors required the accumulation of twenty times more data than did the measurement of the PNC transition amplitude!

2. Theory

In all the cesium atomic PNC measurements to date, including our present measurement, the small PNC transition amplitude, A_{PNC}, is measured by a Stark-interference technique [21]. In this technique, an electric field is applied, which induces a transition amplitude, A_{E1}, that is parity-allowed and larger (typically 5 to 6 orders of magnitude) than A_{PNC}. The interference between these two transition amplitudes

©1999 NRC Canada

Fig. 1. Relevant cesium atom energy levels, showing the hyperfine states split by a magnetic field. The case of an initial $m = 3$ sublevel of the 6S $F = 3$ state is shown. This initial state is prepared with two diode lasers that optically pump all the atoms in the $F = 3$ and 4 levels into this initial sublevel. A dye laser then excites these initial-state atoms to the 7S $m = 4$ sublevel. Since a large fraction of the resulting 7S atoms relax to the previously emptied 6S $F = 4$ level, we use this level to detect atoms that have undergone the 6S–7S transition. Specifically, a probe laser drives a cycling transition between this level and a $6P_{3/2}$ hyperfine state. We also measure PNC for three other initial (F, m) sublevels: (3, −3), (4, 4), and (4, −4).

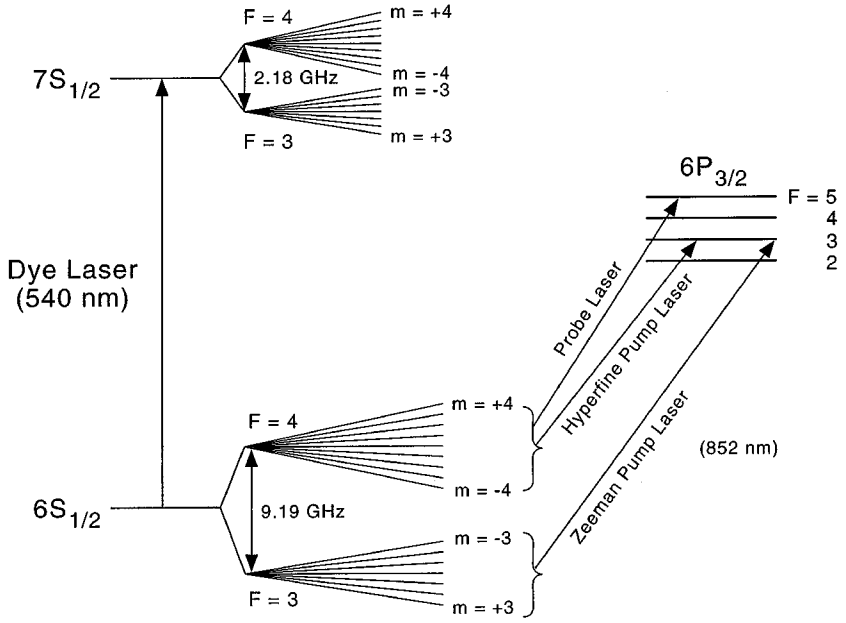

is measured and from that A_{PNC} is determined.

We consider the excitation of a cesium atom from the 6S state to the 7S state by a dye-laser beam, as shown in Fig. 1, in the presence of mutually perpendicular static electric and magnetic fields. Under these conditions, three transition amplitudes between the 6S and 7S states are relevant: the magnetic dipole ($M1$) transition amplitude A_{M1}, which is very small due to the change in principal quantum number; the parity-violating electric-dipole ($E1_{\mathrm{PNC}}$) transition amplitude A_{PNC}, which is 20 000 times smaller than the $M1$ amplitude; and the "Stark-induced" electric-dipole $E1_{\mathrm{Stark}}$ transition amplitude A_{Stark}, which is induced by our applied DC electric field and so scales with the intensity of that field.

We now review previous calculations of these three transition amplitudes, restate the resulting formula for the transition rate for our experimental configuration, and conclude with a discussion of the Zeeman spectrum.

2.1. Transition amplitudes

For an isolated cesium atom with only Coulomb interactions, the electric-dipole transition from the 6S to the 7S state is forbidden by parity conservation. However, the presence of weak neutral currents causes states of opposite parity to mix; thus a small amount of the P state mixes into the 6S and 7S states. In the presence of the oscillating electric field $\boldsymbol{\epsilon}$ of a dye laser, this mixing in turn results in a

©1999 NRC Canada

small, parity-violating, electric dipole transition amplitude, $A_{\rm PNC}$, between the two S states:

$$A_{\rm PNC}(F, m \to F', m') = \sum_{n''} \left\{ \frac{\langle n'SF'm' \mid H^{\dagger}_{\rm PNC} \mid n''P\rangle\langle n''P \mid -e\boldsymbol{\epsilon}\cdot\boldsymbol{r} \mid nSFm\rangle}{E_{n'S} - E_{n''P}} + \frac{\langle n'SF'm' \mid -e\boldsymbol{\epsilon}\cdot\boldsymbol{r} \mid n''P\rangle\langle n''P \mid H_{\rm PNC} \mid nSFm\rangle}{E_{nS} - E_{n''P}} \right\}$$
$$= i{\rm Im}(E1_{\rm PNC})\boldsymbol{\epsilon}\cdot\langle F'm' \mid \boldsymbol{\sigma} \mid Fm\rangle \tag{1}$$

where $H_{\rm PNC}$ is the parity-nonconserving Hamiltonian [1] and, in the second expression, the radial integrals have been incorporated into the constant $E1_{\rm PNC}$ [1]. This amplitude can be re-expressed with the vector components in Cartesian coordinates:

$$\begin{aligned} A_{\rm PNC}(F, m \to F', m') \quad &= \quad i{\rm Im}(E1_{\rm PNC})\epsilon_z C^{F'm'}_{Fm}\delta_{m,m'} \\ &\quad + i{\rm Im}(E1_{\rm PNC})(\pm\epsilon_x + i\epsilon_y)C^{F'm'}_{Fm'\pm1}\delta_{m,m'\pm1} \end{aligned} \tag{2}$$

where the $C^{F'm'}_{Fm}$ factors are combinations of Clebsch–Gordan coefficients, which are tabulated in the Appendix of ref. 17.

To obtain an observable that is first order in this amplitude, we apply a DC electric field, $\boldsymbol{E}$, which also mixes the S and P states. This applied DC electric field induces an additional, much stronger, electric-dipole transition, the "Stark-induced" transition, between these perturbed states, with an amplitude $A_{\rm Stark}$ given by

$$A_{\rm Stark}(F, m \to F', m') = \sum_{n,J,F'',m''} \frac{\langle 7SF'm' \mid -e\boldsymbol{E}\cdot\boldsymbol{r} \mid nP_JF''m''\rangle\langle nP_JF''m'' \mid -e\boldsymbol{\epsilon}\cdot\boldsymbol{r} \mid 6SFm\rangle}{E_{7S} - E_{nP_J}} + \frac{\langle 7SF'm' \mid -e\boldsymbol{\epsilon}\cdot\boldsymbol{r} \mid nP_JF''m''\rangle\langle nP_JF''m'' \mid -e\boldsymbol{E}\cdot\boldsymbol{r} \mid 6SFm\rangle}{E_{6S} - E_{nP_J}} \tag{3}$$

The Bouchiats [1] have shown that this expression can be separated into terms that involve a change in F and terms that do not

$$A_{\rm Stark}(F, m \to F', m') = \alpha\boldsymbol{E}\cdot\boldsymbol{\epsilon}\delta_{F,F'}\delta_{m,m'} + i\beta(\boldsymbol{E}\times\boldsymbol{\epsilon})\cdot\langle F'm' \mid \boldsymbol{\sigma} \mid Fm\rangle \tag{4}$$

where the coefficients α and β are the scalar and tensor "transition polarizabilites", respectively, analogous to the pure electric polarizabilites. In value, $|\alpha/\beta| \approx 10$. We can express this equation in a form similar to that of (2):

$$\begin{aligned} A_{\rm Stark}(F, m \to F'm') = \alpha\boldsymbol{E}\cdot\boldsymbol{\epsilon}\delta_{F,F'}\delta_{m,m'} + i\beta(\boldsymbol{E}\times\boldsymbol{\epsilon})_z C^{F'm'}_{Fm}\delta_{m,m'} \\ + [\pm i\beta(\boldsymbol{E}\times\boldsymbol{\epsilon})_x C^{F'm'}_{Fm'\pm1} - \beta(\boldsymbol{E}\times\boldsymbol{\epsilon})_y C^{F'm'}_{Fm'\pm1}]\delta_{m,m'} \end{aligned} \tag{5}$$

The presence of the oscillating magnetic field of the dye laser, $\boldsymbol{B}_{ac}$, induces a magnetic dipole ($M1$) transition between the 6S and 7S states, with an amplitude A_{M1} given by

$$A_{M1}(F, m \to F', m') = \mu_{\rm B}\langle 7SF'm' \mid \boldsymbol{\sigma}\cdot\boldsymbol{B}_{ac} \mid 6SFm\rangle = M(\widehat{k}\times\boldsymbol{\epsilon})\cdot\langle F'm' \mid \boldsymbol{\sigma} \mid Fm\rangle \tag{6}$$

where $\mu_{\rm B}$ is the Bohr magneton and $\boldsymbol{\sigma}$ is the Pauli spin operator. In the second expression, the radial integrals have been incorporated into the constant M, and we have used Maxwell's equations to replace the oscillating magnetic field of the laser with the corresponding oscillating electric field $\boldsymbol{\varepsilon}$ and wave vector $\boldsymbol{k}$. Although this $M1$ amplitude vanishes to lowest order between states of different principle quantum number, small relativistic effects and the hyperfine interaction prevent it from entirely vanishing [1,22]. Expressing this equation in the form of (2), we get

$$A_{M1}(F, m \to F', m') = M\{(\widehat{k}\times\boldsymbol{\epsilon})_z C^{F'm'}_{Fm}\delta_{m,m'} + [\pm(\widehat{k}\times\boldsymbol{\epsilon})_x + i(\widehat{k}\times\boldsymbol{\epsilon})_y]C^{F'm'}_{Fm'\pm1}\delta_{m,m'\pm1}\} \tag{7}$$

©1999 NRC Canada

Fig. 2. The coordinate system in the interaction region. The electric field $\boldsymbol{E}$ is along $\hat{x}$, the magnetic field $\boldsymbol{B}$ along $\hat{z}$. The dye-laser beam is elliptically polarized, with ϵ_z the component of polarization along the z axis and ϵ_I the component along the x axis (so labeled to emphasize that its phase is imaginary relative to that of ϵ_z).

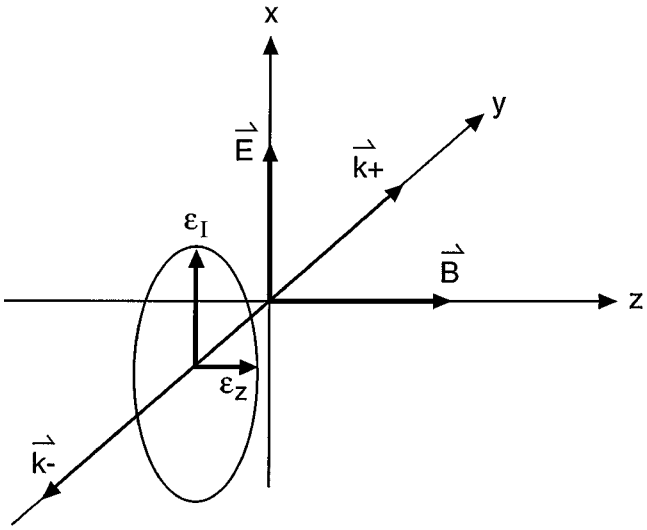

2.2. Transition rate for our experimental configuration

The transition rate R, due to these three amplitudes, is given by

$$R = |A_{\text{Stark}} + A_{M1} + A_{\text{PNC}}|^2 \tag{8}$$

Though A_{Stark} is independent of the handedness of the region (which is defined by the direction of the electric field, the magnetic field, and the circular polarization of the laser), A_{PNC} is not. Thus the interference term between these two amplitudes will change sign with any reversal in handedness. Since A_{E1} is much larger than A_{PNC}, we expect to see a DC signal (due to $|A_{\text{Stark}}|^2$) that has a small oscillation (due to $2A_{\text{Stark}}A_{\text{PNC}}$) synchronous with any reversal in handedness.

We choose our experimental configuration to maximize the interference between the PNC and Stark-induced transition amplitudes, thus maximizing the oscillation of the signal. The coordinate system is shown in Fig. 2, where a dye-laser beam excites the transition from the initial 6S state to the 7S state in a region of mutually perpendicular electric and magnetic fields. We define the y axis to be along the direction of propagation, $\boldsymbol{k}$, of the laser beam. We adjust the orientation of the electric field, $\boldsymbol{E}$, so that it is perpendicular to the beam. The x axis is then along the direction of $\boldsymbol{E}$. Formally, it is defined to be along the direction of the reversing component of $\boldsymbol{E}$ in the plane perpendicular to the laser propagation direction. Any other components of the electric field are nonzero only because of misalignments. The z direction is then defined as the perpendicular to these x and y axes, and we adjust the direction of the magnetic field $\boldsymbol{B}$ and the atomic beam so that they lie along this z axis. To excite the 6S–7S transition, we choose the polarization of the dye laser so that the parity-conserving amplitude A_{Stark} and the parity-nonconserving amplitude A_{PNC} have the same phase. Since A_{Stark} is real while A_{PNC} is imaginary, we need the two polarization components to be out of phase. Thus, we use elliptically polarized light of the form $\boldsymbol{\epsilon} = \epsilon_z\hat{z} + \epsilon_x\hat{x}$, where ϵ_z is the component perpendicular to $\boldsymbol{E}$ and defined to be real, while ϵ_x is the component parallel to $\boldsymbol{E}$ and set to be imaginary, $\epsilon_x = i\epsilon_I$. The effect of imperfect polarization, that is, of a real component to ϵ_x, which we call ϵ_R, is discussed in Sect. 5.

©1999 NRC Canada

For the above experimental geometry, the transition rate from the 6S (F, m) state to the 7S (F', m') state is given by

$$R(F, m \to F', m') = (C_{Fm}^{F'm'})^2 \left[\beta^2 E_x^2 \epsilon_z^2 \mp 2\beta E_x \epsilon_z \epsilon_I \mathrm{Im}(E1_{\mathrm{PNC}}) \pm 2\beta E_x M1(|\epsilon_z^{k+}|^2 - |\epsilon_z^{k-}|^2)\right] \delta_{m,m'\pm 1} \tag{9}$$

where the $\mp$ depends on the sign of the initial-state magnetic sublevel; ϵ_z^{k+} and ϵ_z^{k-} represent the z components of the laser field for the laser beam propagations $\hat{k} = +\hat{y}$ and $\hat{k} = -\hat{y}$, respectively; and we have neglected terms involving only A_{PNC} and A_{M1}.

The first term in (9) represents the pure Stark-induced transition rate, while the second term represents the interference between the Stark-induced amplitude and the much smaller PNC amplitude. We call this second term the Stark–PNC interference term; note that it reverses sign when there is a reversal in either the direction of the applied electric field E_x (which we call e-reversal), the sign of the x component of the dye-laser polarization ϵ_I (p-reversal), or the sign of the magnetic sublevel m (m-reversal). The third term represents the interference between the Stark-induced amplitude and the magnetic-dipole amplitude. For our experimental configuration, in which we use a standing-wave dye-laser beam, the z components of that beam's polarization, ϵ_z^{k+} and ϵ_z^{k-}, are nearly equal, so that this third term is negligible. However, incomplete cancellation can lead to systematic errors, which are discussed in Sect. 5.

We determine the ratio of the parity-violating interference term to the total transition rate by measuring the fraction of the total signal intensity that modulates with reversal of the handedness of the excitation region. From (9), this fraction is given by

$$\frac{R_+ - R_-}{R_+ + R_-} = \frac{2\mathrm{Im}(E1_{\mathrm{PNC}})}{\beta E_x} \frac{\epsilon_I}{\epsilon_z} \tag{10}$$

neglecting systematic errors. The subscripts $+$ and $-$ refer to the handedness of the coordinate system.

To extract our final PNC result, $\mathrm{Im}(E1_{\mathrm{PNC}})/\beta$, from this fractional modulation, we must also measure the x component of the electric field E_x and the ratio of the components of the dye-laser polarization ϵ_I/ϵ_z. Since we measure a fractional modulation, there is a cancellation of other experimental parameters such as the atomic beam flux and the laser intensity.

To gain perspective on the magnitude of these transition rates, consider the allowed transition between the 6S and 6P states, which has an oscillator strength of 1. In contrast, for the $\Delta F = 0$ transition between the 6S and 7S states at our typical DC electric field of 500 V/cm, the pure Stark-induced transition has an effective oscillator strength of 10^{-11}, while the pure $M1$ transition has an oscillator strength of 10^{-13} and the pure PNC transition has an oscillator strength of 10^{-22}.

2.3. Zeeman spectrum

To selectively excite a single transition between two magnetic sublevels, we apply an external uniform magnetic field, which shifts the energies of the different sublevels by different amounts. For a small magnetic field $\boldsymbol{B}$, which is the case for our experimental conditions, the energy shift for a state $|\, nSFm\rangle$ is given by

$$\Delta\nu_m = \langle nSFm \mid \frac{\mu_B}{\hbar}\boldsymbol{\sigma} \cdot \boldsymbol{B} \mid nSFm\rangle = \mu_B g_F m B = (0.35\ \mathrm{MHz/G}) m B \tag{11}$$

Since $g_{F=4} = -g_{F=3} = 1/4$, the sublevels of the $F = 4$ hyperfine state shift in the opposite direction from those in the $F = 3$ hyperfine state, resulting in a resolved spectrum for the 6S–7S $\Delta F = \pm 1$ transition, as shown in Fig. 3. This theoretical spectrum corresponds to a cesium beam that is not spin polarized; the absence of $\Delta m = 0$ transitions is due to our field configuration. Note that each

©1999 NRC Canada

Fig. 3. A theoretical spectrum of the $\Delta F = -1$ 6S–7S transition of cesium in a small applied magnetic field. Note that only the two outer lines correspond to one transition between magnetic sublevels; the rest correspond to two transitions.

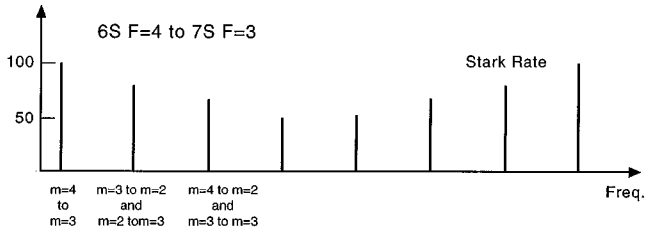

line is the sum of two transitions, $\Delta m = +1$ and -1, except for the two outermost lines, which involve only a single transition, either $m = 4 \rightarrow 3$ or $m = -4 \rightarrow -3$. Therefore, to excite a single transition, we tune our dye-laser frequency to that of either of the two outer lines.

Our present experiment differs from our previous ones in that we use a spin-polarized cesium beam, that is, we pump all the atoms into either the highest or lowest magnetic sublevel of the initial hyperfine state. Since this spin-polarized cesium beam has little population in the neighboring sublevel, the resolution of the Zeeman spectrum is not as crucial, allowing us to use a weaker magnetic field (6 G rather than the previous 74 G). The effect of both spectrum resolution and any residual population in the neighboring sublevels is discussed in Sect. 5.

In addition to shifting the energies of the states, the magnetic field also mixes the states. In our 1988 PNC measurement, this state mixing was a significant problem because we used a stronger magnetic field, resulting in additional, small, $\Delta m = 0$ peaks in the $\Delta F = \pm 1$ spectrum. Since we do not observe any $\Delta m = 0$ transitions in our present experiment and calculations indicate that it is very small, we neglect the effect of state mixing in our analysis.

3. Experiment

3.1. Overview

A schematic of the apparatus is shown in Fig. 4. This is all contained in an aluminum vacuum chamber at a pressure of less than 10^{-6} Torr. The cesium beam emanates from an oven with a multichannel capillary array nozzle. It then enters the optical pumping region, where a static magnetic field lifts the degeneracy of the magnetic sublevels and two diode lasers (labeled hyperfine pump (HFP) and Zeeman pump (ZP) lasers in the figure) pump the atoms into a particular (F, m) sublevel of the 6S state. Since we want to measure the transition rate for two transitions, 6S $F = 3 \rightarrow$ 7S $F = 4$ and 6S $F = 4 \rightarrow$ 7S $F = 3$, we prepare the initial 6S state in one of four hyperfine states: $(F = 3, m = \pm 3)$ or $(F = 4, m = \pm 4)$. For the purpose of this overview, we consider preparation of the 6S $(F = 3, m = 3)$ initial state, as shown in Fig. 1.

The resulting spin-polarized cesium beam then enters a region of mutually perpendicular magnetic and electric fields, the interaction region, where a frequency-locked dye laser excites the transition between the 6S (3,3) and 7S (4,4) states. The interaction region is actually a high-finesse Fabry–Perot power buildup cavity (PBC), which enhances the Stark–PNC interference while suppressing the Stark–$M1$ interference. The DC electric field is generated by a pair of parallel plates that are each divided into five isolated segments to provide greater control of electric-field components and gradients in diagnostic tests.

The excited cesium atoms then decay (by fluorescence) to the 6S state, via the 6P state, thus populating the hyperfine state that had been emptied in the optical pumping region, in this case $F = 4$. It is atoms in this repopulated hyperfine state, (which we call F_{det}), that we detect.

©1999 NRC Canada

Fig. 4. Schematic of the experimental apparatus showing the three main regions: the optical pumping region, the interaction region, and the detection region. Note how the magnetic field changes direction from the optical pumping region to the interaction region.

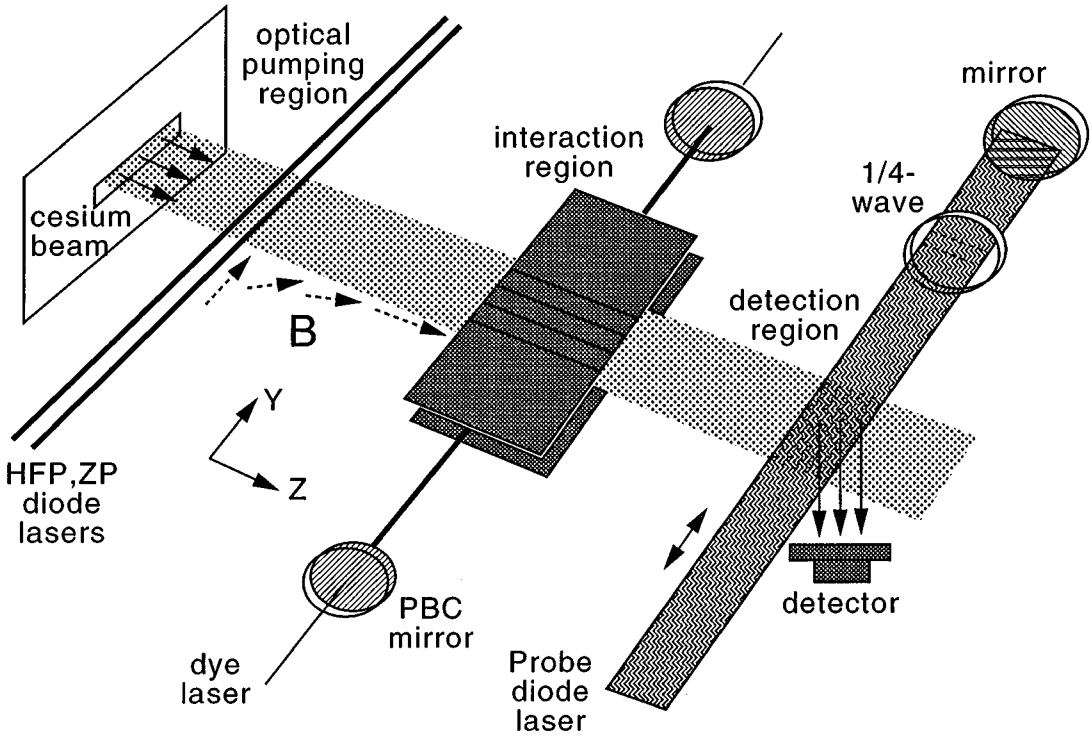

The cesium beam then enters the detection region, where it intersects a probe laser beam that is tuned to the cycling transition between the 6S ($F_{\mathrm{det}} = 4$) and $6P_{3/2}$ ($F = 5$) states. This probe laser excites each atom many times, and we detect scattered probe-laser photons with a photodiode detector located below the atom beam.

There are five ways that we can reverse the sign of the Stark–PNC interference term in (9) without reversing the sign of the pure Stark-induced transition rate; each of these reversals corresponds to a change in the handedness of the coordinate system in the interaction region. We can reverse the sign of E_x by reversing the direction of the electric field (e-reversal); we can reverse the sign of ϵ_x by reversing the handedness of the polarization of the dye laser (p-reversal); or we can reverse the sign of the Clebsch–Gordan coefficient term by reversing the sign of the magnetic sublevel, which we do by reversing the direction of the magnetic field (b-reversal). Since we use a spin-polarized atomic beam, there are two additional ways to reverse the sign of the magnetic sublevel: we can reverse the handedness of the polarization of the Zeeman pump laser (m-reversal), or reverse the direction of the magnetic field in the optical pumping region (a-reversal). The overall handedness of the interaction region ($+$ or $-$) is then determined by the product of the states ($+$ or $-$) for each reversal.

Thus by using a spin-polarized atomic beam, we increase the redundancy on our measurement to five. This redundancy is crucial in decreasing the uncertainty in our final result, for the product of the uncertainties for each of the five reversals is much smaller than the PNC signal itself. In addition, looking at various combinations of reversals enables us to detect misalignments and imperfect reversals and thus eliminate the corresponding potential systematic errors.

To attain the necessary precision in our final result, high-precision laser stabilization is required for

©1999 NRC Canada

all four lasers. We use optical and electrical feedback to control frequency and intensity. We also require precise control of the magnetic field in the three regions. While a uniform field of 2.5 G in the y direction is required in the optical pumping region, a field of 6.4 G in the z direction is required in the interaction region. In between these regions, the field must gradually transition in both magnitude and direction so that the atomic spins follow adiabatically. Furthermore, the field must be nearly zero in the detection region. And we must be able to reverse the field directions in the optical pumping and interaction regions independently, without affecting the other two regions. To achieve these requirements, we use 23 magnetic field coils to generate the fields and gradients. Finally, to achieve precise control over the alignment of our apparatus, we use 31 additional servo systems that ensure optical, mechanical, and thermal stability.

Roughly 7 000 h of data were acquired, corresponding to 7×10^8 measurements of the transition rate. Although the quantity of most fundamental importance is the particular modulation that is synchronous with reversal of the handedness of the coordinate system, only about 5% of the total data collected is used to measure this quantity. The majority of the data is taken to study and eliminate systematic errors.

3.2. Preparation of atomic cesium beam

The spin-polarized cesium beam is the main improvement of this experiment over our previous experiments. Its advantages include an increase in the number of initial-state atoms, an increase in the detection efficiency, and a decrease in the required magnetic-field strength. A detailed analysis of the spin-polarized beam can be found in ref. 20, which includes the density-matrix formalism describing the pumping process, limits to hyperfine-level depletion, and noise sources and requirements. Here we summarize the atomic-beam characteristics and the preparation of spin polarization by optical pumping.

3.2.1. Atomic beam characteristics

The cesium beam is produced in an oven that has a nozzle consisting of a glass capillary array. The shape of the atomic beam is primarily determined by the shape of the capillary array (0.8 cm $\times$ 2.5 cm rectangle, longer in the horizontal y direction than in the vertical x direction), as well as by the apertures downstream. As shown in Fig. 5, the atoms leave the capillary array, pass through a rectangular copper aperture cooled to liquid-nitrogen temperature, then through a brass vane collimator (vane separation $= 0.5$ mm), which is adjustable in the horizontal direction, and finally through a third aperture, before entering the optical pumping region (located 10 cm from the nozzle) where two diode-laser beams pump the atoms into a single hyperfine magnetic sublevel.

Once through the optical pumping region, the spin-polarized atoms pass through a second brass vane collimator (vane separation $= 0.1$ mm), which is adjustable in the horizontal direction, and another liquid-nitrogen-cooled aperture, before entering the interaction region (located 25 cm from the nozzle) where a dye-laser beam excites them to a single magnetic sublevel of a 7S hyperfine state.

Once through the interaction region, the atoms enter the detection region (located 35 cm from the nozzle) where atoms that have undergone the transition to the 7S state (and subsequent decay to the previously emptied 6S hyperfine state, F_{det}) are detected with a probe diode-laser beam. Upon exiting the detection region, the atoms then strike a liquid-nitrogen-cooled beam dump.

As a result of these apertures, for which the vertical height gets progressively smaller while the horizontal width remains at about 2.5 cm, the horizontal Doppler width of the beam is about 15 MHz in the interaction region; the horizontal density is fairly uniform, with 64% of the atoms located in the central 1.25 cm of the beam; and the vertical density distribution is roughly Gaussian. The flux is about 10^{13} atoms/s. The aluminum vacuum chamber is pumped to a pressure of 6×10^{-7} Torr.

3.2.2. Preparation of spin polarization by optical pumping

We use an optical pumping technique to prepare the cesium atoms in one magnetic sublevel of one 6S hyperfine state. In particular, we prepare one of the following (F, m) sublevels: (4,4), (4,–4), (3,3), or

©1999 NRC Canada

Fig. 5. A view of the atomic beam path from above, showing details of the beam collimation and the hyperfine-pump clean-up laser beams. The numbers refer to different coils used to generate magnetic fields and magnetic-field gradients.

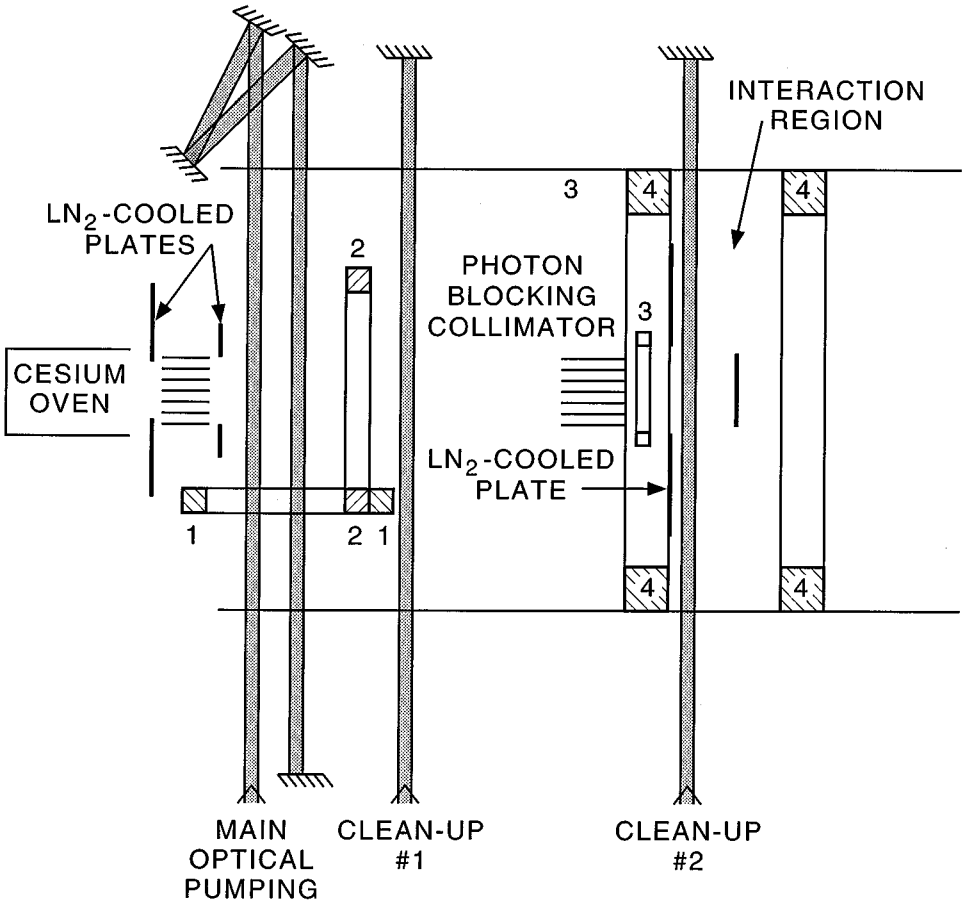

(3,–3). Our technique consists of two optical pumping processes performed simultaneously. For clarity of explanation, we consider here the preparation of the (3,3) sublevel, shown on the left-hand side of Fig. 6. One advantage of this technique is that it allows us to switch quickly between preparation of the (3,3) and (3,–3) sublevels, and thus rapidly switch the handedness of the interaction region. Here we provide a summary of our method; a more detailed discussion can be found in ref. 20.

Hyperfine pumping— To deplete the 6S $F = 4$ state, also called the 6S $F_{\rm det}$ state, we tune the hyperfine pump diode laser to the transition between that state and the $6P_{3/2}$ $F = 3$ state, as shown in Fig. 6. To ensure that atoms in all the $F = 4$ magnetic sublevels can be pumped directly to the $6P_{3/2}$ $F = 3$ state, we use light that is linearly polarized perpendicular to the direction of the applied magnetic field in the optical pumping region, and thus perpendicular to the atomic quantization axis.

We operate this diode laser (SDL 5401-G1 semiconductor laser) in a Littrow external-cavity configuration, as described in refs. 23 and 24, and lock its frequency to the appropriate hyperfine transition at 852 nm using saturated absorption spectroscopy. The noise on the saturated absorption peak (at 27 Hz) is 30 ppm/$\sqrt{\rm Hz}$. We operate the laser at a power density of 20 mW/cm^2, well above the 3 mW/cm^2 level needed to saturate the transitions.

©1999 NRC Canada

Fig. 6. Schematic of the optical pumping scheme used to prepare spin-polarized cesium atoms.

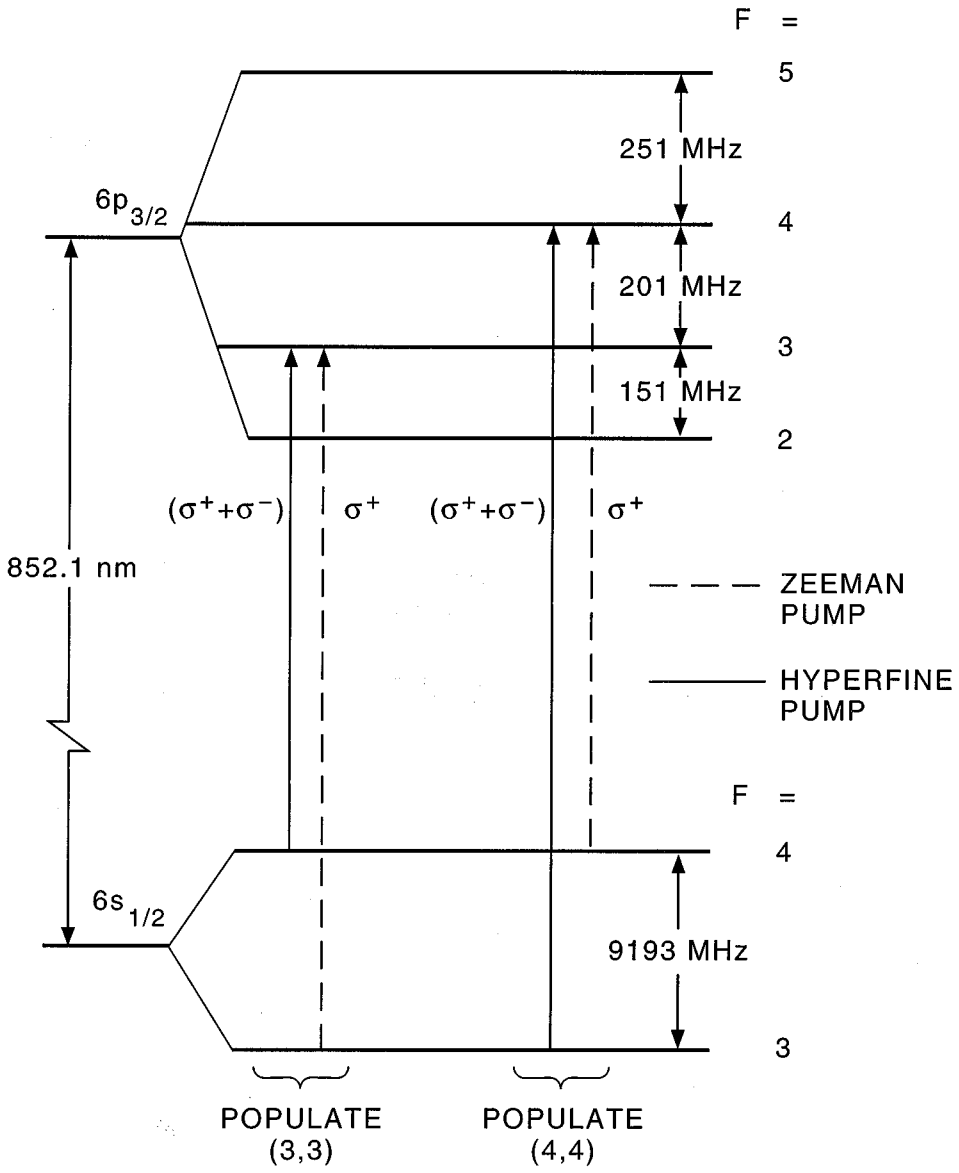

When we study the other hyperfine transition, $F = 4 \rightarrow 3$, we deplete the sublevels of the 6S $F = 3$ state by tuning the hyperfine pump laser to the transition between this state and the $6P_{3/2}$ $F' = 4$ state. However, the hyperfine pumping process for this transition is less efficient for two reasons: the branching ratio is not as favorable and the $F' = 4$ state has a Landé g-factor, g_4, of 4/15 (as compared with the $F' = 3$ state which has $g_3 = 0$). This finite value of the Landé g-factor results in excited-state Zeeman shifts that act as detunings for the magnetic sublevels. Fortunately though, since the magnetic field in the optical pumping region is only 2.5 G, the magnetic sublevel transitions are saturated; moreover, the pumping is done by triple beams going in slightly different directions. Thus detuning is not a problem.

©1999 NRC Canada

Zeeman pumping— To move the atoms in the seven magnetic sublevels of the 6S $F = 3$ state over to the $m = 3$ sublevel, we tune the Zeeman pump diode laser to the transition between this 6S $F = 3$ state and the $6P_{3/2}$ $F' = 3$ state and use σ^+ polarization. To move them over to the $m = -3$ sublevel, needed to reverse the handedness of the coordinate system in the interaction region (m-reversal), we reverse the Zeeman pump laser polarization to σ^- by reversing a quarter-wave plate.

To study the other hyperfine transition, ($F = 4 \rightarrow F' = 3$), we populate either the $m = 4$ or $m = -4$ sublevel of the 6S $F = 4$ state by tuning the Zeeman pump diode laser to the transition between this hyperfine state and the $6P_{3/2}$ $F' = 4$ state and using the appropriate polarization. We also tune the hyperfine pump laser to the appropriate transition.

We operate the Zeeman pump diode laser (SDL 5421-G1 semiconductor laser) in the same configuration as described above for the hyperfine pump diode laser.

Alignment of the optical pumping beams— Both of the optical-pumping laser beams make a triple pass through the optical pumping region, as shown in Fig. 5. We align the beams approximately parallel to the magnetic field in this region. Although the alignment of the hyperfine pump beams is not important, that of the Zeeman pump beams is, since good spin polarization requires that the quantization axis defined by the direction of laser propagation be parallel to that defined by the magnetic field. In practice, we first align the Zeeman pump beams along the magnetic field direction, and then align the hyperfine pump beams along these Zeeman pump beams. To maximize the spin polarization of the atomic cesium beam, (that is, the population of the magnetic sublevel $m = 3$ for our example case of an initial (3,3) sublevel), we then adjust the alignment of both optical-pumping diode lasers while monitoring a Raman transition from a neighboring sublevel. Since we want to minimize the population in the neighboring sublevel, we adjust the alignment of the pump lasers to minimize the signal from this Raman transition. Using this method, we typically attain at least 96% population of the desired sublevel, as described in Appendix A.

The optical pumping process produces scattered light which can get reabsorbed as it goes down the atomic beam and thus can repopulate the emptied hyperfine state. Since we use this emptied hyperfine state to detect atoms that have undergone a 6S–7S transition, any atoms that are in this state without having undergone the transition will contribute a background signal to the detection signal; we call this background contribution the "optical pumping (OP) background."

To reduce the OP background signal, we use two additional hyperfine-pumping "clean-up" laser beams, located downstream from the optical pumping region, as shown in Fig. 5. These clean-up beams reduce the OP background by a factor of 150. Under optimal running conditions, atoms in the emptied hyperfine state make up only 0.03% of the total number of atoms in the beam, corresponding to a signal-to-background ratio of 4. Since the dominant source of noise on the OP background is shot noise, the fractional noise on the background signal is only 25 ppm/$\sqrt{\text{Hz}}$, which corresponds to a fractional noise on the total signal (6S–7S signal + OP background) of 6 ppm/$\sqrt{\text{Hz}}$. For futher discussion of this background signal, see Sect. 4.4.

3.3. Excitation of the 6S $\rightarrow$ 7S transition

3.3.1. Overview

In the interaction region (see Fig. 4), the spin-polarized cesium atom beam intersects a dye-laser beam that is tuned to the transition between the 6S and 7S states. Excitation of this transition involves the most difficult optical, mechanical, and electronic aspects of the PNC experiment. Since this transition is highly forbidden, we require high laser power. To achieve continuous-wave power densities greater than 1 MW/cm^2 without focusing the laser beam, we use a power buildup cavity (PBC) that spans the interaction region. One complication of using a PBC is that the dye-laser beam frequency must precisely match the resonant frequency of the PBC. We also require that the dye-laser beam intensity be highly stabilized, and we need precise control over the dye-laser polarization, $\boldsymbol{\epsilon}$, since reversal of the phase

©1999 NRC Canada

Fig. 7. Block diagram of the optics that control the 540 nm laser light used to excite the 6S–7S transition. The dye laser is locked to the power buildup cavity (PBC), which in turn is locked to the reference "Invar" cavity, which in turn is locked to the 6S–7S atomic transition. The other optics are used to control the intensity and polarization of the light in the PBC. The photodiode located after the PBC detects transmitted laser light and is used for intensity stabilization, while the photodiode located before the PBC detects reflected light and is used for frequency locking. Note that this diagram is not drawn to scale, for in the actual experiment the reflections leading to the frequency-locking photodiode are near normal.

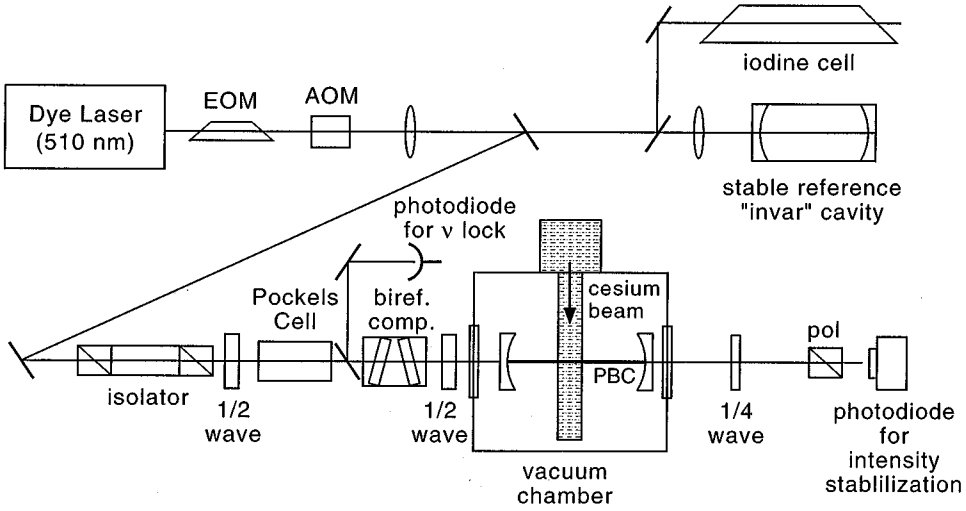

relationship between the x and z components of $\boldsymbol{\epsilon}$, (p-reversal), is one way we reverse the handedness of the interaction region.

A block diagram of the optics used to generate and control the 540 nm dye-laser light that excites the transition between the 6S and 7S states is shown in Fig. 7. Briefly, a dye laser generates light at 540 nm. This light is then phase-modulated at 7.3 MHz by an electro-optic modulator (EOM), which allows the light to be frequency locked to the PBC, which in turn is locked to a stable reference "Invar" cavity. For intensity stabilization, the laser light then passes through an acousto-optic modulator (AOM). After the AOM, part of the light is split off and sent to the Invar cavity. The main laser beam passes through various optics to control its polarization and shape so that it is mode-matched into the TEM_{00} mode of the PBC. The intensity of the light exiting the PBC is then monitored with a fast photodiode.

3.3.2. Dye laser

We generate 540 nm light by pumping a ring dye laser (a modified Spectra-Physics 380) with an argon ion laser (Coherent Innova-90). Typical ion-laser powers range from 3 to 5 W, depending on the age of the dye, resulting in 200 to 500 mW of tunable, single-frequency, 540 nm light. To make the dye solution we dissolve 2.5 g Promethene 556 (Exciton, Inc.) in 2.5 L ethylene glycol. To form the dye jet, we use a sapphire nozzle.

We coarsely tune the dye-laser frequency with an intracavity birefringent tuner, and select the longitudinal lasing mode with both thick and thin etalons. We perform fine frequency tuning via three intracavity elements: a set of galvanometer-mounted glass plates (20 GHz range), a piezo behind one of the cavity mirrors (320 MHz range), and an intracavity EOM (20 MHz range). We lock the dye-laser frequency to the resonant frequency of the PBC.

©1999 NRC Canada

Fig. 8. A schematic of the mechanical design of the power buildup cavity (PBC), showing the vibration isolation, the mirrors, the output-mirror rotation stage, the segmented electric-field plates, and the tilt stage for these plates.

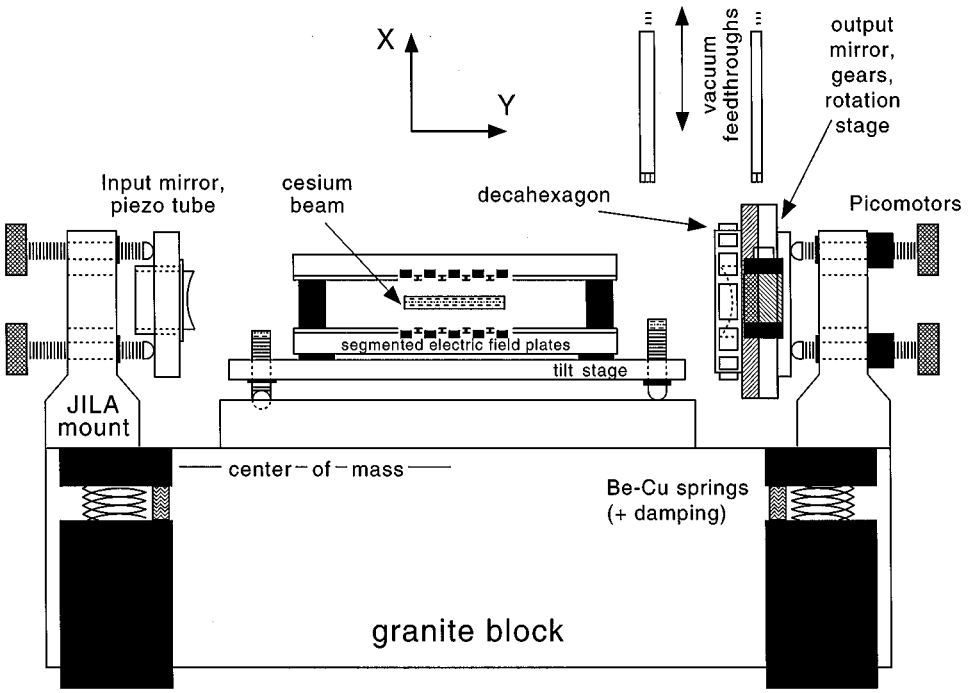

3.3.3. Power buildup cavity (PBC)

The power buildup cavity is a resonator configured specifically to maximize the intracavity power. As shown in Fig. 7, it is defined by two mirrors located on either side of the interaction region and consisting of multilayer dielectric coatings on fused silica substrates (2.5 cm diameter, 6 mm thick). The input mirror has a 10 m radius of curvature, while the output mirror has a 6 m radius; both mirrors have antireflection coatings on their outer sides. The mirrors are separated by 27 cm, giving a 500 MHz free spectral range and a fairly large intracavity spot (radius of 0.82 mm). Since this cavity is nearly a "flat–flat" resonator, the spot diameter varies by less than 1% over the 2.5 cm length of the overlap between the laser and atomic beams, thus maximizing the overlap volume and, in turn, the signal intensity.

The values for the mirror transmissions are $T_{\text{input}} = 40$ ppm, $T_{\text{output}} = 13$ ppm, and the loss from scatter and absorption is 5 ppm for each mirror. (Losses due to absorption of light by the atoms are $<< 1$ ppm, and thus negligible.) For our cavity, the finesse $F = 100\,000$ and the power buildup factor $F_o = 30\,000$. From the injected laser power and the beam diameter, we calculate that the power density is 800 kW/cm^2 at the interaction region for our typical operating conditions.

A major concern with the PBC mirrors is the birefringence of the coatings, since this can lead to systematic errors in the PNC measurement. One source of birefringence is mechanical stress to the mirror substrate. To minimize stress, we mount the mirrors gently, using a silicone rubber adhesive, RTV. This adhesive is mechanically stable and does not "relax" (which could misalign the PBC). The piezo tube attached to the input mirror still causes some stress birefringence on it. Moreover, as the voltage on the piezo varies, the stress on the input-mirror coating changes, and thus so does the birefringence. Typically, the birefringence on the input-mirror coating, ϕ_1, is 3.0 ± 0.1 μrad, (though during the PNC experiment, when the mirror is stressed by the piezo, the birefringence can vary between 2.8 and 3.2

©1999 NRC Canada

μrad), while the birefringence on the output-mirror coating, ϕ_2, is 2.0 ± 0.1 μrad.

The birefringence can change over time because of changes in temperature or exposure to high-intensity linearly polarized light. The light apparently distorts the coating slightly, but these effects can be "annealed" out by exposure to circularly polarized light. Since any birefringence in the output mirror can lead to a systematic error, (as discussed in Sect. 5), we typically wait several hours after switching from circularly polarized light to elliptically polarized light before taking data, so that the birefringence stabilizes.

The mechanical design of the power buildup cavity is shown in Fig. 8. Two JILA-designed optical mounts are bolted to a large granite block, which provides a large mass and good stiffness. The cavity is suspended in the plane of its center-of-mass by four beryllium–copper springs, each damped by a small amount of sorbothane rubber. This configuration minimizes relative tilts between the cavity and the optical table. The combination of soft suspension and high mass leads to very low vibrational frequencies (1 to 8 Hz). These low vibrational frequencies, in conjunction with an air-suspended optical table which itself has low vibrational frequencies ($\leq$1 Hz), result in good isolation of the PBC from any external vibrational perturbations that correspond to the operating frequency (27 Hz) of the PNC experiment.

The input mirror and piezo tube are positioned on the front face of the JILA mount. Both mirrors have temperature-stabilized mounts to prevent changes in the mechanical stress, and warm covers to prevent cesium deposition. Since the output-mirror birefringence can lead to a PNC systematic error, as discussed in Sect. 5, it requires a more intricate mount.

The front face of the output mirror is a spring-loaded, JILA-designed, rotation stage, fitted with a gear around its circumference. A mechanical attachment with an orthogonal matching gear allows this rotation stage to be operated from above. To perform a rotation, a vacuum feedthrough is lowered into the gear system; after rotation, the feedthrough is removed to avoid disturbing the stability of the PBC. To measure the rotation angle precisely, a precision-mounted decahexagon (16 sides) is also mounted on the rotation stage, each side of the decahexagon having a small mirror that is used to reflect a helium–neon laser beam incident from above. We use micrometre-replacement actuators to realign the PBC under vacuum, particuarly after a rotation of the output mirror.

3.3.4. Dye-laser frequency lock

We lock the dye-laser frequency to the PBC resonance frequency using the Pound–Drever–Hall technique [25, 26] with a 7.3 MHz modulation frequency that is provided by the electro-optic modulator (EOM), shown in Fig. 7; light reflected from the PBC is detected by a fast photodiode. This servo system has a unity-gain frequency higher than 1 MHz and results in a relative laser line width that is much less than the 5 kHz resonance width of the PBC.

Any polarization dependence of the optics used in this PBC-dye laser frequency locking system can lead to a PNC systematic error. Characterization and elimination of this systematic error is discussed in Sect. 5; here we simply mention that to minimize this systematic error, we exclusively use near-normal-incidence reflections for the optical path leading to the fast photodiode.

3.3.5. PBC resonance-frequency lock

Although the extremely high finesse of the PBC allows significant laser line-width reduction, the PBC is not suitable as an absolute frequency reference because mechanical motion of the mirrors can cause its frequency to fluctuate. This motion arises from the electric-field plates and magnetic coils that are mounted on the PBC, and from the mechanical instabilities in the mirror mounts. To eliminate these fluctuations we lock the resonant frequency of the PBC to a much more mechanically stable reference cavity, shown in Fig. 7. This cavity is much more stable because it consists of a single solid chunk of Invar with a small hole drilled though it, a mirror bonded onto one end, and a short piezo tube and

©1999 NRC Canada

mirror rigidly bonded onto the other end. The mirrors are mounted confocally 7.5 cm apart, giving a free spectral range of 1 GHz. The finesse is about 300.

To reduce the temperature-dependent drift of the Invar cavity's resonance frequency, we place the cavity in a temperature-stabilized sealed can. To lock the PBC to the Invar cavity, we again use the Pound–Drever–Hall technique [26] with the same EOM to generate the 7.3 MHz sidebands. Although the unity-gain frequency for this servo loop is only 3 kHz, this is sufficient to eliminate PBC vibrations as a source of noise on the 6S–7S transition signal.

3.3.6. Invar-cavity frequency lock

To eliminate very slow drifts in the resonance frequency of the Invar cavity we lock it to the transition frequency of the atoms in the interaction region. We generate an error signal by modulating the Invar-cavity resonance frequency at 300 Hz. This modulation, in turn, imposes a 300 Hz modulation on the resonance frequency of the PBC, which results in a modulation of the atomic transition intensity.

We use a lock-in amplifier to obtain phase-sensitive detection of the transition rate, and send the resulting demodulated signal to a servo filter. We then amplify this signal and send it to the piezo tube that is attached to the Invar cavity; this piezo tube corrects the resonance frequency of the Invar cavity, locking it to the peak of the transition between the 6S and 7S states.

Since there is a cesium-atom time-of-flight delay of 1 ms between the interaction region and the detection region, any frequency fluctuations greater than 1 kHz can not be addressed. Thus the servo loop that locks the Invar cavity to the atomic transition has both a low modulation frequency (300 Hz) and a low bandwidth, but these are sufficient since it is only correcting for very slow drifts.

3.3.7. Dye-laser intensity stabilization

To stabilize the intensity transmitted by the PBC (and hence the light inside the PBC), we detect light transmitted through the PBC with a photodiode and use the AOM to adjust the injected laser intensity, as shown in Fig. 7. The photodiode (EG&G Optoelectronics model SGD-200) has an active area of 0.3 cm^2 and is biased to 70 V. The resulting fractional noise on the intensity, measured by monitoring scattered light from the PBC output mirror, is less than 10 ppm/$\sqrt{\text{Hz}}$ at our data frequency of 27 Hz, which is an acceptable level. However, although this intensity servo gives an acceptable noise reduction, it can also introduce a PNC systematic error due to its dependence on the laser polarization, for when we alternate the laser beam between left- and right-circular polarization, the intensity servo imposes an intensity modulation on the beam.

To distinguish (and then eliminate) this modulation from the modulation due to PNC, we devised a test, described in Sect. 5, that uses the cesium atoms to detect the intensity-servo-imposed modulation. Here we describe how we use this modulation signal to eliminate the problem by minimizing the polarization dependence of three relevant surfaces shown in Fig. 7: the PBC output mirror, the vacuum chamber exit window, and the photodiode surface. (Note that the $\lambda/4$ plate and the polarizer shown in Fig. 7 are not in place when we take PNC data; they are in place only when we measure the dye-laser beam polarization). Although the PBC output mirror is made of fused silica, and thus should not be birefringent, mechanical stress from mounting can induce birefringence. Although this birefringence by itself does not lead to a systematic error, it does when in combination with an etalon effect between the front and back surfaces of the substrate. Therefore, we minimize the etalon effect of the mirror by antireflection (AR) coating the back side of the substrate and by mounting the mirror off-center on the rotation stage, thus making the substrate a wedge. The output window is made of glass and is AR coated on both sides. As we are unable to detect any birefringence of this window, we conclude that its birefringence, φ_w, is less than 10^{-3}. To minimize any etalon effects between this output window and any other optical surfaces, we mount the window at a small angle.

The primary polarization sensitivity comes from the photodiode. We tested several photodiodes, first removing their windows, which are usually of low quality. Our test consists of shining light of

©1999 NRC Canada

Fig. 9. Examples of dye-laser polarization ellipses for the two cases of p-reversal ($p =$ "+" and $p =$ "−"). For ideal circularly polarized light, shown in (a), there is no distinction between the $p = +$ and $p = -$ ellipses. For ideal elliptically polarized light, shown in (b), both ϵ_x and ϵ_z modulate with the p-reversal. For ideal elliptically polarized light, shown in (c), ϵ_R modulates with the p-reversal. A more realistic (though exaggerated) situation is shown in (d), which is a combination of the cases shown in (a), (b), and (c).

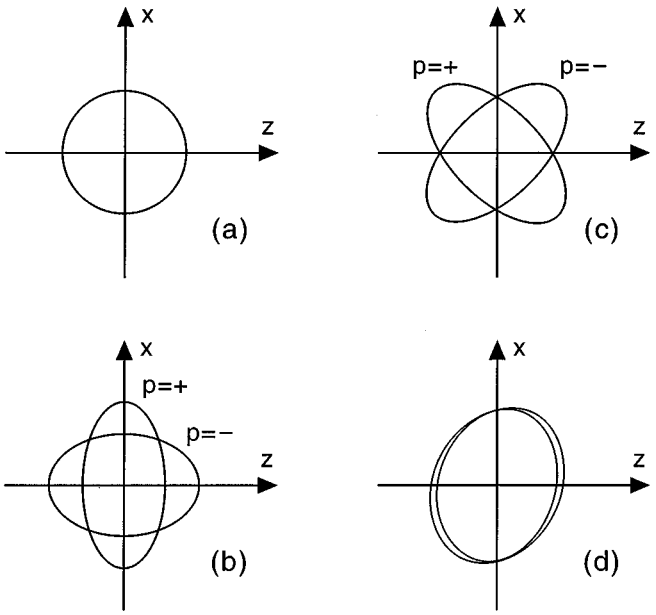

constant intensity on the photodiode, and then monitoring the resulting photocurrent as we rotate the photodiode. For linearly polarized light, we found that all the photodiodes show a modulation of the photocurrent; depending on the particular photodiode, this modulation ranged from 0.1 to 2.0%. For circularly polarized light, however, we could detect little or no modulation, as expected, since for this case there is no preferred axis along the photodiode. Although we took much of our PNC data with the dye-laser light circularly polarized, some of our data was taken with the dye-laser light elliptically polarized. For the case of elliptical polarization, we prevent polarization-induced modulation of the photocurrent by holding the ellipse's major axis at a constant angle when reversing the direction of the dye-laser polarization (p-reversal).

3.3.8. Dye-laser polarization control

To control the polarization of the dye-laser beam, we use a train of optical components, shown in Fig. 7. The laser beam first passes through a 40 dB optical isolator, which prevents any light reflected off the PBC from returning to the dye laser. Moreover, the exit polarizer of the optical isolator transmits light of a well-defined linear polarization, $\boldsymbol{\epsilon} = \epsilon_o(\hat{x} + \hat{z})$. The laser beam then passes through a half-wave plate which rotates the linear polarization. It then passes through a KD*P Pockels cell, which we use to apply a $+$ or $-\lambda/4$ retardance along the x axis. The rotation of the incident linear polarization relative to the Pockels cell axis controls the ellipticity of the polarization. In this way we produce a well-defined polarization ellipse, $\boldsymbol{\epsilon} = \epsilon_z\hat{z} \pm i\epsilon_I\hat{x}$, some examples of which are shown in Fig. 9. Switching from $+$ to $-$ $\lambda/4$ retardance is the polarization (p) reversal. The Pockels cell has two layers of temperature

©1999 NRC Canada

stabilization, and is attached to a finely adjustable rotation stage that is mounted on a tilt stage. We adjust the applied voltage to the Pockels cell for quarter-wave retardance [27].

Once the light enters the PBC, its polarization can be distorted by the birefringence of the coatings on the two cavity mirrors (3 μrad per reflection). Since the PBC has a very high finesse (100 000), the accumulated effect of many reflections introduces a non-negligible modulation on the 6S–7S transition rate that is synchronous with the p-reversal. To minimize this modulation, we use a birefringent compensator before the PBC, which compensates for the birefringence of the PBC mirror coatings and consists of a pair of $\lambda/30$ wave plates, nearly crossed, independently adjustable, and temperature stabilized. Since the birefringence of the PBC changes each time the PBC output mirror is rotated, we reset the compensator each time as well. Finally, since imperfections, misalignments, and light-induced birefringence of the mirror coatings can cause the polarization ellipse to rotate slightly, we use a second $\lambda/2$ plate, located just before the PBC, to align the ellipse with respect to the electric-field plates.

To measure the polarization of the light, we use two techniques. In one technique we monitor the intensity of the light transmitted through a linear polarizer as a function of the angle of rotation. In the other technique, we monitor the intensity of the light transmitted through both a fixed linear polarizer and a $\lambda/4$ plate as a function of the angle of rotation of the $\lambda/4$ plate. We then analyze the Fourier components of the transmitted intensity to determine the polarization state. Details of these two techniques are given in Appendix B.

3.4. Detection scheme

3.4.1. Overview

The repopulation detection scheme used in this experiment represents a substantial improvement over the detection scheme used in our previous experiments. In previous experiments, we collected fluorescence directly from the 7S state in the interaction region with a detector located behind the electric field plates, thus requiring the plates to be transparent. In our present work, we detect the 7S atoms when they have decayed down to the 6S hyperfine state (F_{det}) that had been emptied in the optical pumping region. We detect these atoms using laser-induced-fluorescence downstream from the interaction region. The branching fraction for decay into F_{det} is about 70%. In the detection region, these atoms are excited by a probe laser tuned to a cycling transition (6S $F_{\mathrm{det}} \rightarrow 6\mathrm{P}_{3/2}\ F'$). Each atom that has made the 6S–7S transition scatters about 1 000 photons. We collect about 250 of these photons with a photodiode detector (5 cm^2 silicon photodiode; 30 nF junction capacitance) operating in photovoltaic mode. We place a gold mirror opposite the detector to enhance the photon collection. The resulting photocurrent is amplified using a low-noise op-amp with a $10^7\ \Omega$ feedback resistor.

Using this method, our overall detection efficiency is 70% for the initial $F = 4$ hyperfine state, substantially higher than the 25% we achieved in our 1988 work. Moreover, our measured photocurrent is 1000 times larger than in our previous work, making it unnecessary to cool the photodetector with liquid nitrogen.

3.4.2. Detection loss due to dark states

The transition between 6S $F_{\mathrm{det}} = 4$ and $6\mathrm{P}_{3/2}\ F' = 5$ states (which is used to detect the 6S $F = 3 \rightarrow$ 7S $F = 4$ transition) scatters more photons than does the transition between the 6S $F_{\mathrm{det}} = 3$ and $6\mathrm{P}_{3/2}$ $F' = 2$ states (which is used to detect the 6S $F = 4 \rightarrow$ 7S $F = 3$ transition). In the latter case, the atoms can evolve, by optical pumping, into a dark state where they will no longer scatter photons [28].

To prevent the atoms from evolving into this dark state, we produce both a spatially varying probe laser polarization, as described below, and a small and spatially varying magnetic field, as described in Sect. 3.5.2. Under these conditions, our detection efficiency for the cycling transition between the $F_{\mathrm{det}} = 3$ and $F' = 2$ states is increased substantially, to 43% that for the transition between the $F_{\mathrm{det}} = 4$ and $F' = 5$ states.

©1999 NRC Canada

Fig. 10. A simplified circuit diagram of the double-integrator servo filter used to frequency lock the probe diode laser. The filter uses a "tracking" double-integrator configuration, with feedback to both the PZT and the injection current.

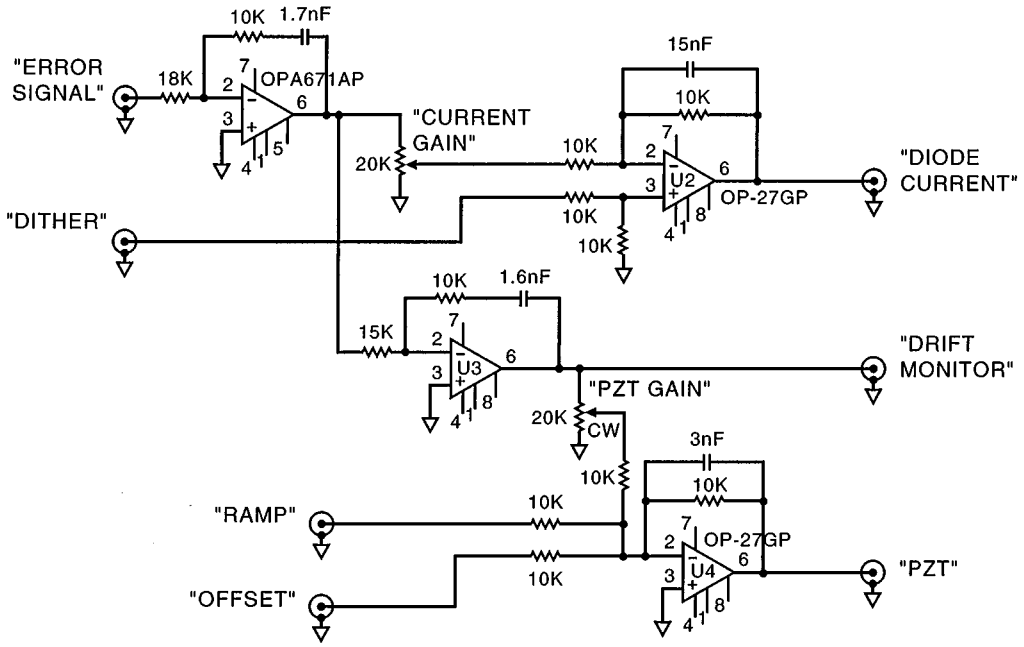

3.4.3. Probe laser

The probe laser is an AR-coated diode laser in a Littrow external-cavity configuration, as described in ref. 24. To lock the laser frequency, we split off 20% of the beam and send it to a saturated absorption spectrometer. The remaining light, after going through an optical isolator, goes through a set of cylindrical lenses to expand the laser beam to the size of the photodiode detector (2.5 cm). To filter out frequency components 9 GHz from the center frequency, which can excite the other ground hyperfine state, we send this beam through a solid-glass etalon filter cavity (20 GHz free-spectral range). This reduces the background in the probe region by 50%.

To produce a spatially varying probe-laser polarization we use a lin⊥lin configuration [29], in which the polarization changes as the light passes through the detection region. On the first pass, the light is linearly polarized along the z direction. Upon exiting the detection region, the light passes through a $\lambda/4$ plate, is retroreflected, passes again through the same $\lambda/4$ plate, and then passes back through the detection region, this time polarized along the x direction. As a result, a polarization gradient is produced, in which the polarization changes from σ^+ to linear ($\hat{x}$) to σ^- to linear ($\hat{z}$) and back to σ^+ in one half of a wavelength.

To achieve shot-noise-limited detection, we stabilize the probe diode-laser frequency. To lock the frequency of the diode laser to the relevant Doppler-free cesium hyperfine transitions (6S $F = 3 \rightarrow 6P_{3/2}F' = 2, 3, 4$; or 6S $F = 4 \rightarrow 6P_{3/2}F' = 3, 4, 5$), we use standard saturated absorption spectroscopy [20,24]. However, since we use an AR-coated diode, the laser tends to act less like a resonator and more like a gain medium. As a consequence, any change in the injection current can cause amplitude modulation (AM) rather than the desired frequency modulation (FM). Since low-frequency noise tends to have the largest frequency excursion, it leads to the largest conversion of FM to AM.

Thus, to minimize the conversion from FM to AM, we use a new servo filter that is based on a double-integration design, shown in Fig. 10. This double-integration design creates an enormous amount of gain

©1999 NRC Canada

Fig. 11. A spectrum of the noise on the saturated absorption signal, obtained with an FFT spectrum analyzer, taken while the probe laser is locked to the peak of the 6S $F_{\text{det}} = 4 \rightarrow 6\text{P}_{3/2} F' = 5$ cycling transition.

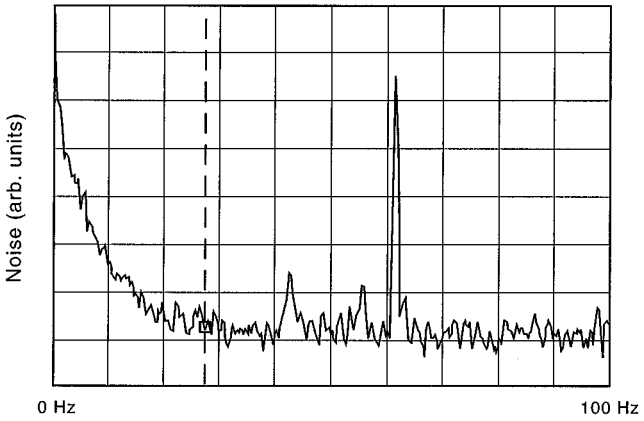

at DC, where we need it the most, while simultaneously minimizing the amplitude noise. Specifically, the error signal is first sent to a fast integrator, which immediately corrects the frequency excursion using the injection current. One might expect to then send the corrected output to the capacitor on this fast integrator, since the capacitor accumulates information about frequency excursions, including drifts. However, since the voltage on this capacitor is fed to the current, it can create the problematic AM. Therefore, to keep the voltage on this capacitor small, we send the corrected output instead to a second (slower) integrator, which then uses the piezo electric transducer (PZT) to correct frequency fluctuations. It is actually the capacitor on this slow integrator that accumulates the low-frequency information and the drift.

Thus, low frequencies are corrected with the PZT, while high-frequency information continues to be routed through the initial integrator (going to the diode current), so that the overall bandwidth of the servo is very high. Since a double integrator is inherently unstable, we close the current loop (initial integrator) before closing the PZT loop.

The performance of this double-integrator servo system is very good, giving a unity-gain servo frequency of about 80 kHz. We have found that the noise spectrum measured on a saturated absorption peak is a good indicator of the noise we measure on the atomic beam, both having similar line widths. Figure 11 shows a spectrum of the noise on the saturated absorption signal, used for locking the frequency of the Invar cavity to the atomic transition frequency, taken with the probe laser locked to the peak of the transition between the 6S $F = 4$ and $6\text{P}_{3/2}$ $F' = 5$ states. The noise is about 6 ppm/$\sqrt{\text{Hz}}$ at 27 Hz, falling to 3 ppm/$\sqrt{\text{Hz}}$. The noise spectrum of the atomic beam fluorescence for the same transition is similar, except that in the case of the atomic beam fluorescence, there is a substantial $1/f$ noise component for very low frequencies, probably due to laser beam motion.

The lasers used for optical pumping are similar, except that we replace the slow integrator with a very-high-gain, low-pass filter, which makes the system more robust, though it also reduces the DC gain.

3.5. Electric and magnetic fields

3.5.1. Electric field

We need to generate a DC electric field in the interaction region that is perpendicular to both the wave vector $\boldsymbol{k}$ of the dye-laser beam and the magnetic field B_z, as shown in Fig. 2. The two principle

©1999 NRC Canada

concerns in constructing the electric field plates are, first, precise control over the y component E_y, which is perpendicular to the main electric field and is used in diagnostic tests relevant to detecting and eliminating systematic errors, and second, minimization of stray (nonreversing) fields arising, in part, from deposition of cesium. Since cesium has a different work function than the eletric-field plate material, a battery is produced. Moreover, since the deposition pattern mirrors the atomic beam density, it produces a gradient in the stray electric field in the y direction, $\partial(\Delta E_y)/\partial y$, of magnitude between 50 and 300 mV/cm^2. In the presence of a similar gradient in B_x, this stray electric-field gradient results in a systematic error, as described in Sect. 5.

Electric-field plate design— Our solution to both these problems, (the need for greater control of E_y and the presence of a stray electric-field gradient in the y direction), is to use a set of plates that is divided into five isolated segments, allowing independent control of the voltage on each segment. This in turn allows us to simultaneously generate, in addition to the main, reversing electric field E_x, either a uniform electric field or an electric-field gradient in the y direction, without tilting the plates. Moreover, these segmented plates allow us to reverse the components of the electric field independently. The relevant fields that we generate are gE_y and $g(\partial E_y/\partial y)$, (a uniform field and gradient that we can reverse independently, with g the independent flipping parameter); eE_y and $e(\partial E_y/\partial y)$, (a uniform field and gradient that reverse with reversal of the main electric field direction, e-reversal); and ΔE_y and $(\partial \Delta E_y/\partial y)$, (a stray, or nonreversing, uniform field and gradient).

The plates are constructed from two pyrex glass plates (5 cm × 9 cm × 0.5 cm), coated with 100 nm of molybdenum (which gives an optical-quality molybdenum surface), and separated by 0.985 77(25) cm with four precision-ground ceramic spacers. Before applying the molybdenum coating, we drill five holes in the sides of each plate. The molybdenum coating partially covers these holes, and then solid turrets are fitted into the holes using silver epoxy, forming electrode connections. After applying the molybdenum coating, we use a carbide-tipped scribe to make four equally spaced scratches across the surface of each plate in the z direction (Figs. 4 and 8), deep enough to reach the glass and to give a large resistance between adjacent segments ($R > 10^7\Omega$).

We use molybdenum as the conducting metal because it generates low stray fields, probably because the metal and its oxide have similar work functions. The plates are mounted on a nonmagnetic tilt stage (Fig. 8) that is attached to the granite block of the PBC. A vacuum feedthrough can be engaged to adjust the tilt of the plates and thus control E_y/E_x.

Electric-field configurations— Two examples of electric-field configurations for the segmented field plates and the resulting potential curves for these configurations are shown in Fig. 12. We optimize the segment geometry using a commercial field-calculation program. To obtain a uniform electric field of 17 V/cm in the y direction (parallel to the plates), we use the configuration shown in Fig. 12*a*. To obtain an electric-field gradient along the y axis, we use the voltage configuration shown in Fig. 12*b*. In this case, E_y varies from 0 V/cm (at the center), to 11 V/cm (below the segments with 10 V applied), to 16 V/cm, and then drops again.

We use the electric-field configuration that generates a uniform E_y when we align the experimental coordinate system; specifically, we use it in our technique to null the magnetic-field components B_x, ΔB_x, $\partial B_x/\partial y$, and $\partial(\Delta B_x)/\partial y$. Occasionally, we also apply a gradient to cancel the gradient $\partial \Delta E_y/\partial y$ caused by cesium deposition.

A typical value for each component of the stray field $\Delta \boldsymbol{E}$ is 50 mV/cm, while a typical value for the gradient $(\partial \boldsymbol{E}/\partial y)$ is 150 mV/cm^2 (and always less than 200 mV/cm^2). Drift in the electric field predominantly occurs in the x component of the stray electric field ΔE_x, and is due to sections of the plates that have become charged. After running the cesium beam for a short warm-up period the drift becomes small (the change in $\Delta E_x/E_x < 100$ ppm).

©1999 NRC Canada

Fig. 12. Two electric-field configurations generated by the segmented field plates. In (*a*) a uniform electric field is generated along the *y* axis, while in (*b*) an electric-field gradient is generated along the *y* axis.

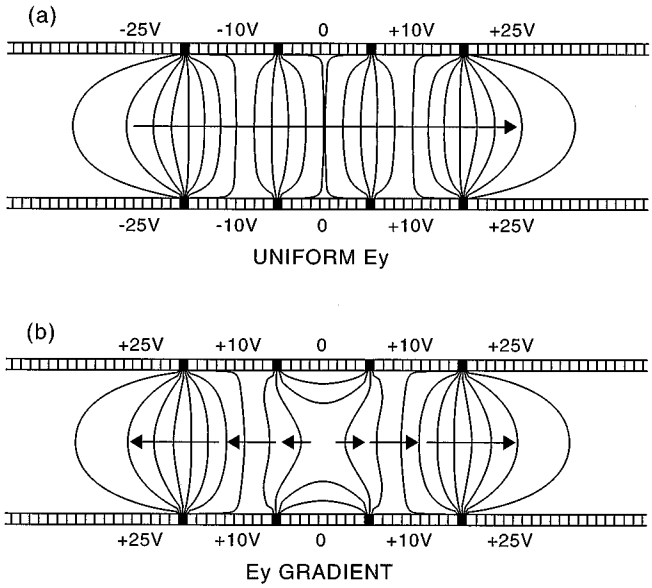

3.5.2. Magnetic field

In the optical pumping region, to prepare the spin-polarized atomic beam, we split the cesium magnetic sublevels with a uniform magnetic field of a few Gauss directed along the *y* axis, as shown in Fig. 4. Then, in the interaction region, to excite the initial cesium magnetic sublevel to a single magnetic sublevel of the 7S hyperfine state, we split the magnetic sublevels with a uniform magnetic field of about 7 G in the *z* direction. For the transition between these two regions, we need to rotate the magnetic field gradually enough so that the atoms follow, that is, so that their spin polarization remains aligned with respect to the magnetic field. Finally, in the detection region, we detect atoms that have undergone the transition by probing a particular hyperfine state regardless of magnetic sublevel; thus here we need a negligible magnetic field.

A detailed picture of the coils used to generate these magnetic fields is shown in Fig. 13. We use commercial software [30] to simulate the magnetic field and guide our choice of coil configurations. Sixteen of the coils are located inside the vacuum chamber, while seven coils are exterior. The exterior coils are used to shim out any stray uniform magnetic fields (ΔB_x, ΔB_y, and ΔB_z) in the vacuum chamber, which are due primarily to the Earth's magnetic field. Another (external) coil is used to cancel out the roughly dipole field ($\partial(\Delta B_y)/\partial y$) in the vacuum chamber, which is due to the magnetic field from the optical table.

Magnetic field in the optical pumping region— The pair of "optical pumping coils," labeled 1 in Fig. 13, is centered on the optical pumping region. The "canceling coil," labeled 2, is oriented 90° relative to the optical pumping coils and is used to cancel the large *z* component of the 7 G magnetic field in the interaction region that leaks into the optical pumping region. The net magnetic field in the optical pumping region, shown in Fig. 14, is about 2.5 G in the *y* direction. The vertical B_x component in this region, not shown, is very small because the coils are centered with respect to the atomic beam, which is narrow in the vertical direction. By reversing the direction of the current in the optical pumping

©1999 NRC Canada

Fig. 13. Two views of the coils used to generate magnetic fields. The atomic beam (thick band) and laser beams (broken lines) are also shown.

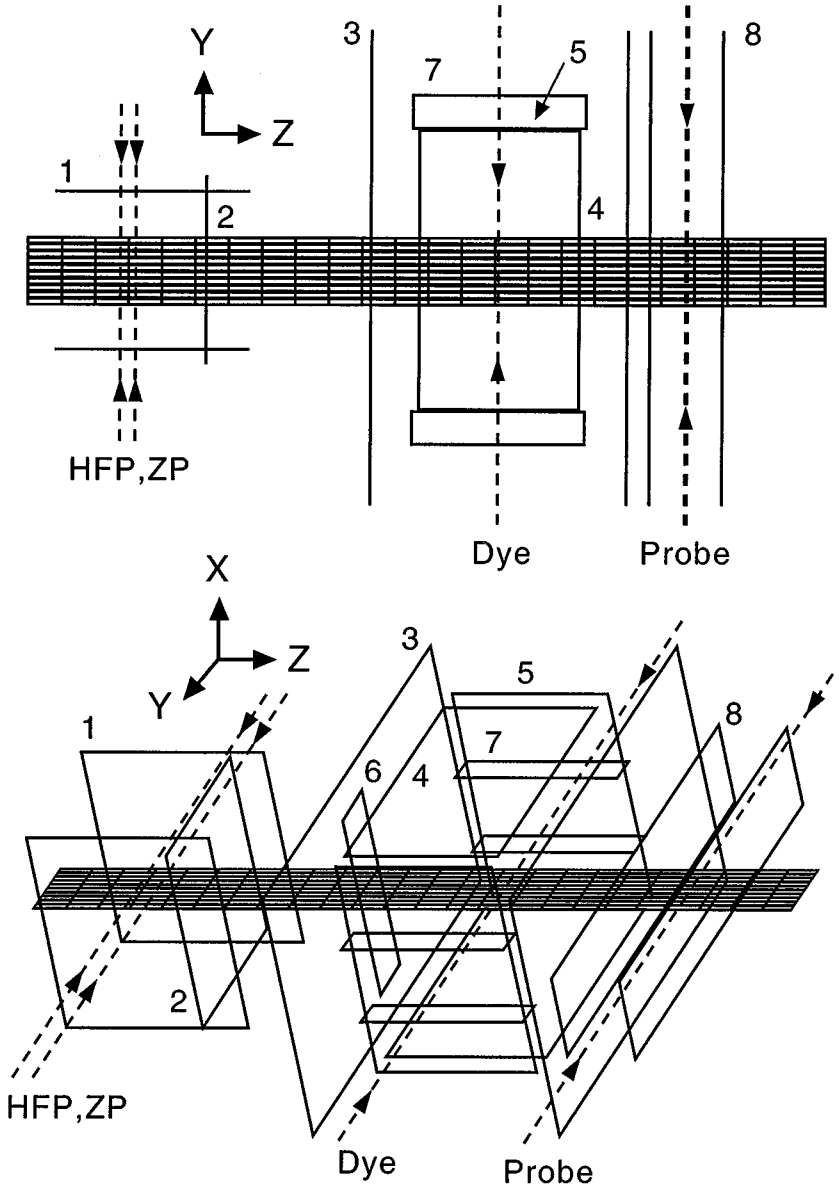

coils, we reverse the direction of the magnetic field in the optical pumping region and thus reverse the direction of the quantization axis (a-reversal).

Between the optical pumping and the interaction regions, the magnetic field bends by 90^{o} and its magnitude increases, as shown in Fig. 14. This bending is done adiabatically so that the spin-polarizied atoms follow the direction of the magnetic field.

Magnetic field in the interaction region— In the interaction region, we use a large pair of coils (labeled 3 in Fig. 13) to generate a 7 G field in the z direction. To precisely align the magnetic field with respect to

©1999 NRC Canada

Fig. 14. Magnetic-field components, in gauss, along the atomic beam path. The optical pumping, interaction, and detection regions are indicated.

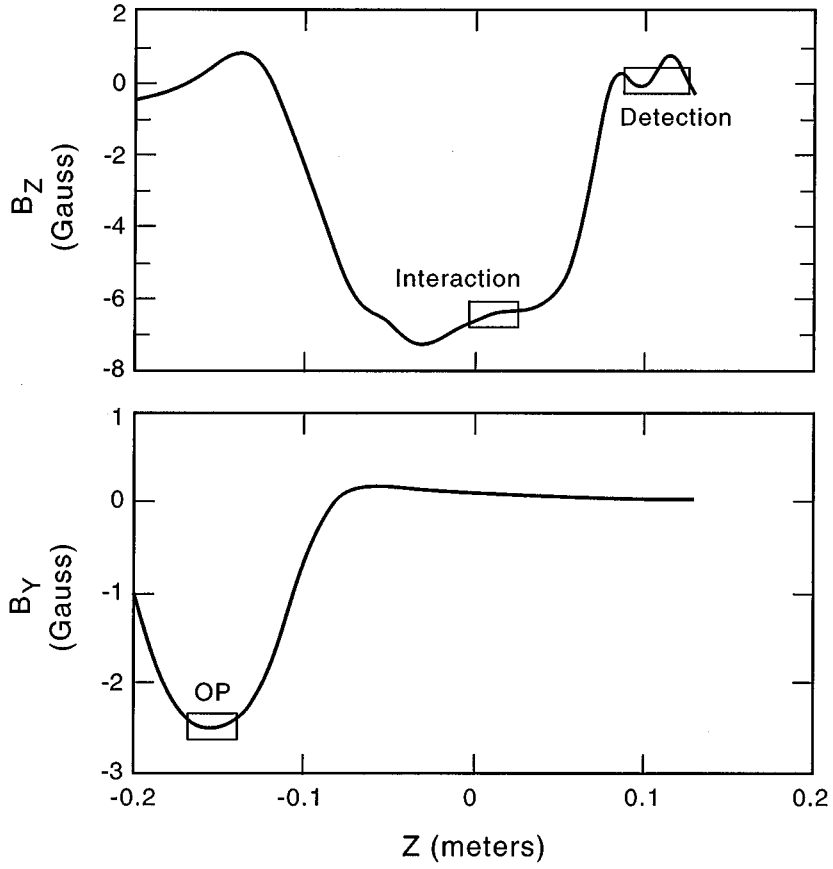

the optical cavity, we use two pairs of coils (labeled 4 and 5) to shim out the B_x and B_y fields. To null any magnetic field gradients along the y axis in the interaction region, we use what we call an "interaction smoothing coil" (labeled 6), which is narrow in the y dimension and wide in the x dimension. Thus, the field experienced by the cesium atoms resembles that produced by two current bars. The magnetic field in the interaction region resulting from coil 6 consists of two nonuniform components: $\partial B_z/\partial y(\hat{z})$ and $\partial B_y/\partial y(\hat{y})$, that is, components B_z and the B_y that vary as a function of y. Although the variation in the z component of B does not affect our experiment, the variation in the y component does. A detailed discussion of the effect of $\partial B_y/\partial y$ is given in Sect. 5.

To control $\partial B_y/\partial y$, $\partial(\Delta B_y)/\partial y$, and $\partial A_y/\partial y$, where A_y refers to the y component of the magnetic field generated by the "optical pumping coils" that leaks into the interaction region, we vary the current through the smoothing coil and reverse one of its components synchronous with both the a- and b-reversals.

Besides the problem of gradients in the y and z components of $\boldsymbol{B}$ along the y direction in the interaction region, there can be a gradient in the x component along this direction as well, $\partial(B_x)/\partial y$, which arises if the PBC is not centered with respect to coils 4 and 5 (used to null B_x and B_y). To null the gradient in the x component of both the applied magnetic field, $\partial(B_x)/\partial y$, and the stray (nonreversing) magnetic field, $\partial(\Delta B_x)/\partial y$, we use four coils, labeled 7, which are long in the z direction and together produce a uniform gradient $\partial(B_x)/\partial y$ in the interaction region. A discussion of the effect of $\partial(B_x)/\partial y$

©1999 NRC Canada

is given in Sect. 5. Note that the magnitude of A_x is negligible in this region.

Magnetic field in the detection region— Since we want to detect atoms in a particular hyperfine state regardless of magnetic sublevel, we want the magnetic field in this region to be small enough so that the Zeeman shifts are less than the transition linewidth. Thus, we want to generate a magnetic field that cancels any leakage from the field generated in the interaction region but does not change the field in the interaction region.

There is a third criterion that the magnetic field generated in the detection region needs to satisfy, which concerns detection of atoms via the cycling transition between the 6S $F_{\rm det} = 3$ and $6P_{3/2} F' = 2$ states. Atoms undergoing this cycling transition can evolve into a nonabsorbing "dark state" and thus be lost to detection. To prevent this loss process, we spatially vary both the magnetic field and the polarization of the optical field. The polarization of the optical field is discussed in Sect. 3.4.3.

To produce a weak, nonuniform, magnetic field in the detection region that has negligible effect in the interaction region, we use a pair of "detection coils," labeled 8 in Fig. 13, which are long in the y direction and narrow in the x direction. This causes the net magnetic field in the detection region to drop to near zero, while not affecting the field in the interaction region. The resulting small magnetic field in the detection region reverses direction twice along the cesium beam direction, as shown in Fig. 14.

It is also important to minimize B_y in the detection region, for if both a y component of the magnetic field and a circularly polarized component of the probe-laser polarization are present, then the atoms may be preferentially optically pumped to a particular magnetic sublevel, which would cause our detection technique to be sensitive to the magnetic quantum number.

3.6. Data acquisition electronics

We detect atoms that have undergone a transition between the 6S and 7S states by letting them decay to the previously emptied 6S $F_{\rm det}$ hyperfine state, driving a cycling transition from $F_{\rm det}$ to a $6P_{3/2}$ hyperfine state, and collecting photons scattered by those atoms in the detection region. A typical signal is 200 nA for the $F = 3 \rightarrow 4$ transition and 85 nA for the $F = 4 \rightarrow 3$ transtion. We change the handedness of the interaction region in one of five ways: by reversing either the direction of the electric field (e-reversal), the handedness of the dye-laser polarization (p-reversal), the direction of the magnetic field in the interaction region (b-reversal), the direction of the magnetic field in the optical pumping region (a-reversal), or the direction of the Zeeman pump-laser polarization (m-reversal). Each of these reversals can cause a change in the transition rate, which we detect as a change in the photocurrent. We use a phase-sensitive gated-integration detection technique to extract modulations in the signal that are synchronous with modulations in the reversals, and to gate out any transients in the signal due to these reversals.

3.6.1. Modulation of the field reversals

Each of the five coordinate-system reversals has associated with it a transient, the duration of which, relative to the period of the reversal, determines the duty cycle for that reversal. The e-reversal has the shortest transient and hence is made the fastest. To control the frequency of this fast reversal, we use a programmable counter/time board (Keithley CTM-05). As shown in Fig. 15, the timer board generates a square wave (27 Hz), which controls the e-reversal, as well as "gate" and "reset" pulses, which control two gated integrators.

The timing for the other four reversals is done with software and is referenced to this fast reversal. We modulate the direction of the magnetic field in the optical pumping region (a-reversal) at 0.29 Hz, the handedness of the dye-laser polarization (p-reversal) at 0.07 Hz, the direction of the magnetic field in the interaction region (b-reversal) at 0.018 Hz, and the direction of the polarization of the Zeeman pump laser (m-reversal) at 0.004 Hz. We randomly shift the relative phases of these reversals.

©1999 NRC Canada

Fig. 15. Block diagram of the data acquisition system. The counter-timer board controls the timing of both the coordinate-system reversals and the signal detection. Note that we separate the signal into two channels, one to detect the whole signal and thus monitor drifts, the other to detect only the modulation. Both signals are gated, integrated, and then sent to a computer.

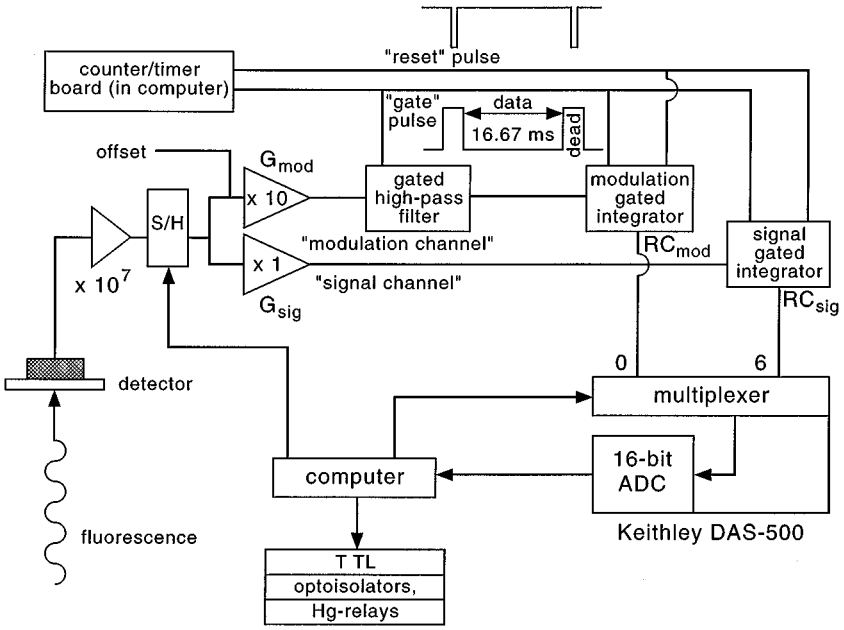

To protect the computers from electrical transients, all the square waves except the one used to drive the m-reversal are first sent to opto-isolators, which then drive mercury-wetted relays. The m-reversal is driven by a stepper motor.

Although the electric-field reversal is the most frequent, there are certain measurements, such as alignment of the fields in the interaction region, for which the e-reversal cannot be used as the reference signal. Moreover, some of the important modulations required for alignment are not synchronous with the e-reversal. For such situations, we use either the p- or a-reversal as the most frequent reversal, for the m-reversal is too slow and the b-reversal has long transients.

The overall duty cycle for PNC data acquisition is 61%. This is primarily limited by the long gate-out times that we use to avoid the transients from the a- and b-reversals.

3.6.2. Gated-integration detection

To optimize the detection sensitivity to small modulations on a large DC signal, we separate the signal from the detector into two channels, as shown in Fig. 15, where the "signal" channel consists of the total signal, and the "modulation" channel consists of the total signal with a large DC offset that subtracts off the part of the signal that does not modulate. The remaining part of the modulation-channel signal is then amplified by a factor of 10. We use the signal channel to keep track of drifts and backgrounds, and the modulation channel to determine the signal modulation.

Each channel is then sent to a gated integrator. The gate pulse, shown in Fig. 15, is controlled by the counter/timer board to coincide with the e-reversal. The "data interval," or time over which the signal is integrated, is set to 16.67 ms, the period of 60 Hz noise, so that a full cycle of 60 Hz noise is cancelled for every integration. The duration of the gate pulse, or "dead time" (1.85 ms), is chosen so that the

©1999 NRC Canada

Fig. 16. Gated high-pass filter (3 dB frequency of 8.5 Hz) used for the modulation channel. During the time when the signal is not being integrated, the voltage on the capacitor is held constant (but not grounded) so that information about the size of the input channel is preserved.

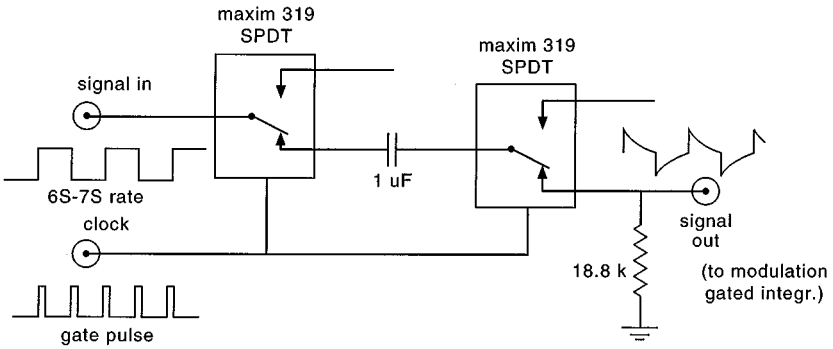

transient from the e-reversal (1.50 ms duration) is gated out of the signal. During the gate pulse, the integrated signal is sent to the computer. The 200 μs "reset" pulse is sent to the integrator just before the start of the next integration to reset the integrated signal value to zero. In a similar manner, but with different timings, we gate out the transients due to the other four reversals.

Since the signal from the detector is also used for locking the frequency of the Invar cavity to the atomic transition frequency, any transients in this signal can affect the dye-laser frequency. Therefore, we gate out each transient from the signal that goes to the lockin amplifier used for the Invar-cavity frequency lock. While the transient occurs, a sample and hold (S/H) circuit maintains the last, pretransient value for the lockin input signal. Then, after the transient is gone, the S/H circuit switches back to the true signal.

The noise on the 6S–7S transition square-wave modulation is higher than the noise at 27 Hz as observed on a spectrum analyzer. This discrepancy occurs because the square wave that defines the timing, as shown by Fourier analysis, is actually a square wave of 27 Hz embedded in a square wave of much lower frequency (1 Hz), embedded in a square wave of even lower frequency, and so on. As a result, though our detection bandwidth is centered on 27 Hz, it has smaller lobes as well at much lower frequencies, where $1/f$ noise is much larger.

To eliminate the noise arising from these lobes we replace the DC detection system on the modulation channel with a gated AC high-pass filter (3 dB frequency at 8.5 Hz), shown in Fig. 16. As a result, very-low-frequency contributions are attenuated. With this improvement, we regularly attain a shot-noise-limited signal-to-noise ratio on the transition-rate modulations. Since this high-pass filter essentially takes the derivative of the input square wave, leading to a distortion in the edges of the output wave form, as shown in Fig. 16, it is especially important to gate this high-pass filter synchronously with the gated integrators, so that no information is lost. Also we carefully calibrate how this affects the measured fractional modulation.

We embed this filter in a sample-and-hold circuit, which maintains the charge on the capacitor during the "dead time," rather than grounding it, to generate an AC wave form that is nearly equivalent to the originally input DC wave form, though with attenuation and reduced $1/f$ noise. Since the DC contribution to the modulation channel is now zero, we must use the signal channel to detect modulations of the signal that do not involve the e-reversal. However, since all relevant modulations occur with the e-reversal, this consequence is not a problem.

The outputs from the gated integrators are sent to a multiplexer that forms the input stage of a Keithley DAS-500 data acquisition system. Each signal is digitized with a 16-bit analog-to-digital

©1999 NRC Canada

converter (ADC), and then stored. The 16-bit ADC ensures that bit noise is less than statistical noise.

Six quantities relevant to the data acquisition system must be calibrated: the time constants for the modulation and signal gated integrators (RC_{mod} and RC_{sig}, respectively); the electronic gains for the modulation and signal channels (G_{mod}, G_{sig}, respectively); the duration of the data interval (τ); and the attenuation of the high-pass filter (f). These quantities are shown in Fig. 15.

These six calibrations are performed by using a 1.5 V battery in place of the fluorescence signal; this voltage is close to the actual signal for the $\Delta F = \pm 1$ 6S–7S transitions. We require the data analysis program to give the same voltages as a calibrated Fluke 8505A digital voltmeter monitoring the same signal. In addition, we construct a PNC-mimicking circuit, which gives an adjustable calibration signal that modulates with all five of the coordinate system reversals. Here again, we use the artificial PNC modulation to calibrate the data acquisition system against the calibrated voltmeter.

4. Data acquisition and analysis

4.1. Procedure

We acquired PNC data over the course of eight months in five separate data runs. Each data run involved the apparatus operating continuously for between 96 and 144 h.

Before each data run, we perform the following set of auxiliary experiments, the purpose of which is to eliminate systematic errors, as explained in Sect. 5: we measure and align $\boldsymbol{E}$, $\boldsymbol{B}$, and the y component of their gradients in the interaction region; we measure and align the birefringence axes of the PBC output mirror; we measure and null out the polarization-dependent power modulation of the dye-laser beam that is synchronous with p-reversal; we measure the initial magnetic-sublevel populations of the cesium atomic beam as it enters the interaction region; and we measure the 6S–7S line shape.

After performing this set of auxiliary measurements, we lock the frequencies of each of the four lasers appropriately to study one 6S–7S hyperfine transition and then acquire data in blocks of between 1.5 to 2 h duration, each data block consisting of 16 sets of all reversals. At irregular intervals during a data run, we reset the four lasers to take data on the other hyperfine transition. During one data run, we typically acquire 25 data blocks, roughly an equal number for each of the two hyperfine transitions. Before each data block, we set (and measure) the polarization of the standing-wave field so that for each hyperfine transition, roughly equal amounts of data are acquired for the two polarization ratios $\epsilon_I/\epsilon_z = 1$ and 2. Moreover, during each data run, we rotate the PBC output mirror once or twice by 90^{o} so that an equal number of data blocks for each hyperfine transition is acquired at each output-mirror position.

After each data run, we repeat the auxiliary experiments to verify that they remain constant. In total, 106 data blocks were acquired for the $4 \rightarrow 3$ transition, and 71 for the $3 \rightarrow 4$ transition.

Each of the 16 sets making up one data block consists of 16 384 e-reversals (at 27 Hz), 256 a-reversals (at 0.29 Hz), 64 p-reversals (at 0.07 Hz), 16 b-reversals (at 0.018 Hz), and 4 m-reversals (at 0.004 Hz), and requires an integration time of 274 s. For each set, we use modulation patterns for the coordinate-system reversals that minimize the effect of any drifts. Since the modulation of the electric field (e-reversal) is determined by the square-wave pulse generated by the timing circuit, there are two possible modulation sequences, either $+-+-$ and so on, or $-+-+$ and so on. One of these sequences is selected at random by our computer program at the beginning of the set. To modulate the dye-laser polarization (p-reversal), we modulate the voltage on the Pockels cell. Since the temperature of the Pockels cell depends on the frequency of modulation, it is always run with a continuous square-wave modulation. In contrast to a square-wave modulation pattern, we modulate the remaining reversals, the magnetic field in the optical pumping region (a-reversal), the magnetic field in the interaction region (b-reversal), and the Zeeman-pump-laser polarization (m-reversal), with the pattern $+--+$, which helps to cancel drifts in the signal. We alter the initial state of the m-reversal, so that its modulation pattern alternates between $+--+$ and $-++-$.

©1999 NRC Canada

Fig. 17. Typical data showing modulation of the fluorescence signal with p-reversal. The fractional modulation, dP in this case, is found by dividing the difference in the signals by the sum of the signals. In (*a*) the m-reversal is in the + state, while in (*b*) it is in the - state. Note how the signal modulates in-phase with the p-reversal in (*a*), but out-of-phase with the p-reversal in (*b*). This modulation is due to several contributions, one of which is the actual PNC modulation, though that contribution is quite small, about half the size of the noise.

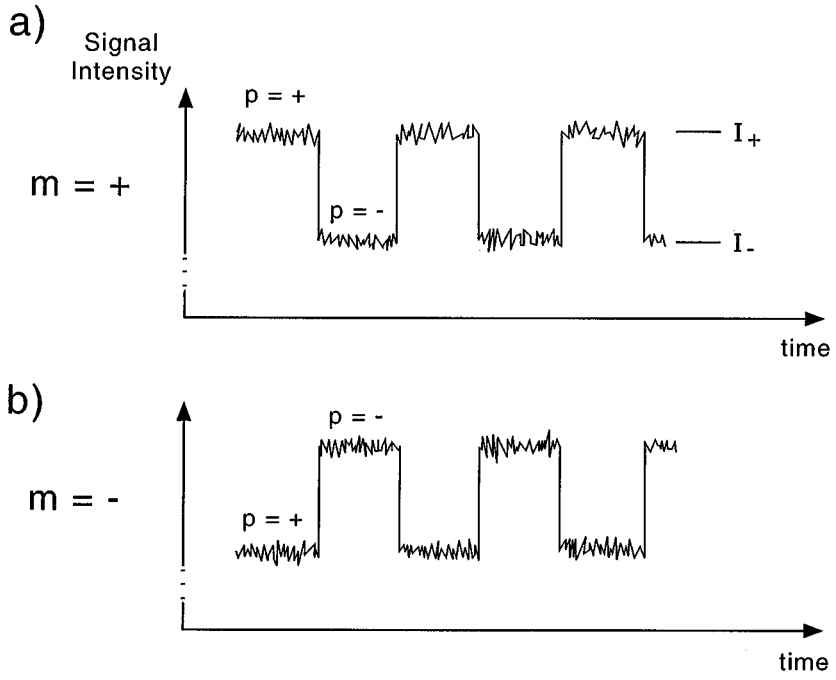

To reject large data disturbances, which occur when, for instance, a laser loses its servo lock, the computer regularly checks the noise. If, after 64 cycles of the fastest reversal (usually the e-reversal), the noise is found to be dramatically high (at least five times the level of typical noise), then the data is rejected and those 64 points are repeated. The computer also monitors whether the DC signal for each 64 cycles is anomalously low, indicating that one of the lasers has jumped off transition. If so, the computer stops the data run so that the laser can be relocked.

4.2. Typical signal

Figure 17 shows a typical signal when the handedness of the dye-laser polarization and the Zeeman-pump-laser polarization are modulated, (p- and m-reversal, respectively). In Fig. 17*a*, m is held in the "+" state and p is modulated, while in Fig. 17*b*, m is held in the "−" state and p is modulated. Note that in Fig. 17*a* the modulation of the signal intensity is in phase with the p-reversal, while in Fig. 17*b* it is out of phase.

We measure the fractional modulation of the 6S–7S transition signal that is synchronous with reversal of the coordinate-system handedness, that is, we measure the difference between the maximum and minimum signal intensities, $(I_{\max} - I_{\min})$, and then divide that by the sum of these signals, $(I_{\max} + I_{\min})$. The equation for the transition rate (10) then predicts that this experimental ratio is equal to the ratio of the Stark–PNC interference term to the main Stark term (neglecting systematic errors and assuming that the Stark–$M1$ interference term is negligible for our experimental configuration).

©1999 NRC Canada

The two primary concerns about the signal are the statistical S/N ratio and potential systematic errors that modulate in the same fashion as the Stark–PNC interference.

4.3. Analysis of signal modulation

There are many contributions to the signal modulation besides Stark–PNC interference. Contributions that modulate with all five reversals are systematic errors and are the primary concern. We label such contributions to the signal "$dEPBMA$," where the "d" represents the fractional modulation and the "E," "P," "B," "M," and "A" represent the reversals with which this modulation is synchronous (electric-field direction, handedness of the dye-laser polarization, magnetic-field direction in the interaction region, handedness of the Zeeman-pump polarization, and magnetic-field direction in the optical pumping region, respectively). We use upper-case letters so as not to confuse these labels with the flipping parameters (e, p, b, m, and a).

Contributions to the signal that modulate with only some of the reversals are labeled accordingly. For example, we label contributions to the signal that modulate only with p-reversal "dP," contributions that modulate only with p and m "dPM," and so on.

We measure the fractional contribution to the signal that modulates with all five reversals by subtracting the signal intensities obtained for a net "$-$" coordinate-system handedness from the signal intensities obtained for a net "$+$" coordinate-system handedness and then dividing this difference by the sum of all the signal intensities, regardless of the handedness:

$$dEPMAB = \frac{\sum_{e,p,m,a,b} epmab\ I(e,\,p,\,m,\,a,\,b)}{\sum_{e,p,m,a,b} I(e,\,p,\,m,\,a,\,b)} \tag{12}$$

Here p, m, a, b, and e are the flipping parameters, equal to ± 1, and $I(e,\,p,\,m,\,a,\,b)$ is the intensity of the signal for a given set of flipping parameters. Note that the signal from the Stark–PNC interference is included in this modulation.

Similarly, we measure the fractional contribution to the signal that modulates with only the p- and m-reversals by subtracting the signal intensities obtained for a net "$-$" p- and m-reversal state, (that is, when the product pm is -1), from the signal intensities obtained for a net "$+$" p- and m-reversal state, (that is, when pm is $+1$), and then dividing this difference by the sum of all the signal intensities, regardless of the handedness:

$$dPM = \frac{\sum_{e,p,m,a,b} pm\ I(e,\,p,\,m,\,a,\,b)}{\sum_{e,p,m,a,b} I(e,\,p,\,m,\,a,\,b)} \tag{13}$$

Each fractional modulation provides us with information about the environment of the atoms. For example, the fractional modulation dE has a magnitude proportional to $\Delta E_x/E_x$ and thus its presence alerts us to the fact that there is a stray (nonreversing) component of the electric field in the x direction. The fractional modulation dP alerts us to any change in the ellipticity of the dye-laser polarization when the handedness of the polarization reverses, which arises when the x component of the polarization has a real part, ϵ_R. The fractional modulation $dPMA$, which occurs in the absence of the applied electric field E_y, represents the part of the modulation dP that depends on the dye-laser frequency; specifically, this modulation is due to the frequency-dependent birefringence of the PBC input mirror coating, which is caused by stress from the PZT. The fractional modulation dEP has a magnitude that is proportional to $(\Delta E_z/E_x)(\epsilon_R/\epsilon_z)$ and so it too alerts us when the reversal of the dye-laser polarization is not perfect. Moreover, we find that this fractional modulation has a component that is proportional to the gradient of the y component of the magnetic field along the y direction, $\partial B_y/\partial y$, and thus alerts us to the presence of such a gradient. We find that the fractional modulations $dEPB$ and $dEPAB$ are also proportional to

©1999 NRC Canada

gradients in the fields, in particular $\partial(\Delta B_y)/\partial y$ and $\partial A_y/\partial y$, respectively, and so alert us to the extent of these gradients. We discuss systematic errors that contribute to the fractional modulation $dPEMBA$ in Sect. 5.

4.4. Sources of noise

We group noise sources into three categories: shot noise, background noise, and technical noise. Each of the noise sources scales in a different way with the DC electric field strength E, depending on how it scales with the Stark-induced signal. Shot noise scales as the square root of the Stark-induced signal and is thus proportional to E, while technical noise scales in proportion to the Stark-induced signal and thus is proportional to E^2, and background noise is independent of the Stark-induced signal and thus is independent of E. After years of previous work, the background and technical noise have been diminished, so that at present shot noise is the dominant source.

Since the main source of shot noise in the laser-induced-fluorescence signal is the fluctuation in the number of atoms that undergo the 6S–7S transition, we can use the measured shot noise to estimate the number of atoms undergoing the transition. For typical conditions, we measure the shot noise to be between 30 and 36 μV/$\sqrt{\text{Hz}}$ on a 2 V signal, or between 15 and 18 ppm/$\sqrt{\text{Hz}}$. This value corresponds to the detection of about 5×10^9 atoms/s, or 1/(15ppm/$\sqrt{\text{Hz}}$)^2. Since we detect only 65% of the atoms excited to the 7S state (because of branching ratios in the decay to the 6S $F = 3$ and $F = 4$ states) we estimate that the number of atoms being excited in the interaction region per second is 8×10^9.

We define "background noise" to be fluctuations in the "background" fluorescence signal that is present when the DC electric field is zero. This noise is primarily due to imperfect optical pumping, which leaves atoms in the previously emptied hyperfine state, also called the "detection" state. Under typical conditions, the photocurrent noise due to "background" atoms is 1 pA/$\sqrt{\text{Hz}}$, or 10 μV/(10 M$\Omega\sqrt{\text{Hz}}$), on an overall background photocurrent of 50 nA, or 0.5 V/10 MΩ. Although scattered laser light from both the probe laser and the PBC contributes an additional 0.15 V/10 MΩ to the background signal, this does not contribute significantly to the noise.

Sources of technical noise include: frequency and intensity noise on all the lasers; fluctuations in the spin polarization, because of insufficient power in the optical pumping lasers; voltage noise on the Pockels cell; noise associated with the power supply for the electric-field plates; noise due to building vibrations; and fluctuations in the atomic beam flux. Since technical noise is proportional to the signal intensity, we measure it by increasing the signal so that it dominates the shot and background noise. To obtain a large signal, we excite the $\Delta F = 0$ 6S–7S transition and increase the electric field to 1 000 V/cm. Under these conditions, we find that for most sources of technical noise, the frequency-dependence of the noise either scales as $1/f$ or peaks at a specific frequency. Since, at our specific PNC detection frequency, the technical noise is typically 6 to 7 ppm/$\sqrt{\text{Hz}}$, its contribution to the overall noise is small under normal PNC running conditions.

4.5. PNC Signal-to-noise ratio

Since the Stark–PNC interference term is linearly proportional to E, we can write for the signal-to-noise ratio:

$$\frac{PNC}{total\ noise} \propto \frac{E}{\sqrt{(g)^2 + (sE)^2 + (tE^2)^2}} \tag{14}$$

where PNC represents the fractional modulation due only to the Stark–PNC interference, g represents the background noise, sE the shot noise, and tE^2 the technical noise. The value of E that maximizes this signal-to-noise is $E_{\max} = \sqrt{g/t}$. Figure 18, shows a plot of the three types of noise and the total noise as a function of the electric field, E. Note that rather than plotting the noise directly, we plot the noise divided by E, which corresponds to the inverse of the signal-to-noise ratio given in (14), and thus is the quantity that we want to minimize. We also plot the PNC modulation divided by E for comparison.

©1999 NRC Canada

Fig. 18. Plots of the noise sources and fractional PNC modulation signal integrated over 1 s as a function of electric field $\boldsymbol{E}$, for a dye-laser polarization ratio ϵ_I/ϵ_z of 1. We actually plot the noise (or fractional PNC modulation signal) divided by E, which gives a quantity that is inversely proportional to the signal-to-noise ratio. To get the total noise, we add the three noise contributions in quadrature. We take data near the minimum for [(total noise)/E], at electric-field values ranging from 400 to 600 V/cm.

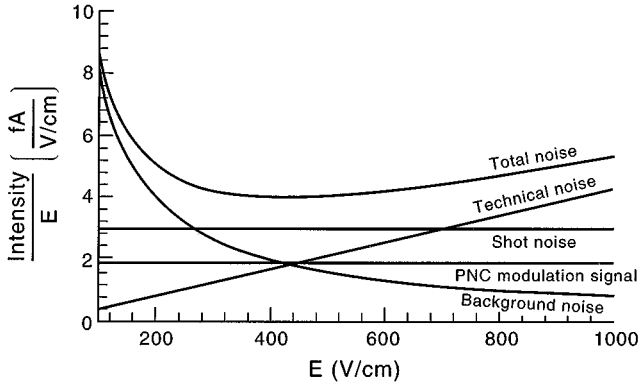

The plot of $(totalnoise)/E$ shows a minimum at $E = 450$ V/cm where the signal-to-noise ratio is $0.5/\sqrt{\text{Hz}}$. The fact that the total noise is rather flat in this region indicates that it is dominated by shot noise.

The plots in Fig. 18 are for the case of a circularly polarized dye laser ($\epsilon_I/\epsilon_z = 1$). For data runs taken with elliptical polarization, ($\epsilon_I/\epsilon_z = 2$), the optimum E is higher (about 900 V/cm) and the fractional modulation due to Stark–PNC interference increases from 6.5 to 8.2 ppm, resulting in an increase in the signal-to-noise ratio by about a factor of 1.26.

The dependence of the signal on the dye-laser polarization is important for three reasons. First, as just mentioned, by changing the ratio of the dye-laser polarization components ϵ_I/ϵ_z from 1 to 2, we increase the PNC fractional modulation from 6.5 to 8.2 ppm, which represents a factor of three improvement over the PNC fractional modulation achieved in our 1988 measurement. (Note that we do not let the polarization ratio exceed 2 because the required electric field would exceed 1000 V/cm, which is too large for our mercury-wetted relays.) Second, since both the $M1$ amplitude and the $(E1_{\text{Stark}})$ amplitude scale with dye-laser polarization in the same way, the fractional modulation from the Stark–$M1$ interference term is independent of the dye-laser polarization. Indeed, when ϵ_I/ϵ_z is changed from 1 to 2, the ratio of the Stark–PNC interference term to any Stark–$M1$ interference term increases by a factor of two. As a consequence, potential systematic errors arising from the Stark–$M1$ interference are reduced relative to the Stark–PNC interference. A third consequence of the polarization dependence is that it can be used as a check on the experiment, for if our final PNC value is the same for the two polarizations, ($\epsilon_I/\epsilon_z = 1$ or 2), then we are assured that there is no undetected Stark–$M1$ interference signal that is contributing to the PNC signal.

5. Systematic errors

Here we describe systematic errors due to contributions to the signal that modulate with all five reversals (and thus mimic the Stark–PNC interference). Our approach is to first calculate how misaligned electric and magnetic fields ($\boldsymbol{E}$ and $\boldsymbol{B}$) and dye-laser polarization ($\boldsymbol{\epsilon}$) can affect the transition rates; we also allow for the possibility that each of these components has both a reversing part and a nonreversing (which

©1999 NRC Canada

we call "stray") part. We then discuss how we measure and control the relevant field components so that these systematic errors are held at an acceptable level. Following that discussion, we cover calibration corrections to the PNC signal due to effects such as imperfect optical pumping and saturation of the transitions.

5.1. Effect of imperfectly aligned fields on the transition rates

There are several sources of (undesirable) DC electric fields in the interaction region. For example, areas differing in potential can build up at random on the electric-field plates ("patch effect") and cause permanent electric fields that are typically 100 mV/cm or less. Another source of permanent electric fields is nearby unshielded dielectric materials. We call such permanent fields, which do not reverse in direction when the applied voltage reverses, "stray" fields and label them $\Delta \boldsymbol{E}$. Nonreversing, or "stray," magnetic fields, $\Delta \boldsymbol{B}$, can occur as well, because of the Earth's magnetic field, local laboratory magnetic fields, and imperfections in optical components. And the dye-laser polarization can have a nonreversing, real, x component, ϵ_R, because of imperfect alignment.

Taking stray fields into account, we obtain the resulting equations for the electric and magnetic fields and the dye-laser beam polarization

$$\begin{aligned}
\boldsymbol{E} &= (eE_x + \Delta E_x)\hat{x} + (eE_y + \Delta E_y)\hat{y} + \Delta E_z \hat{z} \\
\boldsymbol{B} &= (bB_x + \Delta B_x + aA_x)\hat{x} + (bB_y + \Delta B_y + aA_y)\hat{y} + (bB_z + \Delta B_z + aA_z)\hat{z} \\
\boldsymbol{\epsilon} &= (\epsilon_z)\hat{z} + (\epsilon_R + ip\epsilon_I)\hat{x}
\end{aligned} \tag{15}$$

where the flipping parameters e, b, and p are ± 1, depending on the direction of the electric and magnetic fields and the handedness of the dye-laser polarization, respectively. Note that there is no y component of dye-laser polarization because we define the y axis as being along the direction of propagation of the dye-laser beam. Note also that there is no z component of the reversing electric field, for since the x axis is defined as being along the component of the reversing part of $\boldsymbol{E}$ that is perpendicular to y, E_z is zero by definition. However, since there can be a component of $\boldsymbol{E}$ along the z direction that does not reverse, we include that component in (15).

There are additional magnetic-field components that are due to contamination from the magnetic field in the optical pumping region and that thus reverse synchronously with the reversal of that magnetic field (a-reversal). We label these additional terms aA_x, aA_y, and aA_z, where a is the fourth flipping parameter and is equal to ± 1 depending on the direction of the magnetic field in the optical pumping region.

To calculate how the field misalignments in (15) affect the transition amplitudes, we modify the equations for the three transition amplitudes. Specifically, we treat the effect of the misaligned magnetic field on the initial-state wave function with perturbation theory, and replace the electric field by the expression for $\boldsymbol{E}$ in (15). We then obtain new expressions for the $\Delta F = 0, \pm 1$ transition rates between the 6S and 7S states. The rate for the pure Stark-induced transition is given in Appendix C.

5.2. Systematic errors that mimic Stark–PNC interference

Here we describe contributions to the signal that modulate with all five reversals and thus mimic the Stark–PNC interference signal. We divide these error sources into two groups: "common errors" which are common to both hyperfine transitions, and "differential errors" which have a different magnitude for each hyperfine transition. For each error source, we describe how we constrain the error so that its contribution to the PNC modulation is no greater than 0.3%. Although the Stark–$M1$ interference modulates with only four of the reversals (all except the p-reversal), we include this interference in our discussion because it can acquire a dependence on the p-reversal and thus become a systematic error.

For clarity of discussion, we suppress the flipping parameters in this section, since by definition systematic errors modulate with all five.

©1999 NRC Canada

5.2.1. Systematic errors common to both hyperfine transitions

Systematic errors that cause the signal from both hyperfine transitions to shift by the same amount, which we call common errors, lead to an error in the extraction of the weak nuclear charge, Q_W, though not in the extraction of the anapole moment. Sources of this type of systematic error include imperfect alignment of the fields defining the coordinate system, which we call "coordinate systematics," and imperfect reversals that have the same effect on each hyperfine line, which we call "direct couplings."

$E_y \Delta E_z$ systematic error Consider the fourth term in the equation for the fractional, pure, Stark-induced transition rate, (C2). This term arises from both a misalignment of the electric field, resulting in a component E_y along the direction of the dye laser, and the presence of a stray electric field in the z direction ΔE_z. This type of systematic error was recognized previously by several groups [16, 31].

For an electric field of 500 V/cm and a dye-laser polarization ratio ϵ_I/ϵ_z of 1, the fractional Stark–PNC interference modulation is 6 ppm. Thus, to meet the requirement that this systematic error be less than 0.3% of the PNC fractional modulation for typical stray electric fields that are no greater than 100 mV/cm, the ratio E_y/E_x must satisfy:

$$2\frac{E_y}{E_x}\frac{\Delta E_z}{E_x}\frac{\epsilon_I}{\epsilon_z} = 2\frac{E_y}{E_x}\frac{0.1}{500} < (0.003)(\text{PNC}) = 1.8\times 10^{-8} \tag{16}$$

Thus, the ratio E_y/E_x must be $< 45\times 10^{-6}$. To meet this limit with an electric field, E_x, of 500 V/cm, the component in the y direction, E_y (due to misalignment), must be < 22 mV/cm.

To minimize the ratio E_y/E_x, we make use of the modulation $dPMAB$. A major contribution to this modulation comes from the seventh term in the equation for the fractional, pure, Stark-induced transition rate, (C2), specifically:

$$dPMAB = 2\frac{E_y}{E_x}\frac{B_x}{B_z}\frac{\epsilon_I}{\epsilon_z} \tag{17}$$

where we approximate B as B_z. We maximize this modulation signal by applying a large, uniform B_x field with the shim coils (Fig. 13), being careful to keep E_y at a nonzero value. We then tilt the electric-field plates relative to the intracavity dye-laser beam to null out the observed modulation; this minimizes the ratio E_y/E_x. To obtain the required $E_y < 22$ mV/cm for our typical conditions of $B_x = 1$ G, $E_x = 500$ V/cm, $\epsilon_I/\epsilon_z = 1$, and $B_z = 6.4$ G, we adjust the plates so that the fractional modulation $dPMAB$ is < 14 ppm.

This procedure for minimizing E_y/E_x is complicated by the fact that there is an additional contribution to the fractional modulation $dPMAB$ that is proportional to B_y. We suspect that this contribution is due to the m-dependent (tensor) Stark shift. The fractional modulation $dPMAB$ is then

$$dPMAB = 2\frac{E_y}{E_x}\frac{B_x}{B_z}\frac{\epsilon_I}{\epsilon_z} + k\frac{B_y}{B_z}\frac{\epsilon_I}{\epsilon_z} \tag{18}$$

where k is a measured constant and is 0.03. This additional term is an example of a systematic error on a diagnostic measurement that is used to control a systematic error.

Before tilting the electric-field plates to minimize E_y/E_x, we make this second term negligible by decreasing B_y to less than 1 mG. To decrease B_y, we excite the $\Delta F = 0$ transition and monitor the α/β interference term in (C1), which has a strong dependence on B_y; this interference term was used in ref. 32 to measure the ratio α/β. Care is then taken to ensure that there is no additional B_y created when the large B_x is applied.

$B_x \Delta E_y$ systematic error Another systematic error arises (from the seventh term in (C2)) when there is a misalignment of the magnetic field in the x direction, B_x, and a stray electric field in the y direction,

©1999 NRC Canada

ΔE_y. Using arguments similar to those above, and the same experimental conditions, a decrease in this error to less than 0.3% of the fractional Stark–PNC interference modulation requires

$$2\frac{\Delta E_y}{E_x}\frac{B_x}{B_z} < 1.8 \times 10^{-8} \tag{19}$$

which is satisfied when B_x/B_z <45×10^{-6}. Since for our conditions $B_z = 6.4$ G, we require $B_x < 290\mu$G.

To meet this requirement on B_x, we first maximize the modulation signal $dPMAB$ by using the segmented field plates to apply a large E_y (25 V/cm), and then use a procedure similar to that described above. We minimize the observed modulation signal by using the shim coils to decrease B_x. To obtain $B_x = 290\mu$G under our experimental conditions, the fractional modulation $dPMAB$ must then meet the requirement:

$$dPMAB = 2\frac{E_y}{E_x}\frac{B_x}{B_z}\frac{\epsilon_I}{\epsilon_z} = 2\frac{25}{500}\frac{290 \times 10^{-6}}{6.4} = 5 \quad \text{ppm} \tag{20}$$

with B_y made small enough to neglect the additional term shown in (18).

However, there is an additional contribution to the fractional modulation $dPMAB$ that can arise when we use the electric-field-plate segments to generate E_y for the purpose of nulling B_x. If the lines delineating the electric-field-plate segments are not perpendicular to the dye-laser beam, the segments will generate electric fields in both the y and z directions, E_y and E_z, both of which reverse with the e-reversal. (Note that this only occurs during our diagnostic test, not during the actual PNC data runs). As a result, there will be an additional contribution to the dPMAB modulation that mimics the fourth term in the rate for the pure Stark-induced transition, (C2), but with the nonreversing ΔE_z replaced by the reversing E_z. Since this replacement gives the contribution a second factor that reverse with e-reversal, the two factors cancel, causing the contribution to modulate not as $dEPMAB$ but as $dPMAB$.

This modulation then mimics the expected $dPMAB$ modulation in our diagnostic test, and so is another example of a systematic error on a diagnostic test for a systematic error. The total dPMAB modulation for this diagnostic test can be written as

$$dPMAB = \left[2\frac{E_y}{E_x}\frac{B_x}{B_z} + 2\frac{E_y}{E_x}\frac{E_z}{E_x} + k\frac{B_y}{B_z}\right]\frac{\epsilon_I}{\epsilon_z} \tag{21}$$

Note that the first term modulates with E_x and E_y, while the second term modulates with E_y and E_z, and the third term does not modulate at all with the electric field. With our segmented electric-field plates, we can independently modulate E_x and E_y, and thus distinguish between these three contributions to $dPMAB$.

$\partial(B_x)/\partial y$ $\partial\Delta E_y/\partial y$ systematic error The final coordinate systematic error relates to the $B_x\Delta E_y$ systematic error described above. When two fields couple, as in the case of the $B_x\Delta E_y$ interference term, systematic errors arise if both fields have gradients, even if their spatially averaged fields are zero.

A gradient in the y component of the stray electric field, $\partial(\Delta E_y)/\partial y$, is generated by the inhomogeneous deposition of cesium on the electric-field plates by the cesium beam. (Gradients in the other two components of the stray field are insignificant). The resulting gradient is quite symmetric across the interaction region and its magnitude $\partial(\Delta E_y)/\partial y$ varies over time between 100 and 400 mV/cm^2.

A gradient in the x component of the magnetic field, $\partial(B_x)/\partial y$, is generated when the intracavity laser beam is not well centered on the B_x and B_y shim coils. Both simulations and measurements show that $\partial(B_x)/\partial y$ ranges between 1 and 5 mG/cm.

We have characterized these gradients and the resulting modulations in two ways. In one method, we map out each gradient across the atomic beam by blocking sections of the atomic beam, measuring the average fields ΔE_y and B_x over the sections of the beam that are not blocked, and calculating the

©1999 NRC Canada

gradients. In the other method, we directly apply a large gradient $\partial\Delta(E_y)/\partial y$ using the segmented field plates, and a large gradient $\partial(B_x)/\partial y$ using the B_x shim coils operated in anti-Helmholtz configuration, and then calibrate their contribution to the fractional modulation $dEPMBA$.

To minimize this systematic error, we first minimize $\partial(B_x)/\partial y$ by centering the dye-laser beam with respect to the B_x and B_y shim coils. Then, we cancel any remaining contribution by using the B_x gradient coils to generate an opposing $\partial(B_x)/\partial y$. To measure $\partial(B_x)/\partial y$, we block sections of the atomic beam, measure B_x using the modulation $dPMAB$ with a large applied E_y, and then calculate the gradient. Similarly, we measure $\partial\Delta(E_y)/\partial y$ by blocking sections of the atomic beam, measuring $\Delta(E_y)$ using $dEPMA$ with a large applied B_x, and then calculating the gradient. We then calculate the contribution of this gradient–gradient systematic error to the $dEPMAB$ modulation as in ref. 33. By keeping $\partial(\Delta E_y)/\partial y < 150$ mV/cm^2 and $\partial(B_x)/\partial y < 0.5$ mG/cm, we keep this contribution below 0.2% of the Stark–PNC fractional modulation:

$$\frac{1}{12}\frac{[\partial(\Delta E_y)/\partial y]L_y}{E_x}\frac{[\partial(B_x)/\partial y]L_y}{B_z} = \frac{1}{3}\frac{[0.15]}{500}\frac{[0.0005]}{6.4} = 8\times 10^{-9} \tag{22}$$

where L_y is the length of the interaction region, $\simeq 2$ cm. In cases where the gradient $\partial(\Delta E_y)/\partial y$ is greater than 100 mV/cm^2 (which occurs only when the plates are relatively new), we cancel it using the segmented electric-field plates. During the actual PNC data runs, the plates were sufficiently aged that the gradient was low and so this cancellation was not necessary.

5.2.2. Systematic errors due to imperfect reversals: Direct coupling errors

So far we have described systematic errors that arise from the coupling of a misaligned field (either E_y or B_x) and an imperfect reversal (due, for instance, to a stray field). Here we discuss systematic errors that arise from the coupling of two or more imperfect reversals; we call this type of systematic error a "direct coupling" error.

From (9), the pure, Stark-induced, $\Delta F = \pm 1$, 6S– transition rate is proportional to the square of β, the square of the reversible electric field, and the square of the z component of the dye-laser polarization:

$$R \sim \beta^2 E^2 \epsilon_z^2 f_3 \tag{23}$$

where we account for incomplete optical pumping by including the factor f_m, the fractional population in the initial cesium magnetic sublevel. For clarity, consider here the case of $m = 3$. If the e-, p-, and m-reversals are not perfect, there will be, respectively, a portion of the electric field that is nonreversing (ΔE), a portion of the z component of dye-laser polarization that is nonreversing ($\Delta\epsilon_z$), and a portion of the population in $m = 3$ that is nonreversing (Δf_3). Under such conditions, the pure, Stark-induced, transition rate can be written as

$$\begin{aligned} R &\sim \beta^2(E+\Delta E)^2(\epsilon_z+\Delta\epsilon_z)^2(f_3+\Delta f_3) \\ &\sim \beta^2 E^2\epsilon_z^2 f_3\left(1+\frac{\Delta E}{2E}\right)\left(1+\frac{\Delta\epsilon_z}{2\epsilon_z}\right)\left(1+\frac{\Delta f_3}{f_3}\right) \\ &\sim \beta^2 E^2\epsilon_z^2 f_3\,(1+dE)^2\,(1+dP)^2\,(1+dM) \\ &\sim \beta^2 E^2\epsilon_z^2 f_3\,(1+dE+dP+dM+dEdP+dEdM+dPdM+dEdPdM) \end{aligned} \tag{24}$$

where we have dropped higher order terms and ignored any background signal. Note that the term $\Delta E/E$ contributes to the fractional modulation dE because the denominator modulates with the e-reversal. Similarly, if all five reversals are not perfect, they will contribute to the fractional modulation $dEPMBA$ and thus result in a systematic error that is proportional to the product of five nonreversing components. It is easy to make this contribution negligible compared to the Stark–PNC interference.

©1999 NRC Canada

There is another source of systematic error that comes from the coupling of the Stark–$M1$ interference (which arises from imperfect atomic beam alignment and modulates as $dEMAB$) with an imperfect p-reversal (which modulates as dP). For our experimental conditions, $dP < 1 \times 10^{-3}$ and $dEMAB < 1 \times 10^{-4}$, so that this systematic error is less than 2% for each 10 min data block, which is acceptably low when compared with our statistical uncertainty of 18%. Moreover, since both dP and $dEMAB$ are both stabilized around zero and thus drift back and forth through zero over the course of several hours, this systematic error averages away.

5.2.3. Systematic error due to birefringence in the PBC output-mirror coating

The advantage of using multiple passes of the 6S–7S excitation light was recognized in 1981 [34], for while the Stark–$M1$ interference changes sign with the wave vector, $\vec{k}$, and thus cancels itself out, the Stark–PNC interference term is enhanced. However, the presence of birefringence in the output mirror causes the reflected wave to have a slightly different polarization than the incident wave, thus making the cancellation imperfect. The resulting small Stark–$M1$ interference term will modulate with p-reversal as well, thus creating a systematic error.

To account for this systematic error, we consider the spatial dependence of the dye-laser beam's oscillating electric and magnetic fields inside our PBC; a complete analysis of such a system can be found in ref. 35. The spatial dependence of the Stark–$M1$ interference term is then given by

$$R_{\text{Stark}-M1}(y) = \beta E_x M1 \left(C_{Fm}^{F'm'}\right)^2 \left(\delta_{m'm-1} - \delta_{m'm+1}\right) \left[\epsilon_z(y) B^*_{ac_x}(y) + \epsilon_z^*(y) B_{ac_x}(y)\right] \tag{25}$$

where B_{ac} is the oscillating magnetic field of the dye-laser beam. Taking into account the birefringence of the PBC output mirror, a spatial average of this rate gives

$$\bar{R}_{\text{Stark}-M1} = \beta E_x M1 \left(C_{Fm}^{F'm'}\right)^2 \left[2\epsilon_z^2(1-r) - \epsilon_z \epsilon_I \varphi_2 \sin 2\theta_2\right] \tag{26}$$

where φ_2 is the birefringence of the output-mirror coating, θ_2 is the angle of the coating's birefringence axes relative to the z axis, and r is the output-mirror reflectivity. Since the term involving φ_2 has a dependence on ϵ_I, it modulates with the p-reversal, thus causing the Stark–$M1$ interference term to become a systematic error.

The ratio of this systematic error to the Stark–PNC interference term is given by

$$\frac{\bar{R}_{\text{Stark}-M1}}{R_{\text{Stark}-\text{PNC}}} = \frac{\beta E_x M1 \epsilon_z \epsilon_I \varphi_2 \sin 2\theta_2 \left(C_{Fm}^{F'm'}\right)^2}{2\beta E_x \text{Im}(E1_{\text{PNC}}) \epsilon_z \epsilon_I \left(C_{Fm}^{F'm'}\right)^2} = \frac{M1 \varphi_2 \sin 2\theta_2}{2\text{Im}(E1_{\text{PNC}})} \tag{27}$$

To have this ratio be less than 0.005, given our values of $M1/\beta \simeq 32\,\text{V/cm}$, $\text{Im}(E1_{\text{PNC}})/\beta \simeq 1.6\,\text{V/cm}$, and $\varphi_2 \simeq 2\mu\text{rad}$, we require that θ_2 be $< 7^{\text{o}}$.

To measure the birefringence of the output-mirror coating, φ_2, and the angle of its axes relative to the z axis, θ_2, we use an optical technique [27], in which we shine circularly polarized light through the PBC and then through a polarizer. The intensity of the light transmitted, $I(\psi)$, as a function of the angle of the polarizer relative to the z axis, ψ, is given by

$$\frac{I(\psi)}{\bar{I}} = 1 \mp F_o \varphi_1 \sin(2\theta_1 + 2\psi) \mp F_o \varphi_2 \sin(2\theta_2 + 2\psi) \tag{28}$$

where $\theta_1(\theta_2)$ is the angle of the input (output) mirror birefringence axes relative to the z axis, F_o is the power buildup factor ($\simeq$finesse/π), the $\mp$ refers to initial right- and left-circular polarization of the dye laser, and we have normalized the signal with respect to the average intensity transmitted, $\bar{I}$.

Thus the birefringence causes the transmitted intensity to modulate as the handedness of the dye-laser polarization modulates. The modulation in the intensity of light transmitted, ΔI_p, can be written

©1999 NRC Canada

Fig. 19. Results from the technique used to determine the birefringence, ϕ, of each PBC mirror and the angle, θ, of the birefringence axes with respect to the z axis. The left-hand sides of (30) and (31) are plotted as a function of the angle ψ of the polarizer with respect to the z axis. The amplitude of each wave represents ϕ, while the phase shift represents θ. In this example, the output mirror birefringence is 2.2 μrad and its axes are aligned along the z axis to better than 5^o.

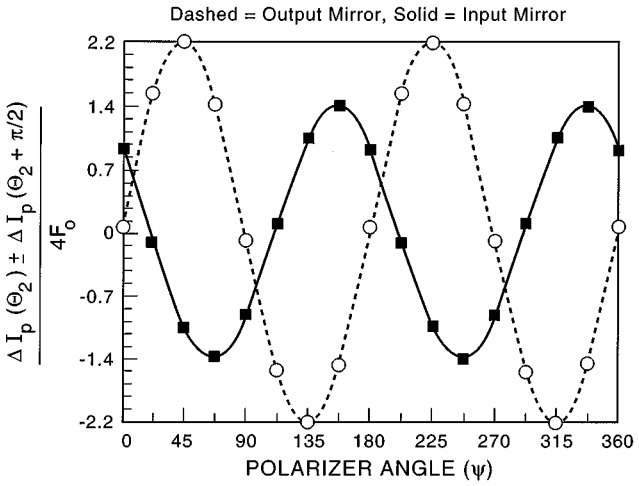

as the difference between the intensities transmitted for the initial right- and left-circularly polarized light:

$$\frac{\Delta I_p}{\bar{I}} = \frac{I_+ - I_-}{\bar{I}} = -2F_o\varphi_1 \sin(2\theta_1 + 2\psi) - 2F_o\varphi_2 \sin(2\theta_2 + 2\psi) \tag{29}$$

again normalized with respect to the average intensity transmitted. Now if the output mirror is rotated by 90^o, that is, if $\theta_2 \to \theta_2 + \pi/2$, then the sign of the second term will reverse. Thus, by measuring $\Delta I_p(\psi)$ at θ_2 and at $\theta_2 + \pi/2$, we can distinguish the parameters of the input mirror from those of the output mirror.

$$\frac{\Delta I_p(\theta_2) + \Delta I_p(\theta_2 + \pi/2)}{\bar{I}} = -4F_o\varphi_1 \sin(2\theta_1 + 2\psi) \tag{30}$$

$$\frac{\Delta I_p(\theta_2) - \Delta I_p(\theta_2 + \pi/2)}{\bar{I}} = 4F_o\varphi_2 \sin(2\theta_2 + 2\psi) \tag{31}$$

A plot of $(\Delta I_p(\theta_2) \pm \Delta I_p(\theta_2 + \pi/2))/(4F_o\bar{I})$ as a function of ψ, is shown in Fig. 19. From the amplitude of each plot we can determine the birefringence of each mirror, while from the phase shift of each plot we can determine the angle of the axes of that birefringence with respect to the z axis. Using this method, we can easily rotate the output mirror so that its birefringence axes are within 5^o of the z axis.

However, using this technique, it is difficult to guarantee that this systematic error remains well below 0.4% of the Stark–PNC interference. This concern led us to consider the proposal by Bouchiat [34] to cancel birefringence effects by averaging PNC data at output-mirror positions that are separated by 90^o. This procedure has the advantage that it is easier to accurately perform a 90^o rotation than it is to accurately position the birefringence axes with respect to the z axis.

©1999 NRC Canada

Fig. 20. A schematic of the elements contributing to the systematic error due to the gradient in the y direction of the y component of the magnetic field for the $F = 3 \rightarrow F = 4$ hyperfine transition. The magnetic sublevels of the two hyperfine transitions are shown in (*a*). For the $F = 3 \rightarrow F = 4$ hyperfine transition, both the $\Delta m = +1$ and the detuned $\Delta m = -1$ transitions from the initial-state magnetic sublevel can contribute to the signal, while for the $F = 4 \rightarrow F = 3$ hyperfine transition, only one transition from the initial-state magnetic sublevel can contribute. The schematic in (*b*) shows how the y component of atomic velocity changes sign across the atomic beam, causing the sign of the Stark–$M1$ interference to change sign too. It also shows that the existence of a gradient, $\partial B_y/\partial y$, can cause the sign of B_y to differ across the atomic beam.

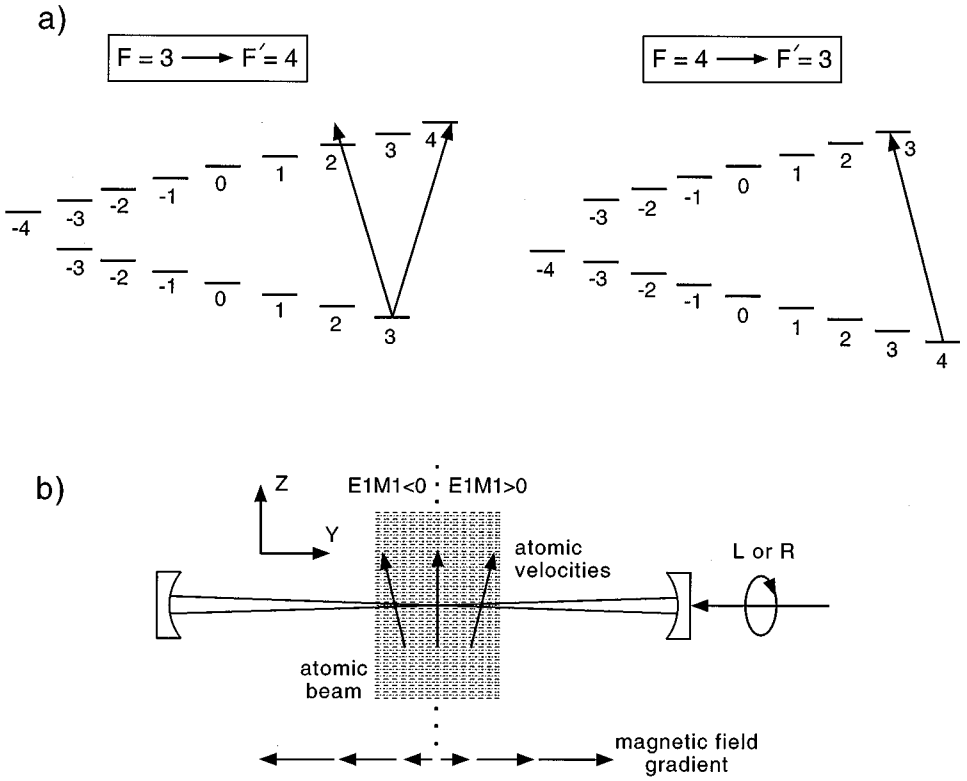

Thus, by averaging data for two output-mirror positions that are separated by 90°, we nearly eliminate this systematic error. With an uncertainty in the 90° rotation, $\delta\theta_2$, and variation in birefringence between the two output-mirror positions, $\delta\varphi_2$, we obtain the following ratio for this systematic error relative to the Stark–PNC interference term:

$$\frac{R_{\text{Stark}-M1}(\varphi_2, \theta_2)}{R_{\text{Stark}-\text{PNC}}} = \frac{M1}{2\text{Im}(E1_{\text{PNC}})} [\varphi_2\, \delta\theta_2 + \theta_2\, \delta\varphi_2] \tag{32}$$

To minimize the variation in birefringence between the two mirror positions, $\delta\varphi_2$, we first center the laser beam on the rotation stage that forms the front of the output mirror mount (shown in Fig. 8). This positioning is not crucial, however, since we have detected very little change in magnitude, and no change in direction, of the birefringence across our mirror surfaces.

To ensure that the ratio in (32) is less than 0.1% for our case of $\varphi_2 = 2.2 \times 10^{-6}$, we need $\delta\theta_2 < 2.6°$. This requirement is easily attained, for by using the decahexagon attached to the output-mirror rotation stage, (shown in Fig. 8), we can ensure that $\delta\theta_2 \simeq 0.5°$. Furthermore, since we always keep $\theta_2 < 5°$, this systematic error is less than 0.4% of the Stark–PNC interference at any individual mirror position.

©1999 NRC Canada

5.2.4. Systematic errors that differ for each hyperfine transition: Differential errors

There are several systematic errors that have a different magnitude for the two $\Delta F = \pm 1$ 6S–7S transitions; such errors are called "differential errors" and, if left unchecked, would lead to an incorrect measurement of the nuclear-spin-dependent PNC effects. These errors are the most difficult to control and arise from previously unknown effects.

$\partial(\Delta B_y)/\partial y$ systematic error The most troublesome potential systematic error arises from a gradient in the stray magnetic field in the y direction, $\partial(\Delta B_y)/\partial y$, for this gradient causes the Stark–$M1$ interference term to modulate with the p-reversal. This systematic error occurs only for the hyperfine transition 6S $F = 3 \rightarrow$ 7S $F = 4$ because we cannot completely resolve the transition of interest, $\Delta m = +1$, from the contaminating transition, $\Delta m = -1$, as shown in Fig. 20. Fortunately, however, the contaminating transition is much weaker than the transition of interest, both because it has a smaller Clebsch–Gordan coefficient ($[C_{33}^{42}]^2 = 2/64$ as compared with $[C_{33}^{44}]^2 = 56/64$), and because the laser is detuned from its resonant frequency. Note that for the other hyperfine transition, $F = 3 \rightarrow F = 4$, this contamination problem does not occur because, as shown in Fig. 20, only one transition can occur, $\Delta m = -1$.

The Stark–$M1$ interference varies across the beam as a result of the inhomogeneous, transverse-velocity distribution, which, in turn, causes an inhomogeneous Doppler shift. Specifically, atoms on one side of the beam have an average velocity component in the $+y$ direction while atoms on the other side of the beam have an average velocity component in the $-y$ direction, as shown schematically in Fig. 20. As a result, the Stark–$M1$ interference term is positive on one side of the beam and negative on the other [27]. This effect alone does not cause a systematic error, for the positive signal from one side of the atomic beam cancels the negative signal from the other. However, if there is a gradient in the y component of the stray magnetic field along the y direction, that is, $\partial(\Delta B_y)/\partial y$, then this small stray magnetic field can point in one direction on one side of the atomic beam and in the other direction on the other side of the atomic beam, also shown schematically in Fig. 20. This difference in magnetic-field direction will then cause the direction of the quantization axis for the dye-laser polarization to differ on either side of the atomic beam, which in turn will cause an increase in the strength of the $\Delta m = -1$ transition relative to that of $\Delta m = +1$ on one side of the atomic beam, and a decrease in this ratio on the other side. Thus, the signals from the two sides of the atomic beam will no longer cancel. When the handedness of the dye-laser polarization is reversed, so is the side of the atomic beam that has the increase in the relative strength. Thus, for one value of p there will be a net positive signal, while for the other value of p there will be a net negative signal, resulting in a small fractional modulation of the Stark–$M1$ interference term with dye-laser polarization, and thus a systematic error. Note that other magnetic-field gradients do not cause corresponding systematic errors, for although they cause the Stark–$M1$ interference term to modulate with p-reversal, they also induce a second modulation of this interference with b-reversal, resulting in no net modulation with b.

To eliminate this systematic error, we cancel out the gradient in the stray magnetic field by applying an opposing magnetic-field gradient using the smoothing coil. To measure the resulting net gradient, we excite the $\Delta F = 0$ transition and use the $\alpha\beta$ interference term (the second line in (C1)), which is sensitive to magnetic fields in the y direction. For our experimental conditions, this term results in the following fractional modulation $dPMA$ of the $\Delta F = 0$ transition rate

$$dPMA(\Delta F = 0) = 2\frac{\beta}{\alpha}\frac{\Delta B_y}{B_z}\frac{\epsilon_z}{\epsilon_I}C_{Fm}^{Fm} \simeq 0.15\frac{\Delta B_y}{B_z} \tag{33}$$

We find that a change of 1 mG/cm in the magnitude of the gradient causes a change in the fractional modulation $dEPMAB$ that is 5% of the Stark–PNC interference signal.

Therefore, to limit the contribution of this systematic error to less than 0.3% of the Stark–PNC interference modulation, we reduce the gradient in the stray magnetic field, $\partial(\Delta B_y)/\partial y$, to less than 60 μG/cm by blocking the atomic beam and then adjusting $\partial(\Delta B_y)/\partial y$ so that the fractional modulation

©1999 NRC Canada

$dPMA(\Delta F = 0)$ on one side of the atomic beam agrees with that on the other side of the beam to within 3 ppm.

We also monitor $\partial(\Delta B_y)/\partial y$ during our PNC data runs by taking advantage of the fact that this particular gradient also contributes to the fractional modulation $dEPB$:

$$dEPB \propto \frac{1}{E_x}\frac{1}{B_z}\frac{\partial(\Delta B_y)}{\partial y}\frac{\epsilon_I}{\epsilon_z} \tag{34}$$

via a Stark–$M1$ dilution mechanism. We find that a change of 1 mG/cm in the gradient causes a change of 2 ppm in the fractional modulation $dEPB$. Although the fractional modulation $dEPB$ has other significant contributions to it besides this gradient, and thus does not provide an accurate quantitative measurement of the gradient, it is useful nonetheless in catching any significant change that may occur during a run.

Systematic error due to power modulation synchronous with p-reversal We discovered another new potential systematic error that arises from the unusual line shape of the Stark–$M1$ interference. This systematic error occurs when the power inside the PBC modulates synchronously with the p-reversal, in turn causing the Stark–$M1$ line shape to modulate with the p-reversal, thus causing a contribution to the signal that mimics Stark–PNC interference.

Since this dye-laser-beam power-modulation systematic error is sensitive to the alignment of the probe-laser retro reflection used for the 6S $F = 4 \rightarrow$ 7S $F' = 3$ hyperfine transition, we categorize this error as a differential error. (Recall that the retro reflection is used to eliminate dark states during the detection process. Since the degree that a dark state is suppressed can differ for different velocity groups, retro reflection affects the efficiency with which a particular velocity group is detected.)

The line width for the 6S–7S $\Delta F = \pm 1$ transition is between 20 to 30 MHz and has many sources [33]: the natural width for the 7S state (3 MHz); the Doppler width for the atomic beam (16 MHz); and the inhomogeneous AC Stark broadening (which is typically 30 MHz though it depends on laser intensity). In addition, the line width is slightly affected by both the alignment of the probe laser beam and the degree of cesium atom spin polarization (since the sublevels are not resolved in the 6.4 G field).

The Stark–$M1$ interference term is also affected by these sources. For example, its line shape is quite sensitive to the degree of spin polarization, for even though there are only a few atoms that do not get pumped into the correct sublevel, these atoms tend to have huge Doppler shifts, and thus make a disproportionately large contribution to the Stark–$M1$ signal. Moreover, since the unpumped atoms are on one side of the peak, they cause the Stark–$M1$ line shape to be asymmetric.

In addition to being sensitive to the spin polarization, the Stark–$M1$ line shape is also sensitive to the laser intensity, for since we use such high laser power, which causes large AC Stark shifts, any change in laser intensity affects the width of the Stark–M1 line and thus its line shape. If this laser power modulation is synchronous with the p-reversal, then the Stark–M1 interference modulates with all five reversals and thus mimics the Stark–PNC interference.

To calibrate the effect of power modulation on the size of this systematic error, we intentionally apply a large power modulation synchronous with the p-reversal. We find that a change in the dye-laser intensity of 1% with p-reversal can give a modulation $dEPMAB$ that is 50% of the Stark–PNC interference. However, since this modulation depends on the alignment of the probe laser beam, we can use this alignment dependence to eliminate this systematic error. Since different atoms in the cesium beam have different transverse velocities, and thus different Doppler shifts, the measured modulation arises from the Stark–$M1$ interference term for a convolution of atoms with different Doppler shifts. Moreover, the narrow-band probe laser detects some velocity groups with greater efficiency than it does others, depending on its alignment. Thus the modulation that we measure depends on both the probe-laser power (through line broadening) and alignment.

To optimally align the probe laser beam, we first adjust its power to optimize the signal-to-background ratio. Then we apply a large modulation to the dye-laser power (3%) synchronous with the p-reversal,

©1999 NRC Canada

and adjust the probe-laser alignment to minimize the signal modulation. So that there is no modulation due to Stark–PNC interference, we do not modulate the handedness of the dye-laser polarization (that is, no p-reversal).

Under typical conditions, we find that a 1% modulation in the laser intensity synchronous with p-reversal causes a change in the fractional modulation $dEPMAB$ that is 15% of the Stark–PNC interference. Given a conservative value of 200 ppm for the fractional modulation of our laser intensity, this systematic error is 0.1% of the Stark–PNC interference. Note that even though this systematic error is sensitive to the alignment of the probe-laser retro reflection used for the 6S $F = 4 \rightarrow$ 7S $F' = 3$ hyperfine transition, with careful probe-laser alignment the two hyperfine lines of interest have comparable sensitivity to errors from power modulations that are synchronous with p-reversal.

To ensure that this systematic error is sufficiently low, we first determine the sources of polarization-dependent power modulation and reduce them. There are several sources of power modulation synchronous with p-reversal. For example, we have observed high-order, transverse, spatial modes of the PBC that are degenerate in frequency with the TEM_{00} Gaussian mode. Thus, there can be a transfer of energy between modes for light inside the PBC. If the Pockels cell alters the wave fronts for the two states of the p-reversal, then mode-matching into the PBC will depend on the p-reversal and so the power in the TEM_{00} mode will modulate. Similarly, power modulation can occur if the Pockels cell steers the dye-laser beam differently for the two states of p-reversal. We reduce these sources of synchronous power modulation to an acceptable level by carefully aligning the Pockels cell, properly adjusting the PBC mode-matching, and properly adjusting an intracavity aperture so that it greatly attenuates higher order transverse modes while having a negligible effect on the TEM_{00} mode.

Another source of p-reversal-dependent power modulation is polarization-dependent optical components located after the PBC. Such optical components cause the power incident on the intensity-stabilization photodiode to modulate with p-reversal, in turn causing the intensity servo to impose a power modulation on the light inside the PBC. A description of how we reduce the polarization dependence of these optical components to an acceptable level is given earlier in Sect. 3.3.7.

Similarly, light reflected from the PBC that is used for frequency locking must go through a series of optics before reaching the frequency-stabilization photodiode. If any of these optics have a polarization dependence, then the intensity of light striking this photodiode will depend on the incident polarization. This variation in incident intensity with polarization will, in turn, lead to a variation in the gain of the dye-laser/PBC servo loop with polarization, which is thus an error that is synchronous with p-reversal. To account for this systematic error, we first calibrate the effect by intentionally applying a large-intensity modulation (using a $\lambda/4$ plate and a polarizer) on the fast photodiode synchronous with the p-reversal. We then eliminate this systematic error by exclusively using near-normal-incidence reflections for the optical path leading to the frequency-stabilization photodiode. By measuring the intensity modulation of the light striking the fast photodiode, we verify that this error contributes less than 0.1% to the PNC modulation.

Elimination of the systematic error due to power modulation requires that we measure power modulations less than 100 ppm independent of the polarization state of the light. Since photodiodes have too much polarization sensitivity we developed an indirect method: we monitor the frequency shift of the 6S–7S transition induced by an intensity-dependent, polarization-independent, AC Stark shift [36].

The effect of power modulation on the $\Delta F = 0$ line can be seen in Fig. 21, where we have intentionally modulated the laser intensity, I, by $\pm 9\%$. These traces were taken with an average laser intensity that is half that used in the PNC experiments. If we increase the average intensity, the widths continue to increase due to the AC Stark shift, while the peaks remain nearly constant since the transition is near saturation. Note that the line shift is predominantly in one direction, as seen by the difference between the two traces, given by the broken line. Indeed, the change in transition rate with intensity for a fixed laser frequency is five times larger on one side of the line than on the other.

To cancel out any sensitivity of the transition rate to dye-laser polarization, we perform a differential

©1999 NRC Canada

Fig. 21. Plot of the line shape for the $\Delta F = 0$ transition for two dye-laser intensities, I, differing by 18%. Note how on one side of the peak, the signal intensity α at a specific frequency changes by a larger fraction than it does for a specific frequency on the other side of the peak. A plot of the difference between these two signals (broken line) clearly shows the asymmetry in the line shift. (Note that here we use the notation α to represent signal intensity so as not to confuse it with the laser intensity, I).

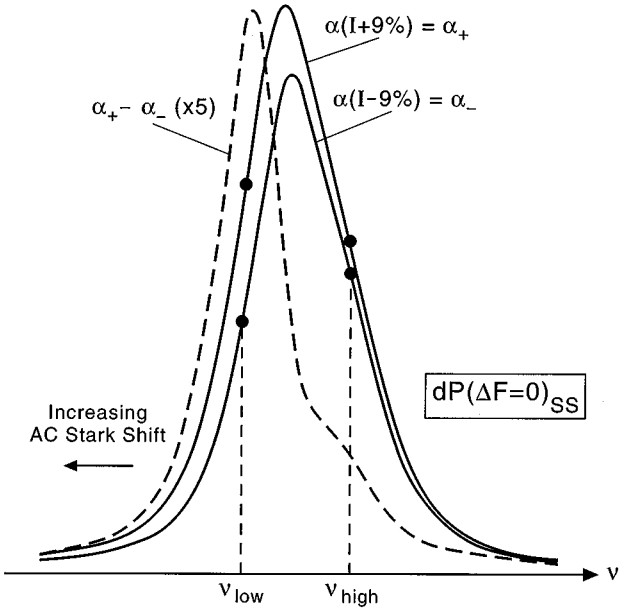

measurement between the two sides of the line. First we set the dye-laser frequency to match the frequency for which the transition strength is least affected by changes in laser intensity, ν_{high}, and measure the modulation in transition rate as the polarization is reversed. Then we reset the dye-laser frequency to match the frequency for which the transition strength is most affected by changes in laser intensity, ν_{low}, and again measure the modulation in transition rate with polarization. The difference between the two modulations gives a modulation that is due only to intensity changes and not to polarization changes. To obtain the cleanest signals we perform this calibration on $\Delta F = 0$ lines and with an atomic beam that is not spin polarized.

Under normal operating conditions (power density = 800 kW/cm^2) the fractional modulation of the transition rate with p-reversal, $dP(\Delta F = 0)_{\text{SS}}$, where SS stands for side-to-side, is related to the fractional change in laser intensity by:

$$\frac{dP(\Delta F = 0)_{\text{ss}}}{\Delta I/I} \simeq 3 \tag{35}$$

Thus, a change in power of 100 ppm that is synchronous with the p-reversal leads to a fractional modulation $dP(\Delta F = 0)_{\text{ss}}$ of 300 ppm.

Using this technique we can monitor the polarization-dependent power modulation and adjust the dye laser and PBC alignment to minimize it. For PNC runs this modulation was between 18 and 50 ppm. In combination with the proper probe alignment discussed above, this results in a negligible systematic error.

©1999 NRC Canada

Systematic error due to imperfect laser polarization Ideally, we want pure, reversing, elliptical light inside the PBC during the PNC measurement, that is, we want $\boldsymbol{\epsilon} = \epsilon_z\hat{z} \pm i\epsilon_I\hat{x}$, where the $\pm$ refers to p-reversal. We have discovered that if the x component of the dye-laser polarization has a real, nonreversing part, ϵ_{R}, (defined as being in phase with the z component of polarization, ϵ_z), then a contribution to the signal arises that mimics the Stark–PNC interference. In this case, the dye-laser polarization is given by $\boldsymbol{\epsilon} = \epsilon_z\hat{z} + (\epsilon_{\mathrm{R}} + ip\epsilon_I)\hat{x}$.

Although we do not have a definitive physical explanation for this systematic error, we have empirically determined that it gives a fractional signal, S, that mimics the PNC modulation,

$$S = 38(7)\,ppm\,\frac{\epsilon_{\mathrm{R}}}{\epsilon_z}\left(\frac{600}{E}\right)^2 \tag{36}$$

Thus, a value of $\epsilon_{\mathrm{R}}/\epsilon_z = 0.1$, at $E = 600$ V/cm, leads to a fractional modulation that is 6% of the Stark–PNC interference. We can equivalently write this as

$$S = \beta^2[22.8(4.2)\times 10^3]\frac{\epsilon_{\mathrm{R}}\epsilon_z}{(\beta^2E^2\epsilon_z^2)} \tag{37}$$

which shows explicitly that the $1/E^2$ dependence arises solely because we are looking at a fractional change in the pure Stark-induced transition rate, for if this effect were due to a transition amplitude interfering with the $E1_{\mathrm{Stark}}$ amplitude, then we would see either a $1/E$ scaling or no E-dependence at all. Thus, we suspect that this systematic error comes from an AC Stark shift and is entirely light induced.

We adjust the polarization so that $\epsilon_{\mathrm{R}}/\epsilon_z$ is sufficiently small to ensure that no significant errors are introduced. Typically, $\epsilon_{\mathrm{R}}/\epsilon_z \simeq 0.003$ and its absolute value is always < 0.006. This ensures that the contribution to the PNC signal is always less than the 4% statistical error for each 2 h data block.

For circularly polarized light, we control $\epsilon_{\mathrm{R}}/\epsilon_z$ by adjusting the voltage on the Pockels cell, while for elliptically polarized light we control it by rotating the half-wave plate located just before the PBC. We adjust the polarization after each 2 h block, making sure that over the course of many blocks, the average value for $\epsilon_{\mathrm{R}}/\epsilon_z$ is nearly zero. This method essentially eliminates the sensitivity to uncertainty in the calibration shown in (37).

In addition to the many measurements discussed above, we also carried out a very extensive set of measurements in which we applied all the various possible reversing and nonreversing field components (and many of their gradients) individually and in combination, and studied their effects on the various modulation signals we could monitor. We also applied various polarization components of the dye-laser light. Where relevant we have mentioned the results of particular measurements in the above discussion, but we do not take the space here to separately discuss the entire set of many such measurements. Although in some sense most of these measurements were redundant with our other analysis, they did accomplish several purposes:

- they experimentally confirmed the sizes and dependencies of the various calculated potential PNC systematic errors listed above;
- they confirmed (and in a few cases, revealed) how all the various fields showed up as contributions in the many different modulation patterns; and
- they tested for and ruled out the existence of possible PNC systematic errors that depended on many different fields, field gradients, and polarizations.

5.3. Calibration corrections

Here we describe calibration corrections and associated uncertainties involved in extracting a value for the observable $\mathrm{Im}(E1_{\mathrm{PNC}})/\beta$ from the measured signal.

©1999 NRC Canada

Fig. 22. Scan over the 6S–7S transition at zero magnetic field. The detuning factors, d_i, indicate the relative contributions of detuned transitions to the total signal intensity.

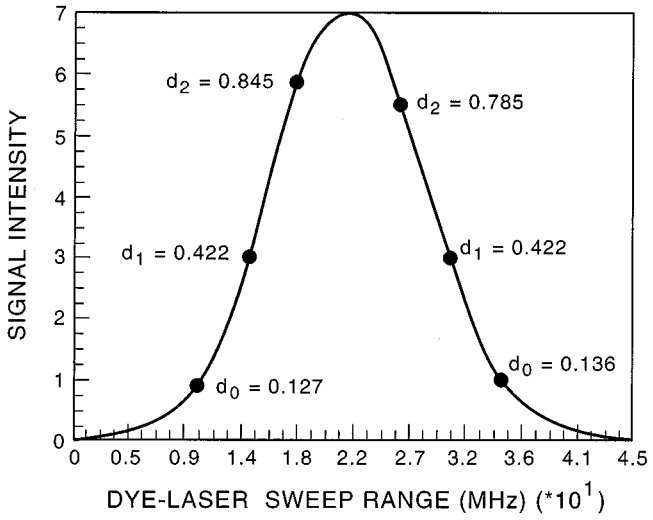

5.3.1. Deconvolution of transitions contributing to one spectral line: Dilution

We measure the fractional modulation in signal that is synchronous with a modulation in the handedness of the coordinate system. If our signal is due only to one transition between two magnetic sublevels, then the fractional modulation due to the Stark–PNC interference term is given by (10). However, if we have either incomplete optical pumping (so that the neighboring initial-state sublevel has some population) or incomplete resolution of transition lines (so that we detect both $\Delta m = +1$ and $\Delta m = -1$ transitions for the $F = 3 \rightarrow F = 4$ hyperfine transition) our signal will be due to two or more transitions. Taking these transitions into account, the relation between our measured fractional modulation $dEPMAB$ and the observable $\mathrm{Im}(E1_{\mathrm{PNC}})/\beta$, is given by

$$dEPMAB = 2\frac{\mathrm{Im}(E1_{\mathrm{PNC}})}{\beta E_x}\frac{\epsilon_I}{\epsilon_z}\frac{\sum_m \pm f_m d_i \left(C_{Fm}^{F'm\pm1}\right)^2}{\sum_m f_m d_i \left(C_{Fm}^{F'm\pm1}\right)^2} \simeq 2\frac{\mathrm{Im}(E1_{\mathrm{PNC}})}{\beta E_x}\frac{\epsilon_I}{\epsilon_z}\left(1-\frac{d_2}{14}\right) \tag{38}$$

where f_m is the fractional population in the magnetic sublevel m of the initial cesium hyperfine state; d_i is a "detuning factor" that represents the contribution to the signal from transitions other than the resonant transition, as described below; and the sum is over contributions from all possible transitions. Our measurement of fractional populations, f_m, is discussed in Appendix A. Since only the initial-state sublevel and the neighboring sublevel have appreciable population, we truncate this sum to two terms; in the second term, the $d_2 f_3$ term, we set $f_3 = 1$. We call the factor $(1-d_2/14)$ the "dilution correction." This equation differs from (10) in that it has a dilution, $d_2/14$, which represents the amount by which the signal is diluted by the presence of multiple transitions.

Note in Fig. 20 that for the transition 6S $F = 3 \rightarrow$ 7S $F' = 4$, two transitions from the $m = 3$ sublevel can occur, $\Delta m = \pm 1$. Thus, for this hyperfine transition we must extract from the measured modulation the contribution from each transition to different upper-state magnetic sublevels. In contrast, for the other hyperfine transition, 6S $F = 4 \rightarrow$ 7S $F' = 3$, there is only one sublevel transition possible; thus, there is no dilution correction needed.

©1999 NRC Canada

Fig. 23. Plot of the signal intensity for the $\Delta F = 0$ transition as a function of DC electric field, showing saturation of the transition. The triangles represent our data, the broken line is a fit to our data of a functional form for the transition rate assuming no saturation, and the continuous line is a fit to our data of a functional form for the transition rate assuming saturation.

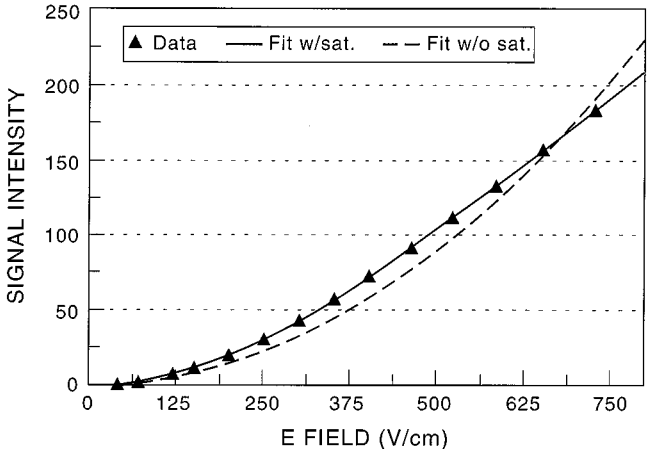

The detuning factor d_i represents the relative contribution of a detuned transition to the resonant transition; a series of d_i is shown in Fig. 22. For an initial 6S $F = 3$ $m = 3$ state, with the laser tuned to excited the 7S $F = 4$ $m = 4$ sublevel, d_3 (not shown) represents the resonant transition and is equal to 1, d_2 represents the relative contribution of the $\Delta m = -1$ transition (which is detuned by 4.5 MHz), d_1 represents the relative contribution of a transition that is detuned by 9 MHz, and so on. Because of the line-shape asymmetry seen in Fig. 22, detuning factors (d_i) on opposite sides of the line differ. Since we take data for transitions at opposite ends of the multiplet, and since the line shape for each $m-$to$-m'$ transition remains the same across the multiplet, we take an average of the two d_i's on each side of a line.

Our measurement of the detuning factors d_i is a refined, digital version of the technique used in our 1988 experiment. We calibrate both the magnetic field in the interaction region and the dye-laser frequency scale over the range of the transition. To obtain the line shape for each individual Δm transition, we scan over the transition with no magnetic field. From this line shape and the shifts of the transitions due to the known applied magnetic field, we find the fractional contribution of each detuned transition to the peak intensity of the line. These fractional contributions are the detuning factors, d_i, shown in Fig. 22.

The $d_2 f_3$ term is sensitive to fluctuations in the laser intensity because such fluctuations cause changes in the line shape (because of broadening by AC Stark shifts). In contrast, this term is insensitive to the spin polarization (f_2 and f_3); indeed, changing f_3 from 0.9 to 1.0 affects the term by only a few tenths of a percent. This insensitivity to laser polarization arises because the $d_2 f_3$term is dominated by the $\Delta m = -1$ transition for which the Clebsch–Gordan coefficient is small.

From the above analysis, we find that the dilution factor for the PNC data ranges between 0.940(1) and 0.942(1) for the $3 \rightarrow 4$ transition, and is 1.00 with negligible uncertainty for the $4 \rightarrow 3$ transition. The observed signal is divided by this factor, (38).

©1999 NRC Canada

5.3.2. Correction for saturation of the transition

If we excite too large a fraction of the cesium atoms there will be saturation. Our observed modulation signal will be smaller than the signal as given by (10) and will thus need to be corrected. In this section we describe our measurement of the extent of saturation, and our correction for this saturation.

To measure the extent of saturation, we study the $\Delta F = 0$ transition, since this transition rate is larger and we know how to scale to the weaker $\Delta F \pm 1$ transition. A plot of fluorescence signal intensity as a function of electric-field strength for this transition is shown in Fig. 23, where the triangles represent our data. The dotted line shows a fit to our data of the functional form $I \propto \alpha^2 E^2 \epsilon_z^2$, which neglects saturation of the transition, while the continuous line shows a fit to our data of the functional form

$$I = k \frac{E^2}{1 + \left(\frac{E}{E_{\rm sat}}\right)^2} \tag{39}$$

which takes into account the effect of saturation. Clearly the latter curve fits our data better, giving a saturation field $E_{\rm sat}$ of 1040 V/cm.

To correct for the effect of saturation on our PNC modulation, we use the measured scaling factor $\alpha/\beta = 9.905$ [32] to calculate the saturation electric field for the $\Delta F = \pm 1$ transitions. This scaling gives $E_{\rm sat} = 10\,300$ V/cm for these transitions.

The saturation correction at $E = 500$ V/cm is then $1 + \left(\frac{E}{E_{sat}}\right)^2 \simeq 1 + \left(\frac{500}{10\,300}\right)^2 \simeq 1.0024(3)$. The uncertainty is from both the statistical uncertainty of the measurement in Fig. 23 and the residuals from the fit. This correction multiplies the observed signal.

5.3.3. Measurement of the dye-laser polarization

We take PNC data at two different dye-laser polarizations, $\epsilon_I/\epsilon_z = 1$ and $\epsilon_I/\epsilon_z = 2$, and these polarization ratios must be precisely measured. Our measurement of this polarization ratio to 1 part in 1000 is the same as that in ref. 32; a description is given in Appendix B. Here we discuss the related problem of how we determine the orientation of the axis of the polarimeter to sufficient accuracy relative to the axis of the PNC interaction region.

We use the fact that the Pockels cell generates transients in the laser field strength (polarization transients) along any direction except its birefringence axes when its voltage is reversed. Thus, we know that the axes of the Pockels cell are parallel to the electric-field plates when we see no transients on the 6S–7S transition rate when the Pockels cell voltage is flipped. To ensure that the axes of the polarimeter (located after the PBC) are matched to the experimental coordinate system, we align the initial angle of the polarimeter input polarizer so that there are no transients in the light it transmits. With this technique we can align all the axes to better than $0.5^{\rm o}$. We did various tests rotating the output mirror and output window to make sure that birefringence of these optical elements did not affect our polarization measurements at the level of interest. From this work, we conclude that our polarization measurements have an uncertainty of about 0.1%, which is predominantly statistical [32]. This gives an overall uncertainty in the PNC measurement due to uncertainty in the ratio ϵ_I/ϵ_z that is less than 0.05%.

5.3.4. Subtraction of the background

There are three sources of background signal that occur with no applied electric field: the pure magnetic dipole ($M1$) 6S–7S transition rate, scattered light, and imperfect optical pumping. These must be measured and subtracted from the observed signal to properly determine the fractional PNC modulation. The $M1$ contribution depends on dye-laser frequency and hence must be measured at the frequency of the normal Stark-induced 6S–7S transition. (This is shifted by about 5 MHz from the peak of the

©1999 NRC Canada

Fig. 24. Sixteen individual PNC measurements taken for one data block. Im($E1_{PNC}$)/β is the fractional modulation in the 6S $\rightarrow$ 7S excitation rate with the dependence on static and oscillating electric fields, $\boldsymbol{E}$ and $\boldsymbol{\epsilon}$, divided out. This leaves the results in terms of an equivalent electric field that would provide the same mixing of S and P states as the parity-violating interaction.

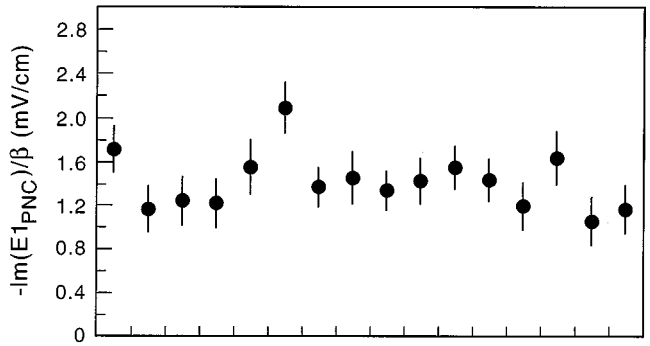

pure $M1$ transition.) The imperfect optical pumping background changes slightly with the a, b, and m reversals, and hence we must measure it under all possible field configurations.

During the PNC runs we regularly (about every 2 h) short out the electric-field plates to null the electric field and measure this background. We then subtract this background from the total transition intensity to obtain the pure Stark-induced transition signal, which is then used to calculate the fractional modulations.

5.3.5. Calibration of the electric field

To determine the strength of the electric field, we measure both the voltage across the plates (with a Fluke 8505A digital voltmeter) and the spacing between the plates. To measure the spacing, we place the assembly on a polished granite surface, measure the distance from the granite surface to the surface of the bottom plate using a dial indicator, and then measure the height of the dial indicator with a precision height micrometer that has zero backlash. We then repeat the process for the corresponding point on the top plate, and take the difference. By doing this for many pairs of points, we obtain a map of the plate surface. We find that the variations in the plate spacing are less than 0.0003 cm, and calculate an average spacing of 98 577(25) cm. The uncertainty in this spacing is a combination of the statistical variations obtained by several measurements that were made by three different individuals and the accuracy specifications given for the height gauge. The electric field is then taken to be the voltage divided by the plate spacing.

6. Statistical tests

We check our results by performing extensive statistical tests that examine whether there are any variations in the results that cannot be explained by shot noise alone.

We acquired 177 blocks of data, as described in Sect. 4.1. Results for a single block of data (which consists of 16 measurements and takes about 1.5 h to acquire) are shown in Fig. 24. Each of these 16 individual measurements consists of 16 384 e-reversals (at 27 Hz), 256 a-reversals (at 0.29 Hz), 64 p-reversals (at 0.07 Hz), 16 b-reversals (at 0.018 Hz), and 4 m-reversals (at 0.004 Hz). In total, 106 data blocks were acquired for the 4 $\rightarrow$ 3 transition, and 71 for the 3 $\rightarrow$ 4 transition.

Figure 25 shows all the data blocks for each of the two hyperfine transitions. Note that the noise is about 25% larger for the $F = 4 \rightarrow 3$ transition than for the $F = 3 \rightarrow 4$ transition. This difference is

©1999 NRC Canada

Table 1. The values of PNC data grouped by polarization ratio and hyperfine transition, and the values of χ^2 when polarizations are combined.

	$\epsilon_1/\epsilon_z = 1$	$\epsilon_1/\epsilon_z = 2$	Combined χ^2
6S $F = 4 \rightarrow$ 7S $F = 3$	1.630(9)	1.623(17)	1.092; Probability = 25%
6S $F = 3 \rightarrow$ 7S $F = 4$	1.548(8)	1.571(14)	0.876; Probability = 76%

Fig. 25. Scatter plots of all the PNC measurements obtained under different conditions, including those used to obtain our final results.

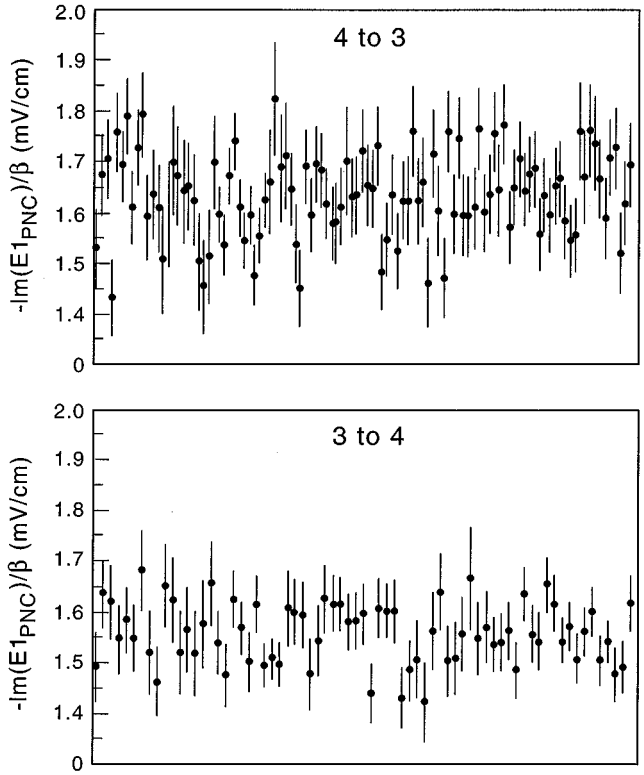

mainly due to the additional sensitivity to diode-laser noise through the imperfect suppression of dark states for the $F = 4 \rightarrow 3$ transition when detection is performed via the cycling transition from the 6S $F_{\rm det} = 3$ state to the $6P_{3/2}$ $F' = 2$ state. There is also detection of slightly fewer atoms on the $F = 4 \rightarrow 3$ transition.

To test whether our results are shot-noise limited, we first compare the noise on one block of PNC data, such as that shown in Fig. 24, with the noise observed on the shortest of time scales, that is, on the fluorescence signal as measured with a fast Fourier transform (FFT) spectrum analyzer. We find good agreement, which indicates that the fluctuations in the PNC values are predominantly due to shot noise. The agreement also indicates that there are no systematic drifts in the PNC values on a time-scale of 2 h.

We then compare the differences in the results obtained for each two-hour data block shown in Fig. 25 with the statistical fluctuations within each block (taken to be the short-term noise) by calculating the reduced χ^2. As shown in Table 1, the probability for the observed value of χ^2 is 25% for the $4 \rightarrow 3$

©1999 NRC Canada

Fig. 26. Histograms showing the distribution of PNC data blocks for each hyperfine transition. Solid bars represent our data, while open bars are the theoretical distributions predicted for random samples with standard deviations equal to the short-term noise on the fluorescence signals, which is predominantly shot noise. The difference in the central values for the two transitions is due to the nuclear anapole moment.

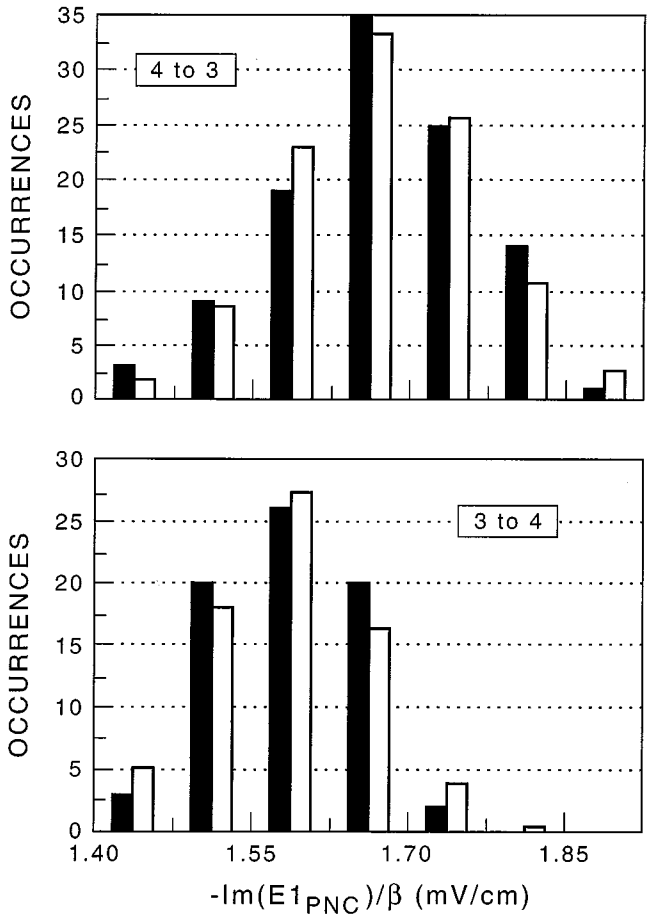

transition and 75% for the $3 \rightarrow 4$ transition. These values are consistent with statistical variations in the PNC values, as shown in Fig. 26, where our data (solid bars) are compared to a Gaussian distribution (open bars) that has the same average value and a standard deviation based on the short-term noise.

We also perform χ^2 tests on sets of data blocks grouped according to either run number, electric-field value (which we vary between 400 and 950 V/cm for different data runs), or dye-laser polarization ratio. The results of all three tests show that there is no statistically significant difference between PNC data obtained under these different conditions. In particular, the results for the test of dye-laser polarization are shown in Table 1. This test is particularly relevant because, as discussed earlier, if there were an error arising from the Stark–$M1$ interference, it would show up as a difference in the measured PNC values taken at $\epsilon_I/\epsilon_z = 1$ and 2. The absence of a statistical difference between the PNC values taken at different dye-laser polarization ratios rules out all Stark–$M1$ interference terms as a source of significant systematic error.

©1999 NRC Canada

Table 2. Comparison of experimental parameters for the present work with those for our previous measurement. Note that we have improved the PNC signal-to-noise ratio by nearly a factor of 7.

Quantity	**1988**	**1996**
540 nm laser power density	200 kW/cm^2	800 kW/cm^2
Detection efficiency	25%	≈65%
Cavity waist, ω_o	0.21 mm	0.41 mm
Volume = $\pi\omega_o^2 L$, $L = 2$ cm	0.0028 cm^3	0.011 cm^3
Resonant atomic density	1 x 10^8 cm^{-3}	2.2 x 10^8 cm^{-3}
Experimental duty factor	$< 30\%$	$\approx 65\%$
$\Delta F = +1$ 6S–7S photocurrent	200 pA	200 nA
Signal/background	17	4
Electric field	1000 V/cm	450–950 V/cm
Magnetic field	74 G	6.4 G
6S–7S shot noise	28.5 ppm/$\sqrt{\text{Hz}}$	15 ppm/$\sqrt{\text{Hz}}$
6S–7S technical noise	22 ppm/$\sqrt{\text{Hz}}$	<8 ppm/$\sqrt{\text{Hz}}$
BG, detector noise	27 ppm/$\sqrt{\text{Hz}}$	<8 ppm/$\sqrt{\text{Hz}}$
Fractional PNC modulation	3.2 ppm	6–8 ppm
PNC signal/noise	0.07/$\sqrt{\text{Hz}}$	0.45/$\sqrt{\text{Hz}}$

7. Results and conclusion

After taking into account the appropriate calibrations and corrections as described in the previous two sections, we obtain the results shown in Fig. 26 for our measurement of parity nonconservation on the $\Delta F = \pm 1$ transitions between the 6S and 7S states of cesium. From this data, our final results are

$$\frac{\text{Im}(E1_{\text{PNC}})}{\beta} = \begin{array}{ll} -1.5576(77) & \text{mV/cm} \qquad 6S\ F = 3 \rightarrow 7S\ F' = 4 \\ -1.6349(80) & \text{mV/cm} \qquad 6S\ F = 4 \rightarrow 7S\ F' = 3 \end{array} \tag{40}$$

Physically, the quantity $\text{Im}(E1_{\text{PNC}})/\beta$, which is 1.6 mV/cm for the system studied here, represents the magnitude of an applied electric field that would produce a pure Stark-induced transition amplitude equal to the pure PNC transition amplitude. The uncertainties are dominated by the statistical uncertainties of 0.0078 and 0.0073 mV/cm, respectively.

The difference between these two results, due to the nuclear-spin-dependent contribution, is 0.077(11) mV/cm. This is related to the nuclear anapole moment and provides information about parity violating purely hadronic interactions. The appropriately weighted average,

$$\begin{aligned} \frac{\text{Im}(E1_{\text{PNC}})}{\beta\xi}\left(\frac{-Q_W}{N}\right) &= (0.535)\ \delta_{LR}(4,3) + (0.465)\ \delta_{LR}(3,4) \\ &= -1.5935(56)\ \ \text{mV/cm} \end{aligned} \tag{41}$$

where the weighting factors are the average of those derived in refs. 37–39, gives a nuclear-spin-independent result of $-1.5963(56)$ mV/cm.

Comparison of these results to those of our previous measurement [2] ($\text{Im}(E1_{\text{PNC}})/\beta = -1.693(47)$ and $-1.513(49)$ mV/cm for the $4 \rightarrow 3$ and $3 \rightarrow 4$ transition, respectively) shows that our new results not only agree with the old but are more precise by a factor of 6.5. A comparison of the parameters for the 1998 and 1996 measurements is summarized in Table 2.

From the nuclear-spin-independent average for $\text{Im}(E1_{\text{PNC}})/\beta$, one can extract a value for the weak charge of the nucleus, Q_w, which provides a test of the standard model of electroweak unifi-

©1999 NRC Canada

cation [8,9,40]. This requires both a knowledge of the atomic structure, which can be obtained by ab initio calculations [37,41–44]and a value for β, which can be obtained from related atomic structure calculations or by experimental measurements [45]. In ref. 45, a value for the weak charge is extracted following this procedure, and is compared with the standard model value. The uncertainties arising from this procedure are discussed extensively.

The difference in the PNC on the two hyperfine lines constitutes the first measurement of an anapole moment, in this case that of the nucleus. This arises from parity nonconservation in the nuclear ground state due to PNC hadronic interactions. As discussed in refs. 46,47 this provides valuable new information about PNC in purely hadronic interactions, particularly the sizes of the pi and rho meson PNC coupling constants.

This paper has provided a detailed discussion of the experimental measurement of parity nonconservation in atomic cesium. This is the most precise measurement of PNC in an atomic system to date. It provides the first measurement of a nuclear-spin-dependent contribution to atomic PNC, and makes possible a precise low-energy test of the standard model. The many elements of the highly complex apparatus have been presented for the first time, as have been the extensive analysis of potential systematic errors.

Acknowledgments

We would like to acknowledge the extensive help of B. Masterson and C. Tanner in the development of the apparatus, and the major assistance of L. Kovalenko in the writing of this manuscript. Countless members of the AMO community have provided useful advice and suggestions over the course of this experiment. The work was funded by the NSF. JLR acknowledges support of an NSF predoctoral fellowship.

References

1. M.A. Bouchiat and C. Bouchiat. J. Phys. (Paris), **35**, 899 (1974).
2. M.C. Noecker, B.P. Masterson, and C.E. Wieman. Phys. Rev. Lett. **61**, 310 (1988).
3. D.M. Meekhof et al. Phys. Rev. Lett. **71**, 3442 (1993).
4. N.H. Edwards et al. Phys. Rev. Lett. **74**, 2654 (1995).
5. P.A. Vetter et al. Phys. Rev. Lett. **74**, 2658 (1995).
6. M.J.D. Macpherson et al. Phys. Rev. Lett. **67**, 2784 (1991).
7. R.B. Warrington, C.D. Thompson, and D.N. Stacey. Europhys. Lett. **24**, 641 (1993).
8. W.J. Marciano and A. Sirlin. Phys. Rev. D: Part. Fields, **29**, 75 (1984).
9. W.J. Marciano and J.L. Rosner. Phys. Rev. Lett. **65**, 2963 (1990).
10. Ya.B. Zel'Dovich. JETP, **6**, 1184 (1958).
11. V.V. Flambaum and I.B. Khriplovich. JETP, **52**, 835 (1980).
12. C. Bouchiat and C.A. Piketty. Z. Phys. C: Part. Fields, **49**, 91 (1991).
13. V.F. Dmitriev, I.B. Khriplovich, and V.B. Telitsin. Nucl. Phys. **A577**, 691 (1994).
14. M.A. Bouchiat et al. Phys. Lett. **117B**, 358 (1982).
15. M.A. Bouchiat et al. Phys. Lett. **134B**, 463 (1984).
16. M.A. Bouchiat et al. J. Phys. (Paris), **47**, 1709 (1986).
17. S.L. Gilbert and C.E. Wieman. Phys. Rev. A: Gen. Phys. **34**, 792 (1986).
18. G. Avila et al. Phys. Rev. A: Gen. Phys. **36**, 3719 (1987).
19. R.N. Watts and C.E. Wieman. Opt. Commun. **57**, 45 (1986).
20. B.P. Masterson, C. Tanner, H. Patrick, and C.E. Wieman. Phys. Rev. A: At. Mol. Opt. Phys. **47**, 2139 (1993).
21. M.A. Bouchiat and C. Bouchiat. J. Phys. (Paris), **36**, 493 (1975).
22. V.V. Flambaum, I.B. Khriplovich, and O.P. Sushkov. Phys. Lett. **67A**, 177 (1978).
23. C.E. Wieman and L. Hollberg. Rev. Sci. Instrum. **62**, 1 (1991).
24. K.B. MacAdam, A. Steinbach, and C.E. Wieman. Am. J. Phys. **60**, 1098 (1992) and references therein.
25. N.M. Sampas. Ph.D. thesis, JILA, University of Colorado at Boulder. 1990.

©1999 NRC Canada

26. R.W.P. Drever, J.L. Hall, F.V. Kowalski, J. Hough, G.M. Ford, A.J. Munley, and H. Ward. Appl. Phys. B, **31**, 97 (1983).
27. M.C. Noecker. Ph.D. thesis, JILA, University of Colorado at Boulder. 1988.
28. R.G. Brewer and E.L. Hahn. Phys. Rev. A: Gen. Phys. **11**, 1641 (1975) and references therein; P.M. Radmore and P.L. Knight. J. Phys. B: At. Mol. Opt. Phys. **15**, 561 (1982) and references therein; A. Aspect et al. J. Opt. Soc. Am. B, **6**, 2112 (1989).
29. J. Dalibard and C. Cohen-Tannoudji. J. Opt. Soc. Am. B, **6**, 2023, (1989).
30. BiotSavart magnetic field calculator. Vol. 2.1. [Computer software], Merritt Reynolds Kaliden, B.C. 1993.
31. P.S. Drell and E.D. Commins. Phys. Rev. A: Gen. Phys. **32**, 2196 (1985).
32. D. Cho, C.S. Wood, S.C. Bennett, J.L. Roberts, and C.E. Wieman. Phys. Rev. A: At. Mol. Opt. Phys. **55**, 1007 (1997).
33. B.P. Masterson. Ph.D. thesis, JILA, University of Colorado at Boulder. 1991.
34. M.A. Bouchiat, A. Coblentz, J. Guena, and L. Pottier. J. Phys. (Paris), **42**, 985 (1981).
35. S.L. Gilbert. Ph.D. thesis, University of Michigan. 1984.
36. C.E. Wieman, M.C. Noecker, B.P. Masterson, and J. Cooper. Phys. Rev. Lett. **58**, 1738 (1987).
37. S.A. Blundell, J. Sapirstein, and W.R. Johnson. Phys. Rev. D: Part. Fields, **45**, 1602 (1992).
38. A.Ya. Kraftmakher. Phys. Lett. **132A**, 167 (1988).
39. P.A. Frantsusov and I.B. Khriplovich. Z. Phys. D: At. Mol. Clusters, **7**, 297 (1988).
40. K.T. Mahanthapa and P.K. Mohapatra. Phys. Rev. D: Part. Fields, **43**, 3093 (1991).
41. V.A. Dzuba, V.V. Flambaum, and O.P. Sushkov. Phys. Lett. **141A**, 147 (1989).
42. V.A. Dzuba, V.V. Flambaum, and O.P. Sushkov. Phys. Lett. **140A**, 493 (1989);**142A**, 373 (1989).
43. V.A. Dzuba, V.V. Flambaum, and O.P. Sushkov. Phys. Rev. A: At. Mol. Opt. Phys. **56**, R4357 (1997).
44. S.A. Blundell, W.R. Johnson, and J. Sapirstein. Phys. Rev. Lett. **65**, 1411 (1990); Phys. Rev. A, **42**, 3751 (1990); **43**, 3407 (1991).
45. S.C. Bennett and C.E. Wieman. Phys. Rev. Lett. **82**, 2484 (1999).
46. W.C. Haxton. Science, **275**, 1753 (1997).
47. V.V. Flambaum and D.W. Murray. Phys. Rev. C: Nucl. Phys. **56**, 1641 (1997).
48. N.F. Ramsey. Molecular beams. Clarendon Press, Oxford. 1956.
49. M. Kasevich, D.S. Weiss, E. Riis, K. Moler, S. Kasapi, and S. Chu. Phys. Rev. Lett. **66**, 2297 (1991).
50. M. Kasevich and S. Chu. Appl. Phys. B, **54**, 321 (1992).
51. K. Moler, D.S. Weiss, M. Kasevich, and S. Chu. Phys. Rev. A, **45**, 342 (1992).
52. A. Yariv. IEEE J. Quantum. Electron. **QE-13**, 943 (1977).
53. K.T. Lau, N. Bar-Chaim, I. Urym, and A. Yariv. Appl. Phys. Lett. **43**, 1 (1983).
54. P.R. Hemmer, M.S. Shahriar, H. Lamela-Rivera, S.P. Smith, B.E. Bernacki, and S. Ezekiel. J. Opt. Soc. Am. B, **10**, 1326 (1993).
55. C.J. Myatt, N.R. Newbury, and C.E. Wieman. Opt. Lett. **18**, 649 (1993).
56. P. Feng and T. Walker. Am. J. Phys. **63**, 905 (1995).
57. H.R. Noh, J.O. Kim, D.S. Nam, and W. Jhe. Rev. Sci. Instrum. **67**, 1431 (1996).
58. D.E. Aspnes and A.A. Studna. Appl. Opt. **14**, 220 (1975).
59. R.W. Collins. Rev. Sci. Instrum. **61**, 2029 (1990).
60. E. Hecht. Optics. Addison-Wesley, Reading, Mass. 1987.
61. E. Collett. Polarized light. Marcel Dekker, Inc., New York. 1993.
62. R.M.A. Azzam and N.M. Bashara. Ellipsometry and polarized light. North-Holland Publishing Co., Amsterdam. 1977.
63. P.S. Hauge and F.H. Dill. Opt. Commun. **14**, 431 (1975)

Appendix A. Determination of initial population distribution by Raman spectroscopy

A.1. Overview

The fractional modulation in the signal intensity given in (10) assumes 100% population in the initial-state sublevel of interest. Since we typically prepare an initial atomic beam with 96% of the atoms in the sublevel of interest, we must correct our signal for contamination by atoms in other sublevels. Therefore, we must measure the populations in these other sublevels.

©1999 NRC Canada

Fig. 27. Relevant energy levels of cesium for a two-photon Raman transition between the 6S $F = 3, m = 3$ state and the 6S $F = 4, m = 3$ state. The detuning from the $6P_{3/2}$ $F = 2$ state is 160 MHz.

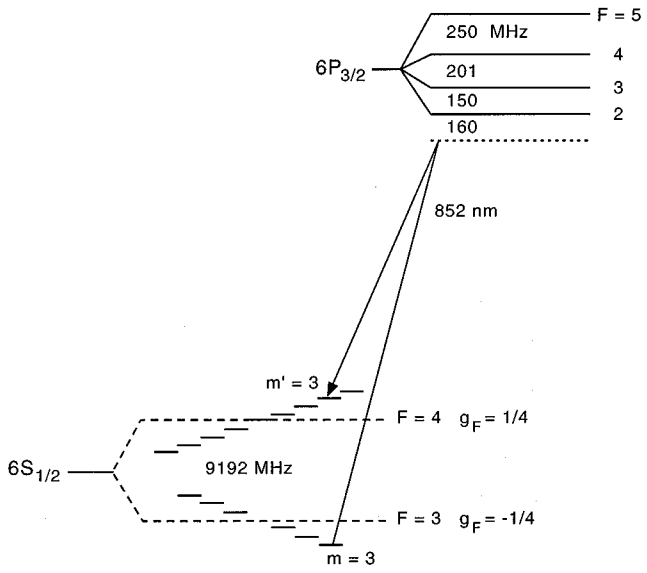

In past work we used a microwave approach [48] to measure these populations, which required substantial modification of the interaction region; here we use two-photon Raman spectroscopy [49,50], which has the advantage that we can measure the populations in-situ. In fact, we need only send an additional laser, an IR laser, into the interaction region. We take advantage of the fact that the mirrors forming the buildup cavity are transparent to infrared light, and so we can send the IR laser into the interaction region through these mirrors. Another advantage of Raman spectroscopy is that we can obtain additional information by taking spectra using different laser polarizations.

Since we need to know the populations to an accuracy of 1%, we need both accurate measurements of the Raman transitions and accurate calculations of the relative line strengths for those transitions. First we present some background information about Raman transitions. Then we present our novel approach for generating the necessary laser frequencies using only a single, external-cavity, diode laser. This is followed by a description of the data acquisition and analysis, in which we present our results for the integrated line intensity. We then present the results of two different methods to simulate the Raman line strengths, and evaluate the accuracy of these line strengths.

A.2. Raman transitions

Figure 27 shows the relevant energy levels for a velocity-insensitive Raman transition for cesium in the initial 6S $F = 3$ $m = 3$ state. To excite the Raman transition from this state to the 6S $F = 4$ $m = 3$ state, we use two co-propagating optical frequencies (ω_1 and ω_2), each detuned by 160 MHz from the $6P_{3/2}$ $F = 2$ intermediate state, with a difference frequency ($\Delta\omega$) approximately equal to the ground-state hyperfine splitting of 9.2 GHz.

This three-level system can be reduced to a two-level system [50, 51] with the Rabi frequency replaced by an "effective" Rabi frequency given by

$$\Omega^{\text{eff}}_{m_f m_i} = \frac{e^2}{2\hbar^2} \sum_k \frac{\langle 6S, F = 4, m_f \mid \boldsymbol{r} \cdot \boldsymbol{E}(\omega_1) \mid k \rangle \langle k \mid \boldsymbol{r} \cdot \boldsymbol{E}(\omega_1) \mid 6S, F = 3, m_i \rangle}{\Delta_k} \tag{A.1}$$

where Δ_k is the detuning of each laser frequency from the frequency of the transition to the intermediate

©1999 NRC Canada

state $|\ k\rangle$, $\boldsymbol{E}(\omega)$ is the oscillating electric field of the laser at frequency ω, and the sum is over all possible intermediate states, that is, all states in the $6P_{3/2}$ manifold that satisfy the selection rules.

In the perturbative limit, for which the interaction time, t, of the atoms with the Raman laser beam satisfies the condition $t \ll \pi\ /\ \Omega^{\rm eff}_{m_f m_i}$, the transition rate can be written as [52]

$$R(F=3, m_i \rightarrow F=4, m_f) = \frac{\pi}{2} N_i \left(\Omega^{eff}_{m_f m_i}\right)^2 L(\omega_1, \omega_2, t, \Delta\omega, \nabla \boldsymbol{B}) \tag{A.2}$$

which is Fermi's Golden Rule with the single-photon Rabi frequency replaced by the two-photon effective Rabi frequency. Here $L(\omega_1, \omega_2, t, \Delta\omega, \nabla \boldsymbol{B})$ is a line-shape factor that depends on the two laser frequencies, the interaction time, the frequency jitter between the two optical frequencies, and magnetic-field inhomogeneities.

The effective Rabi frequency can be expressed in terms of the single-photon Rabi frequencies Ω_{ik}:

$$\Omega^{\rm eff}_{m_f m_i} = \sum_k \frac{\Omega^*_{1k}\Omega_{2k}}{4\Delta^2_k} \tag{A.3}$$

where $\Omega_{ik} = (e\boldsymbol{r} \cdot \boldsymbol{E}(\omega_i))/\hbar$. From the effective Rabi frequency we can determine the laser power requirement for the Raman process. Consider the case where the Raman detuning is much larger than the excited-state hyperfine splittings (yet still much smaller than the fine-structure splittings). In this case, the effective Rabi frequency can be approximated by

$$\Omega^{\rm eff}_{m_f m_i} \simeq \frac{e^2 E(\omega_1) E(\omega_2)}{2\hbar^2 \Delta} \sqrt{\frac{3\hbar c^3 \pi \epsilon_o}{\tau e^2 \omega^3}} \left[A^{3,m_k}_{3,m_i} A^{3,m_k}_{4,m_f} + A^{4,m_k}_{3,m_i} A^{4,m_k}_{4,m_f}\right] \tag{A.4}$$

where τ is the lifetime of the $6P_{3/2}$ state and the A's are "transfer" coefficients, related to Clebsch–Gordan coefficients.

The factor containing the transfer coefficients represents the interference between different possible Raman amplitudes, and is a function of both the magnetic field and the laser polarization. For example, when σ^+ polarized light is used, as in ref. 32, only $\Delta m = +1$ transitions are driven, and the factor containing the transfer coefficients is large (about 0.2). However, for our magnetic-field configuration, we must use light that is linearly polarized along the direction of $\boldsymbol{B}$. In this case, only $\Delta m = 0$ transitions are driven, and the factor containing the transfer coefficients is small (about 0.02). This decrease is due to destructive interference from paths involving the $6P_{3/2}$ $F' = 3$ and $F' = 4$ states.

To obtain complete population transfer, the product of the effective Rabi frequency and the interaction time must satisfy the equation for a π pulse, $\Omega^{\rm eff}_{m_f m_i} t = \pi$. Thus, for a given interaction time t and detuning Δ, this π-pulse equation along with (A.4) can be used to determine the required laser intensity. In our experiment, the interaction time is about 10 μs, which, according to (A.4), requires an effective Rabi frequency of 315×10^3 for a π pulse. We use a power density of 20 mW/cm^2 at each Raman frequency, and an average detuning of about 300 MHz, which gives an effective Rabi frequency of 16×10^3 rad/s, corresponding to incomplete population transfer.

The line-shape factor, L, in (A.2) is sensitive to the interaction time, t. Assuming the width of the Raman transition to be limited by the interaction time, averaging over the longitudinal velocity spread in the beam [48] gives the width of the Raman transition, $\Delta\nu$(FWHM), as $(1.07)\bar{\upsilon}/l$, where l is the interaction length and $\bar{\upsilon}$ is the most probable velocity in the beam. For our nozzle temperature of 250°C (which gives $\bar{\upsilon} = 300$m/s) and our interaction length of 3 mm, this equation give $\Delta\nu$(FWHM) = 100 kHz. Our measured typical width is 120 kHz, showing that the dominant effect on L is indeed the interaction time.

A.3. Raman laser

The most difficult requirement for Raman spectroscopy is the generation of two optical frequencies that have a relative jitter much less than the line width for the transition of interest. For low frequencies,

©1999 NRC Canada

Fig. 28. Typical modulation spectrum for the Raman laser, measured with a scanning Fabry–Perot interferometer. The first-order sidebands, ω_1 and ω_2, drive the Raman transition and differ by 9.2 GHz.

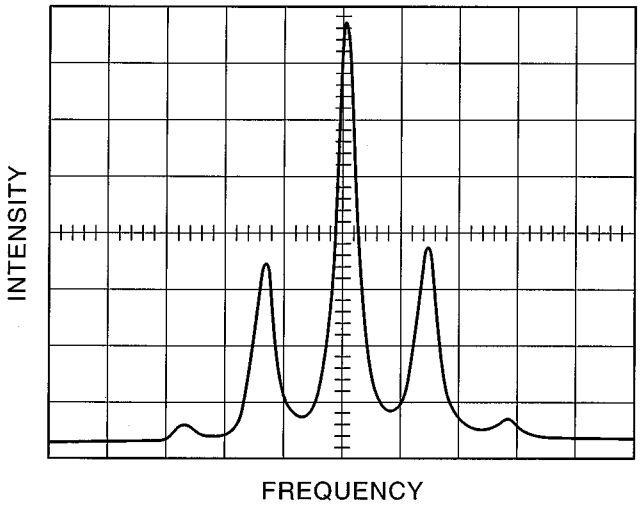

Fig. 29. Schematic of the apparatus used to control the Raman diode laser.

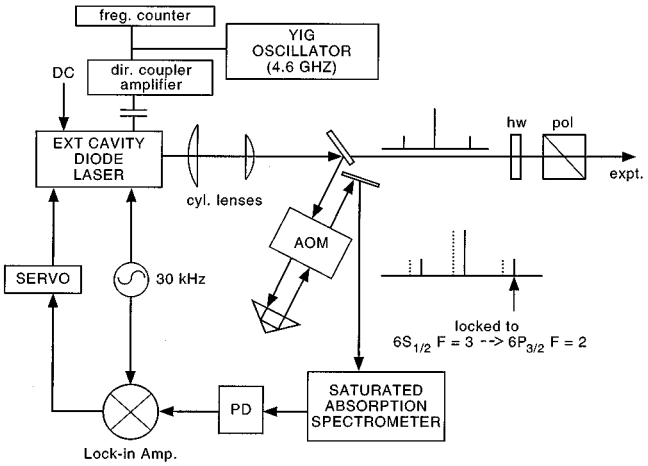

one option is to use a diode laser and modulate its injection current to produce correlated sidebands. However, for oscillation frequencies above 2 to 3 GHz, the modulation response of diode lasers drops off rapidly [53].

Since we require a modulation current of 4.6 GHz, we need to increase the modulation response. We do this by using an external-cavity diode laser with a large modulation current [54] and with the free spectral range of the external cavity matched to the modulation frequency [23]. This type of technique has been used to demonstrate a single-laser, magneto-optic trap for rubidium [55–57].

Specifically, we use an STC LT50A03U diode laser with a grating-feedback, external cavity. This laser is similar to the other three diode lasers in our experiment (hyperfine pump, Zeeman pump, and probe). However, it differs in that we set the external-cavity, free spectral range near 4.6 GHz, which ensures that upon modulation at 4.6 GHz, the first two sidebands have the proper separation of 9.2

©1999 NRC Canada

GHz. Moreover, the unused carrier is detuned by 4.6 GHz from any transitions, which enhances the two-photon rate relative to the one-photon rate. A typical modulation spectrum is shown in Fig. 28.

A schematic of the apparatus used to generate the two correlated frequencies is shown in Fig. 29. We operate the laser with an injection current of 80 mA which produces 25 mW of light, 13 mW of which is coupled out by the grating.

The injection current is modulated by a tunable microwave source (Yttrium–Iron–Garnet (YIG) oscillator, Avantek model AV-7403), which produces microwaves over a range from 4 to 8 GHz. We use a JILA-designed diode-laser driver to supply low-noise current to the YIG oscillator. The resulting line width of the oscillator, limited by noise on the current driver, is 30 kHz. The microwaves are sent through an isolator, a directional coupler, a +20 dBm amplifier, and a very short section of RG-174 coaxial cable, before coupling into the diode laser via a 100 pF ceramic capacitor.

A pair of cylindrical lenses transforms the elliptical laser beam into a nearly circular shape before it enters the vacuum chamber, which results in symmetric Raman line shapes. Any additional structure on the laser beam, which can cause significant line-shape asymmetries, is removed with an iris.

To enhance the two-photon rate relative to the one-photon rate, we use a large detuning from the excited state. To hold this detuning constant while scanning the difference frequency, $\omega_1 - \omega_2$, we send a fraction of the modulated output from the laser first through a double-pass acousto-optic modulator (AOM; 80 MHz), which shifts the laser light frequency up by 160 MHz, and then into a saturated absorption spectrometer.

A complicated saturated-absorption spectrum can arise when two different frequencies are resonant in the vapor cell. In this case, the two-level system can become a three-level system, producing a spectrum in which "peaks" can become "dips" or even dispersion shapes as the difference frequency is scanned. The transitions between both the $F = 3$ and $F = 2$ states and the $F = 4$ and $F = 5$ states remain two-level systems with normal line shapes; thus either can be used for locking the laser frequency. We lock the high-frequency side band to the transition between the $F = 3$ and $F = 2$ states.

Since our laser power is low and our interaction time short, we need to transfer a significant fraction of light to the first-order side bands. If we increase the microwave power greater than that used to generate the spectrum in Fig. 28, higher order side bands appear, which give rise to more than one pair of frequencies with the proper difference and thus complicate the spectrum. To attain the appropriate power in the sidebands, we adjust the injection current while monitoring the amplitude of the sidebands. The proper condition is characterized by a small range of injection currents over which the modulation spectrum is independent of the current. The width of this region, due in part to a circuit resonance in the microwave coupling, is about 300 MHz. Although less microwave power is required when operating near the peak of the resonance, the sideband power variations are large when the YIG oscillator is tuned. Therefore, we operate in the wings of the resonance, so that the power in the first two sidebands varies by only 10% over the course of a 45 MHz scan.

The Raman laser beam intersects the atomic beam a few mm downstream from the dye-laser beam. To prevent retro-reflection of the exiting Raman beam, which can cause velocity selection [49], we place a black metal beam dump at the exit of the chamber.

A.4. Raman spectra

A typical spectrum of atoms that have undergone a Raman $\Delta m = 0$ transition (linear Raman-laser polarization, parallel to the magnetic field) is shown in Fig. 30*a*. This spectrum is attained for a cesium beam that has undergone hyperfine pumping only, which empties one of the hyperfine states. Atoms that have undergone the Raman transition repopulate the previously emptied hyperfine state, and are then detected in the usual manner.

To attain the spectrum shown in Fig. 30*a*, we set the YIG oscillator frequency so that the difference frequency, $\omega_1 - \omega_2 = 2\omega_{\mathrm{YIG}}$, is just below the first Raman resonance frequency, and then slowly increase the difference frequency by small steps, 1600 steps in all. At each step, the fluorescence is integrated and digitized.

©1999 NRC Canada

Fig. 30. Spectrum of cesium atoms having undergone Raman transitions (*a*) when only hyperfine pumping is performed and (*b*) when both hyperfine and Zeeman pumping are performed. The Raman laser is linearly polarized parallel to the magnetic field, so only $\Delta m = 0$ transitions are driven. The asymmetry in (*a*) is due to hyperfine mixing of the $6P_{3/2}$ levels, not to the population distribution. The scan range in (*b*) is reduced since all but two of the peaks are negligible; note that the width of the transition in (*b*) is 120 kHz. Note also the difference in vertical scale between (*a*) and (*b*): the main peak is about seven times more intense in (*b*) than in (*a*) because the population of the other six magnetic sublevels has been transferred to one of the extreme sublevels.

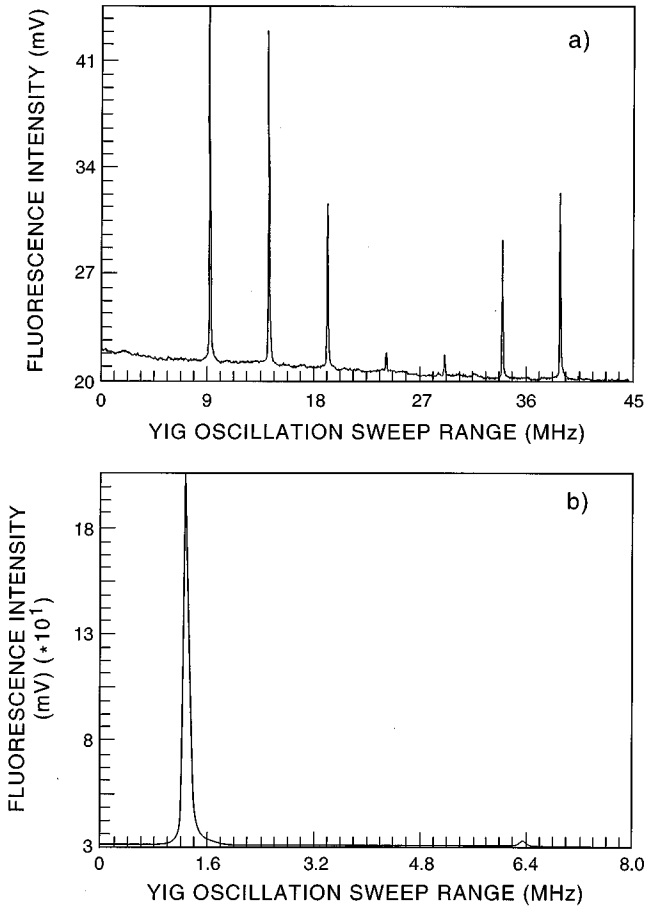

A similar scan for a spin-polarized beam (which underwent both hyperfine and Zeeman pumping) is shown in Fig. 30*b*. Since all but two of the sublevels are empty in this case, the scan range is reduced to 8 MHz. From this data, it can be seen that the line width for these transitions is just above 100 kHz. Note also that, as expected, the intensity of the main peak in this spectrum is seven times larger than that of the corresponding peak in Fig. 30*a*. We can also perform a detailed analysis of the Raman transition by taking narrow-range, high-resolution scans of the individual peaks.

There are several features in the long-range scans in Fig. 30 that must be considered in using Raman spectra for the determination of populations. First, the spectrum of cesium without spin polarization,

©1999 NRC Canada

which should thus have equal populations in all the magnetic sublevels, nevertheless shows a dramatic asymmetry, due to hyperfine mixing of the $6P_{3/2}$ states by the 6.4 G magnetic field. Second, the detuning (by -160 MHz) from the $6P_{3/2}$ $F' = 2$ state is not large enough to neglect the effects of either hyperfine or Zeeman structure, both of which significantly alter the Raman spectrum. And third, there is a background signal that is a function of the difference frequency. This background signal is due to off-resonant excitation to the $6P_{3/2}$ $F' = 3$ state and is proportional to the power in the high-frequency Raman sideband. Thus, by monitoring this fluctuation in background intensity, we monitor the fluctuation in laser power. We then normalize the signal intensity for fluctuations in the sideband intensity. Note that since the Raman transition is a two-photon process, the transition probability scales as the square of the Raman laser power.

A.5. Determination of population distributions

We now show how to extract sublevel populations, P_i, from the spectrum of atoms that have undergone a Raman transition.

The fractional population f_i in sublevel m_i can be written as

$$f_i = \frac{P_i}{\sum_k P_k} \tag{A.5}$$

To simplify the analysis of the Raman spectrum so that each transition specifies a unique sublevel, we consider only $\Delta m = 0$ transitions. Our method is analogous to that used in ref. 32 except that they considered $\Delta m = +1$ transitions.

Since the peak height is sensitive to factors other than population, such as magnetic field broadening, we measure the integrated transition rate, that is, the area (A) under the Raman resonance. This area is given by

$$A_i \propto P_i \; S_i \; I_i^2 \tag{A.6}$$

where S_i is the line strength for the Raman transition and I_i is the intensity of the laser beam at the frequency of the sideband. Thus, from (A.5) and (A.6), the fractional population can be expressed as

$$f_i = \frac{A_i}{\sum_k A_k \left(\frac{S_i}{S_k}\right)\left(\frac{I_i^2}{I_k^2}\right)} \tag{A.7}$$

Finally, to normalize for fluctuations in the laser sideband intensity, we divide each area, A_i, by the square of the background signal, BG_i

$$f_i = \frac{A_i}{\sum_k A_k \left(\frac{S_i}{S_k}\right)\left(\frac{BG_i^2}{BG_k^2}\right)} \tag{A.8}$$

Note that we only need to know relative Raman line strengths and relative changes in the intensity of the background.

To measure A_i and BG_i, we take several 200-point, high-resolution scans of the two peaks shown in Fig. 30*b*, as well as the usually undetectable third peak. To determine the background signal, we take the first and last five points of a scan (single Raman peak) and then fit a straight line through them. We then performed a point-by-point subtraction of this line from the data. In addition, we use this line to calculate the average background, BG_i, used in the expression for the fractional populations, (A.8).

We have five different ways to reverse the handedness of the interaction region, and we obtain our final PNC value by averaging these results. Since three of these ways, the b-, m-, and a-reversals, reverse the spin polarization (and thus the initial-state magnetic sublevels that are populated), we need to take measurements of fractional population for the eight possible configurations of b-, m-, and a-reversal,

©1999 NRC Canada

and then average these results to obtain $\langle f_{\pm 3}\rangle_{\rm bma}$ for calibrating the PNC results. Typical values for the fractional population in the magnetic sublevel of interest are $\langle f_{\pm 3}\rangle_{\rm bma} = 96$ to 97% (with $\langle f_{\pm 2}\rangle_{\rm bma} = 3$ to 4 %) for higher atomic beam densities, and $\langle f_{\pm 3}\rangle_{\rm bma} = 98$ to 99% for lower atomic beam densities, because of light scattering issues discussed in ref. 20. We measure the spin polarization both before and after each PNC data run.

For the case where we prepare the initial 6S $F = 4$ state, it is more difficult to extract the fractional populations. This difficulty arises because we use linearly polarized light to excite the Raman transition to the 6S $F = 3$ state, which cannot excite atoms from either the 6S $F = 4$ $m = 4$ or $m = -4$ sublevel to the 6S $F = 3$ state. Fortunately, however, we do not need as accurate a measurement of the populations for the 6S $F = 4$ state since, for the $\Delta F = -1$ transition to the 7S $F = 3$ state, the Clebsch–Gordan coefficient for the $m = 4$ state is much larger than those for the other states. Thus, as long as the population in the $m = 4$ sublevel is at least 90%, any contribution of the other sublevels to (38), and hence to the PNC results, is negligible.

A.6. Theoretical determination of Raman line strengths

To determine the ratio of the line strengths S_i/S_k necessary for calculation of the fractional populations, (A.8), we use two methods: we calculate the line strengths and we measure them; the results of these two methods agree well. In this section we describe the theoretical determination.

We first show that the precision we require in the calculated line-strength ratios is relatively low. The dependence of the uncertainty in the fractional population, $f_{\pm 3}$, on the uncertainty in the line strength ratio, $S_{\pm 3}/S_k$, is given by

$$\Delta f_{\pm 3} = \frac{\partial f_{\pm 3}}{\partial\left(\frac{S_{\pm 3}}{S_k}\right)}\Delta\left(\frac{S_{\pm 3}}{S_k}\right) \tag{A.9}$$

By (A.8), the fractional uncertainty in $f_{\pm 3}$ can be written as

$$\frac{\Delta f_{\pm 3}}{f_{\pm 3}} = f_k\left[\Delta\left(\frac{S_{\pm 3}}{S_k}\right)\right]\left(\frac{BG_{\pm 3}}{BG_k}\right)^2 \simeq f_k\,\Delta\left(\frac{S_{\pm 3}}{S_k}\right) \tag{A.10}$$

where we have neglected the background (laser power) correction because it is small for adjacent sublevels. Since we need this fractional uncertainty to be no greater than 1%, (as explained in Sect. 5), and since our spin polarization is about 95%, we require the uncertainty in the line-strength ratio $S_{\pm 3}/S_k$ to be no greater than 20%. For optical pumping of the 6S $F = 3$ state, and considering Raman transitions with $\Delta m = 0$, we arrive at the estimates: $S_{-3}/S_{-2} \simeq 1$ and $S_3/S_2 \simeq 2$. Using these estimates, we calculate that the required fractional uncertainties in the line-strength ratios are $< 20\%$ for $\Delta(S_{-3}/S_{-2})/(S_{-3}/S_{-2})$ and $< 10\%$ for $\Delta(S_3/S_2)/(S_3/S_2)$. Note that these estimates become more favorable as the spin polarization increases. Since both f_1 and f_{-1} are less than 1%, the uncertainties in the line-strength ratios, S_3/S_1 and S_{-3}/S_{-1}, are negligible.

Two factors make the line-strength calculations difficult for our particular situation. First, we use a small detuning from the intermediate state (since we have only a 10 μs interaction time and a limited amount of diode-laser power). Thus, we must include both the hyperfine and Zeeman structure of the intermediate state. Second, to determine the spin polarization under the same conditions as in the PNC experiment, we must excite the Raman transitions in a 6.4 G magnetic field. This magnetic field mixes the hyperfine states of the intermediate state. These two factors lead to a large number of Raman amplitudes that interfere and cause the asymmetry shown in Fig. 30*a*.

For a magnetic field along the z axis, the $6P_{3/2}$ state, taking into account hyperfine mixing, can be written as

$$\overline{\mid 6P_{3/2}Fm\rangle} = \mid 6P_{3/2}Fm\rangle + \sum_{F'\neq F} \mid 6P_{3/2}F'm\rangle\frac{\langle 6P_{3/2}F'm \mid L_z + 2S_z \mid 6P_{3/2}Fm\rangle}{E_F - E_{F'}} \tag{A.11}$$

©1999 NRC Canada

Fig. 31. Calculated line strengths for Raman transitions under the same conditions as in Fig. 30. Continuous lines are from perturbation theory, while broken lines are for full diagonalization.

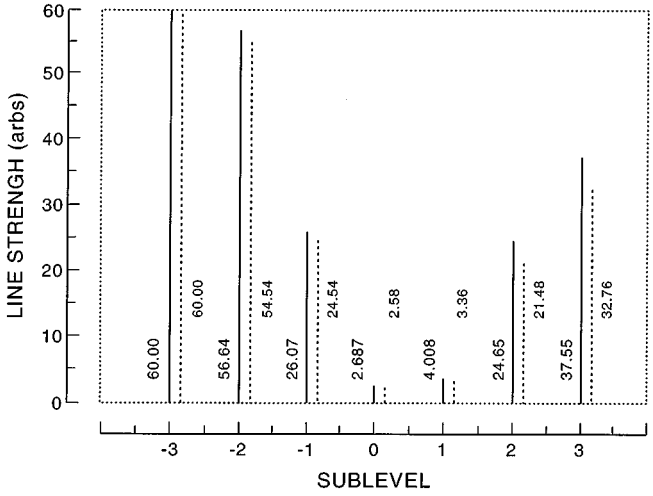

Using angular momentum algebra, with the substitution $J_z + S_z = L_z + 2S_z$, this expression can be written as

$$\overline{\mid 6P_{3/2}F = 4, m\rangle} = \mid 6P_{3/2}4, m\rangle + .015\sqrt{16 - m^2} \mid 6P_{3/2}3, m\rangle + .008\sqrt{25 - m^2} \mid 6P_{3/2}5, m\rangle \quad \text{(A.12)}$$

where we have taken B as 6.4 G. This expression shows that the $F = 4, m = 0$ state actually has some of the $F = 3, m = 0$ and $F = 5, m = 0$ states mixed in. This mixing of $m = 0$ states causes the appearance of a middle peak in Fig. 30*a*.

The expression for the effective Rabi frequency, (A.1), can be separated into two factors:

$$\Omega^{\text{eff}}_{m_f m_i} = \left[\frac{e^2 \mid \boldsymbol{E} \mid^2}{2\hbar^2} \mid \langle 6P_{3/2} \parallel \boldsymbol{r} \parallel 6S_{1/2}\rangle \mid^2\right] \sum_k \frac{A^{k,m}_{3,m_i} A^{k,m}_{4,m_f}}{\Delta_k} \quad \text{(A.13)}$$

the first factor consisting of quantities common to all of the amplitudes, such as the reduced matrix element, the second factor consisting of a sum of Clebsch–Gordan coefficients over all possible intermediate states, which contains the interference information. Since we are interested only in relative line strengths, we need only calculate the second factor.

The results of our calculation of line-strength ratios are shown by the continuous lines in Fig. 31, where we use the same parameters as those used to obtain the experimental spectrum in Fig. 30*a*, except that here we assume a uniform initial m population distribution, which is not the case for the experimental spectrum. Nevertheless, comparison of the two spectra reveals several important points. First, since the calculation reproduces the experimental asymmetry, it should also reproduce the relative line strengths. Second, since the agreement between the calculated line strengths and those determined from the experiment is good (better than 10%), the nonuniformity in the experimental m populations caused by the hyperfine pumping must be small, on the order of a few percent. And finally, determination of the spin polarization relies only on the ratio of adjacent peaks; these ratios agree to about 5%.

A second calculation was performed for us by a group at JILA. [2] That calculation was similar to ours except that, rather than treating the $6P_{3/2}$ state using perturbation theory, a full rediagonalization of

[2] P. Marte. Unpublished work.

©1999 NRC Canada

Fig. 32. Technique of "hiding the atoms," used to create several 6S $F = 3$ magnetic sublevels with equal populations. In step one, the 6S $F = 4$ atoms are Zeeman pumped into the $m = 4$ magnetic sublevel. In step two, these atoms in the $m = 4$ sublevel are then hyperfine pumped into the $m = 3, 2, 1$, and possibly 0 magnetic sublevels of the $F = 3$ state. As a result, the $F = 4$ state is empty; the $m = -3, -2$, and -1 sublevels of the $F = 3$ state (which are the sublevels to be probed) have not been perturbed; and the atoms that have undergone the pumping are in sublevels that will not be probed and thus are "hiding."

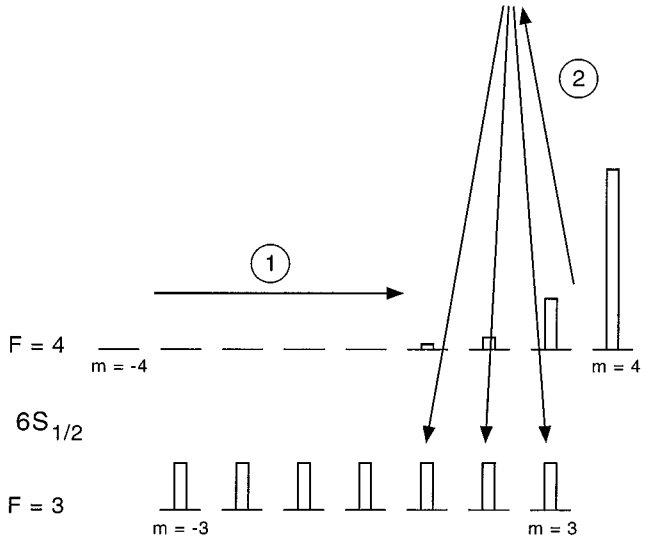

the $6P_{3/2}$ state was performed with respect to the Zeeman Hamiltonian. This procedure deals properly with the detunings, energies, and mixing, and is shown by the broken lines in Fig. 31. Once again the agreement is very good, especially for adjacent Raman peaks.

We now describe our experimental determination of line-strength ratios via a technique called "hiding the atoms." One might expect that optimal experimental conditions for measuring line strengths would consist of having a uniform population distribution, which we nearly have coming out of our cesium oven. However, when both of the lowest level hyperfine states are populated, our Raman detection scheme does not work well, because Raman "spin flips" can occur in both directions, resulting in no net change in population. Therefore we want to have a uniform population distribution in one hyperfine state, and no population in the other hyperfine state. However, use of the hyperfine-pumping process to empty one of the hyperfine states, as above, can perturb the population distribution in the other hyperfine state because of the different Clebsch–Gordon coefficients for the various m transitions.

To avoid this problem, we use a procedure which we call hiding the atoms, in which we empty one hyperfine state yet still retain a uniform population distribution in a few, though not all, of the m sublevels in the other hyperfine state. This procedure, shown in Fig. 32, uses sequential, two-step optical pumping (in contrast to our procedure to prepare the initial state of the cesium atoms for the PNC experiment, which uses simultaneous two-step optical pumping). First we move all the atoms in the 6S $F = 4$ state over to the $m = 4$ sublevel by Zeeman pumping. (We use σ^+ polarized laser light to excite the transition between the 6S $F = 4$ and the $6P_{3/2}$ $F = 5$ states). This process leaves the $F = 3$ hyperfine state unperturbed. Then we move these atoms up to the 6S $F = 3$ state by hyperfine pumping. Since most of the atoms start in the $m = 4$ sublevel of the $F = 4$ state (with a few in the

©1999 NRC Canada

Table 3. Comparison of experimental and theoretical relative Raman line strengths for the extreme magnetic sublevels. These values agree to within 3% for the worst case. Also shown are the predictions from a less rigorous perturbative simulation.

Line-strength ratio	Experiment	Full simulation	Perturbative simulation
S_{-2}/S_{-3}	0.902(5)	0.909	0.944
S_2/S_3	0.647(12)	0.657	0.656

neighboring sublevels), the atoms move predominantly to the $m = 0$, 1, 2, and 3 magnetic sublevels of the $6P_{3/2}$ $F = 3$, thus leaving the other $6P_{3/2}$ $F = 3$ sublevels unperturbed. Thus this two-step process empties the $F = 3$ hyperfine state and leaves the $F = 4$ hyperfine state with a few magnetic sublevels ($m = -3$, -2, and -1) with their original (uniform) populations.

We then excite $\Delta m = 0$ Raman transitions from the three $F = 4$ sublevels ($m = -3$, -2, and -1) that have their original uniform populations. Thus, our measured line intensities for atoms that have undergone the Raman transitions are equal to the relative line strengths. By reversing the polarization of the Zeeman pumping laser, we measure the relative line strengths of the $F = 4, m = 3, 2$, and 1 sublevels as well. Although the method of "hiding the atoms" provides relative line strengths for only the outer sublevels, these are the relevant sublevels for the PNC experiment.

A comparison of the theoretical and experimental line strengths is given in Table 3.

Even with our hiding-the-atoms technique, the population distribution in the sublevels being probed may not be 100% uniform. For example, in the first step of the process, Zeeman pumping, we want to move any atoms in the $F = 4$, $m = -4$ sublevel over to the $F = 4$, $m = 4$ sublevel. However, the Clebsch–Gordan coefficient for excitation of the $F = 4$, $m = -4$ sublevel to the intermediate $F' = 5$ $m' = -3$ sublevel is only 1/45, and thus the process is slow. Moreover, this same $m = -4$ sublevel has the greatest Zeeman shift, and so is slightly detuned from the Zeeman pumping light, another factor that slows down the Zeeman pumping. And finally, some of the atoms in the beam have Doppler shifts that detune them even further from resonance.

In light of these considerations, we have measured the effect of any leftover population in the $F = 4$ hyperfine state both by attenuating the Zeeman pump laser power and by increasing the OP magnetic field (which moves the transition frequency further away from resonance with the Zeeman laser frequency). From these measurements, we are confident that the initial populations for the measurement of line strengths are uniform to within 1%.

A third method by which we can determine the spin polarization of the initial cesium state is by directly monitoring the transition rate between the 6S and 7S states while varying the spin polarization of the initial state. As shown in Appendix C, the expression for the transition rate between the 6S and 7S states for $\Delta F = 0$, (C.1), has an $\alpha\beta$ interference term that is proportional to the quantity $\sum_m f_m m$. Thus, we can use this equation to predict how a change in the population distribution will affect the transition rate, and thus the signal intensity. We can then compare this prediction with direct measurement. To perform the direct measurement, we vary the fractional populations by attenuating the Zeeman pump laser, and then measure the change in the transition intensity. We then measure these new fractional populations by using Raman spectroscopy, calculate the quantity $\sum_m f_m m$, and use this in (C.1) to predict the transition intensity. We find that our experimental measurements agree with our theoretical predictions to within 1%, even for cases in which the population distribution is very asymmetric.

©1999 NRC Canada

Appendix B. Measurement of dye-laser polarization

Since the wave vector $\hat{k}$ of the dye-laser beam defines the y axis for the PNC coordinate system, its polarization can be written

$$\boldsymbol{\epsilon} = \epsilon_z \hat{z} + (\epsilon_{\mathrm{R}} + i\epsilon_I)\hat{x} = \epsilon_z \left[\hat{z} + \left(\frac{\epsilon_{\mathrm{R}}}{\epsilon_z} + i \frac{\epsilon_I}{\epsilon_z} \right) \hat{x} \right] \tag{B.1}$$

where $\hat{x}$ and $\hat{z}$ refer to the PNC coordinate system. Here we use a phase convention in which the polarization component along $\hat{z}$ is defined to be real, while the x component can have a real part (in phase with the z component) and an imaginary part (out of phase). In (B.1), we reference the amplitudes of the real and imaginary parts of the x component to the amplitude of the z component.

We developed two techniques for measuring the polarization state $\boldsymbol{\epsilon}$. The first involves rotating a polarizer and the second involves rotating a $\lambda/4$ plate.

Rotating polarizer technique

Our first technique for measuring $\boldsymbol{\epsilon}$ is to use a rotating polarizer, similar to refs. 58, 59. The system is configured as in Fig. 7, except that we remove the $\lambda/4$ plate located after the PBC. We mount the polarizer in a rotation stage driven by a stepper motor geared for 720 steps per rotation. To ensure that only circularly polarized light is incident upon the photodiode that is located after the PBC, we mount a $\lambda/4$ plate onto the rotation stage after the polarizer. So that the photodiode operates in the linear regime, we also put a $\times 1000$ attenuator (whose polarizing properties were tested) in front of the photodiode. We operate the photodiode in photoconductive mode (biased to 70 V), with its cover window removed.

The transmission axis of the polarizer is initially aligned with the z axis of the PNC coordinate system. The polarizer is then rotated in steps of 22.5^{o} through a total of 16 positions ($\theta_1 \ldots \theta_{16}$). At each position, the photocurrent is integrated and digitized. Also at each position, the polarization is modulated at the rate used during the PNC experiment, so we measure the polarization $\boldsymbol{\epsilon}$ for both states of the p-reversal.

The polarization vector in (B.1) can be written using the Jones matrix formalism [60] as

$$\boldsymbol{\epsilon} = \begin{pmatrix} \boldsymbol{\epsilon} \cdot \hat{x} \\ \boldsymbol{\epsilon} \cdot \hat{z} \end{pmatrix} = \epsilon_z \begin{pmatrix} \epsilon_{\mathrm{R}}/\epsilon_z + i\epsilon_I/\epsilon_z \\ 1 \end{pmatrix} \tag{B.2}$$

If $\boldsymbol{\epsilon}$ is incident upon a polarizer whose transmission axis is at an angle θ with respect to the PNC coordinate system, then the polarization vector $\boldsymbol{\epsilon}'$ in the frame of the polarizer ($\hat{x}'$, $\hat{z}'$) is

$$\boldsymbol{\epsilon}' = R(\theta)\boldsymbol{\epsilon} = \begin{pmatrix} \cos\theta & -\sin\theta \\ \sin\theta & \cos\theta \end{pmatrix} \begin{pmatrix} \epsilon_{\mathrm{R}}/\epsilon_z + i\epsilon_I/\epsilon_z \\ 1 \end{pmatrix} \epsilon_z \tag{B.3}$$

Since the polarizer will transmit only one component, say $\hat{z}'$, the resulting transmitted intensity is

$$\begin{aligned} I(\theta) &= \left(\boldsymbol{\epsilon}' \cdot \hat{z}'\right)\left(\boldsymbol{\epsilon}' \cdot \hat{z}'\right)^* \\ &= \left\{ \frac{1}{2}\left[1 + \left(\frac{\epsilon_{\mathrm{R}}}{\epsilon_z}\right)^2 + \left(\frac{\epsilon_I}{\epsilon_z}\right)^2 \right] + \frac{1}{2}\left[1 - \left(\frac{\epsilon_{\mathrm{R}}}{\epsilon_z}\right)^2 - \left(\frac{\epsilon_I}{\epsilon_z}\right)^2 \right] \cos 2\theta + \frac{\epsilon_{\mathrm{R}}}{\epsilon_z} \sin 2\theta \right\} \epsilon_z^2 \end{aligned} \tag{B.4}$$

Thus, the transmitted intensity has three terms: one that is constant, one that varies like $\cos 2\theta$, and one that varies like $\sin 2\theta$. This suggests using a discrete Fourier analysis to extract ϵ_z^2, $\epsilon_{\mathrm{R}}/\epsilon_z$, and ϵ_I/ϵ_z. In fact, a discrete Fourier analysis is equivalent to a least-squares fit to a function of the form $I(\theta) = C_1 + C_2 \cos 2\theta + C_3 \sin 2\theta$. For the least-squares fit we define a function

$$\chi^2 = \sum_{i=1}^{16} \left(I(\theta_i) - C_1 - C_2 \cos 2\theta_i - C_3 \sin 2\theta_i \right)^2 \tag{B.5}$$

©1999 NRC Canada

With the conditions: $\partial\chi^2/\partial C_1 = 0$; $\partial\chi^2/\partial C_2 = 0$; $\partial\chi^2/\partial C_3 = 0$, we obtain the three equations

$$C_1 = \frac{1}{16}\sum_{i=1}^{16} I(\theta_i) \tag{B.6}$$

$$C_2 = \frac{1}{8}\sum_{i=1}^{16} I(\theta_i)\cos 2\theta_i \tag{B.7}$$

$$C_3 = \frac{1}{8}\sum_{i=1}^{16} I(\theta_i)\sin 2\theta_i \tag{B.8}$$

Here, the equivalence of the least-squares technique and the discrete Fourier analysis is clear. Now, we can make the following identifications:

$$\frac{C_1 + C_2}{2} = \epsilon_z^2 \tag{B.9}$$

$$\frac{2C_3}{C_1 + C_2} = \frac{\epsilon_{\mathrm{R}}}{\epsilon_z} \tag{B.10}$$

$$\frac{C_1^2 - C_2^2 - 4C_3^2}{(C_1 + C_2)^2} = \left(\frac{\epsilon_I}{\epsilon_z}\right)^2 \tag{B.11}$$

This last equation shows one of the limitations for the rotating polarizer technique. Since it determines the quantity $(\epsilon_I/\epsilon_z)^2$, we cannot distinguish between left- and right-circular polarization. Moreover, this technique cannot distinguish between circularly polarized light and partially polarized light.

Retardance technique

Our second technique for measuring $\boldsymbol{\epsilon}$ involves a rotating $\lambda/4$ plate and is slightly more general than the rotating polarizer technique. The rotating $\lambda/4$ plate can distinguish left-circular polarization from right-circular polarization, provided we know the orientation of the fast axis of the $\lambda/4$ plate (usually specified by the manufacturer). Also, this technique can distinguish circular polarization from partial polarization. For these reasons, we can go one step beyond the Jones matrix analysis and instead use Mueller matrices and Stokes vectors [61, 62].

To implement this technique, we first need to measure the actual retardance of the waveplate, which can differ from $\pi/2$. Consider light, linearly polarized along $\hat{z}$, that is incident upon a waveplate with retardance φ. The waveplate is positioned in the stepper-motor mount and is rotated in exactly the same manner as the polarizer above. The transmitted light is analyzed using a polarizer whose transmission axis is along $\hat{z}$. Using the Jones matrix formalism , the polarization transmitted by the waveplate is

$$\boldsymbol{\epsilon} = \begin{pmatrix} \cos\theta & -\sin\theta \\ \sin\theta & \cos\theta \end{pmatrix} \begin{pmatrix} 1 & 0 \\ 0 & \mathrm{e}^{i\varphi} \end{pmatrix} \begin{pmatrix} \cos\theta & \sin\theta \\ -\sin\theta & \cos\theta \end{pmatrix} \begin{pmatrix} 0 \\ 1 \end{pmatrix} \epsilon_o \tag{B.12}$$

The intensity of light transmitted by the analysis polarizer is then

$$\begin{aligned} I(\theta) &= \left(\boldsymbol{\epsilon}\cdot\hat{z}\right)\left(\boldsymbol{\epsilon}\cdot\hat{z}\right)^* \\ &= \frac{\epsilon_o^2}{4}\left[(3+\cos\varphi) + (1-\cos\varphi)\cos 4\theta\right] \end{aligned} \tag{B.13}$$

Again, we can perform a discrete Fourier analysis and obtain

$$C_1 = \frac{1}{16}\sum_{i=1}^{16} I(\theta_i) \tag{B.14}$$

©1999 NRC Canada

$$C_4 = \frac{1}{8}\sum_{i=1}^{16} I(\theta_i)\cos 4\theta_i \tag{B.15}$$

The retardance can be identified as $\cos\varphi = 2[(C_1 - C_4)/(C_1 + C_4)] - 1$.

Our implementation of this method is similar in principle to refs. 59 and 63. The configuration is shown in Fig. 7, where now the polarizer located after the PBC is fixed (along $\hat{z}$) and the $\lambda/4$ plate is rotating in the stepper-motor-driven mount. Here it does not matter that linear light is incident upon the photodiode located after the PBC, because the orientation of the linear polarization is always constant. As in the previous technique, we place a $\times 1000$ attenuator in front of the photodiode to ensure linearity of response.

The Stokes vector for our laser beam is written

$$\boldsymbol{S} = \begin{pmatrix} S_0 \\ S_1 \\ S_2 \\ S_3 \end{pmatrix} = \begin{pmatrix} \langle\epsilon_z^2\rangle + \langle\epsilon_x^2\rangle \\ \langle\epsilon_z^2\rangle - \langle\epsilon_x^2\rangle \\ \langle 2\epsilon_z\epsilon_x\cos\xi\rangle \\ \langle 2\epsilon_z\epsilon_x\sin\xi\rangle \end{pmatrix} = \epsilon_z^2 \begin{pmatrix} 1 + \left(\frac{\epsilon_R}{\epsilon_z}\right)^2 + \left(\frac{\epsilon_I}{\epsilon_z}\right)^2 \\ 1 - \left(\frac{\epsilon_R}{\epsilon_z}\right)^2 - \left(\frac{\epsilon_I}{\epsilon_z}\right)^2 \\ 2\epsilon_R\epsilon_z \\ 2\epsilon_I\epsilon_z \end{pmatrix} \tag{B.16}$$

where the brackets denote time averaging and ξ is the phase difference between the x and z components. Unlike the Jones vector, which specifies field information, the Stokes parameters S_0, S_1, S_2, and S_3 specify intensity information. The effect of a $\lambda/4$ plate with retardance φ and fast-axis orientation θ on a laser beam with Stokes vector $\vec{S}$ is given by:

$$\boldsymbol{S}' = \begin{pmatrix} 1 & 0 & 0 & 0 \\ 0 & \cos^2 2\theta + \cos\varphi\sin^2 2\theta & (1-\cos\varphi)\sin 2\theta\cos 2\theta & -\sin\varphi\sin 2\theta \\ 0 & (1-\cos\varphi)\sin 2\theta\cos 2\theta & \sin^2 2\theta + \cos\varphi\cos^2 2\theta & \sin\varphi\cos 2\theta \\ 0 & \sin\varphi\sin 2\theta & -\sin\varphi\cos 2\theta & \cos\varphi \end{pmatrix} \boldsymbol{S} \tag{B17a}$$

$$= \begin{pmatrix} S_0 \\ S_1\cos^2 2\theta + S_2\sin 2\theta\cos 2\theta + S_3\sin 2\theta \\ S_1\sin 2\theta\cos 2\theta + S_2\sin^2 2\theta - S_3\cos 2\theta \\ -S_1\sin 2\theta + S_2\cos 2\theta \end{pmatrix} \tag{B17b}$$

Here we have assumed an ideal $\lambda/4$ waveplate by letting $\varphi = \pi/2$. If the light is then sent through an analyzing polarizer at an angle γ, the resulting Stokes vector is

$$\boldsymbol{S}'' = \frac{1}{2}\begin{pmatrix} 1 & \cos 2\gamma & \sin 2\gamma & 0 \\ \cos 2\gamma & \cos^2 2\gamma & \sin 2\gamma\cos 2\gamma & 0 \\ \sin 2\gamma & \sin 2\gamma\cos 2\gamma & \sin^2 2\gamma & 0 \\ 0 & 0 & 0 & 0 \end{pmatrix} \vec{S}' \tag{B.18}$$

and the transmitted intensity is

$$\begin{aligned} I(\theta,\gamma) &= \frac{1}{2}\left(S_0'' + S_1''\right) \\ &= \frac{1}{2}\left[\left(S_0 + \frac{S_1}{2}\cos 2\gamma + \frac{S_2}{2}\sin 2\gamma\right) + S_3\cos 2\gamma\sin 2\theta - S_3\sin 2\gamma\cos 2\theta\right. \\ &\qquad \left. + \left(\frac{S_2}{2}\cos 2\gamma + \frac{S_1}{2}\sin 2\gamma\right)\sin 4\theta + \left(\frac{S_1}{2}\cos 2\gamma - \frac{S_2}{2}\sin 2\gamma\right)\cos 4\theta\right] \end{aligned} \tag{B.19}$$

©1999 NRC Canada

With a discrete Fourier analysis, the angle γ can be extracted from the fit. As before, we have

$$C_2 = \frac{1}{16}\sum_{i=1}^{16} I(\theta_i)\sin 2\theta_i = \frac{S_3\cos 2\gamma}{4} \tag{B.20}$$

$$C_3 = \frac{1}{16}\sum_{i=1}^{16} I(\theta_i)\cos 2\theta_i = \frac{-S_3\sin 2\gamma}{4} \tag{B.21}$$

and

$$\gamma = -\frac{1}{2}\tan^{-1}\left(\frac{C_3}{C_2}\right) \tag{B.22}$$

Thus, we can align the analyzing polarizer along $\hat{z}$, and then use this fit to determine the angle between the analysis polarizer and the fast axis of the $\lambda/4$ plate. Note that the angle γ is actually the difference in angle between the $\hat{z}$ axis and the fast axis of the $\lambda/4$ plate at the *initial* position of the stepper motor, θ_1. The true angular difference between the fast axis and the $\hat{z}$ axis as the $\lambda/4$ plate is rotated is $\theta_i - \gamma$, and we properly account for this once γ is determined. Note also that our assumption $\varphi = \pi/2$ has no effect on our determination of γ since the actual retardance cancels in (B.22). We also mention that the angle γ is correctly determined for elliptically polarized light, but when the light becomes linearly polarized $C_3 \to 0$ and the expression for γ diverges.

We now consider the case of an imperfect $\lambda/4$ ($\varphi \neq \pi/2$). Having determined γ and corrected the rotation angles appropriately ($\theta_i' = \theta_i - \gamma$), we again use (B.17*a*). After transmission through the analysis polarizer along $\hat{z}$, the intensity is

$$I(\theta') = \frac{1}{2}\left\{\left[S_0 + \frac{S_1}{2}(1+\cos\varphi)\right] + \left[\frac{S_1}{2}(1-\cos\varphi)\right]\cos 4\theta' + \left[\frac{S_2}{2}(1-\cos\varphi)\right]\sin 4\theta' - [S_3\sin\varphi]\sin 2\theta'\right\} \tag{B.23}$$

The discrete Fourier analysis gives

$$S_0 + \frac{S_1}{2}(1+\cos\varphi) = \frac{1}{8}\sum_{i=1}^{16} I(\theta_i') \tag{B.24}$$

$$\frac{S_1}{2}(1-\cos\varphi) = \frac{1}{4}\sum_{i=1}^{16} I(\theta_i')\cos 4\theta_i' \tag{B.25}$$

$$\frac{S_2}{2}(1-\cos\varphi) = \frac{1}{4}\sum_{i=1}^{16} I(\theta_i')\sin 4\theta_i' \tag{B.26}$$

$$S_3\sin\varphi = \frac{1}{4}\sum_{i=1}^{16} I(\theta_i')\sin 2\theta_i' \tag{B.27}$$

and we can make the identifications

$$\epsilon_z^2 = \frac{S_0 + S_1}{2} \tag{B.28}$$

©1999 NRC Canada

$$\frac{\epsilon_{\mathrm{R}}}{\epsilon_z} = \frac{S_2}{S_0 + S_1} \tag{B.29}$$

$$\frac{\epsilon_I}{\epsilon_z} = \frac{S_3}{S_0 + S_1} \tag{B.30}$$

If the analysis polarizer is along $\hat{x}$, then slightly different equations result, but the measured values of ϵ_z^2, $\epsilon_{\mathrm{R}}/\epsilon_z$, and ϵ_I/ϵ_z are the same. Also, a Jones matrix formulation was performed for the rotating $\lambda/4$ plate technique, and the results agree.

Finally, we compare the measured degree of polarization with the expected, perfect polarization. The degree of polarization is defined as

$$P = \frac{\sqrt{S_1^2 + S_2^2 + S_3^2}}{S_0} = \frac{I_{\mathrm{polarized}}}{I_{\mathrm{total}}} \tag{B.31}$$

and $P = 1$ for perfectly polarized light. We can extract all four Stokes parameters, or we can make the assumption that we have perfectly polarized light and define $S_0' = \sqrt{S_1^2 + S_2^2 + S_3^2}$. Using S_0' in the above expressions for ϵ_z^2, $\epsilon_{\mathrm{R}}/\epsilon_z$, and ϵ_I/ϵ_z gives slightly different results ($\sim 0.1\%$ difference) than if we use S_0, and the discrepancy is discussed below.

Limitations and accuracy

The rotating polarizer technique, aside from its inability to measure phases, is a fairly robust method. The most important consideration is to obtain a high-quality polarizer. We tested polarizers by comparing the signal intensity for two positions differing by 180^{o}. Although for an ideal polarizer these signal intensities should be equal, we always found discrepancies due to the following sources: absorbing or scattering centers either in the calcite or in the coatings on the surfaces; polarization-dependent reflections from surfaces; and an angular dependence of Fresnel coefficients. Another difficulty we had with the rotating polarizer technique was in positioning the transmission axis of the polarizer relative to the PNC coordinate system. Since the stepper-motor gears tended to lock up at certain discrete positions, this positioning was limited to $\pm\ 0.5^{\mathrm{o}}$.

In contrast, the rotating $\lambda/4$ plate technique avoids the problem of the initial angle alignment with the PNC coordinate system, for the angle between the polarizer and the $\lambda/4$ plate is determined from the fits. However, other problems affect the $\lambda/4$ plate technique, such as scattering centers in the waveplate or on the surface coatings and any variation in retardance across the waveplate. We found about a 0.1% difference in the values $\epsilon_{\mathrm{R}}/\epsilon_z$ and ϵ_I/ϵ_z when calculated assuming perfectly polarized light as compared to when calculated using all four Stokes parameters. If either the magnitude of the retardance or the direction of the birefringence axes varies across the surface, this leads to a false indication of partially polarized light. Near the edge of the waveplates, where there is stress due to mounting, this effect is most prominent. Also, if the retardance value is incorrectly determined for a waveplate, this leads to a false indication of partially polarized light.

The final fractional uncertainty for our measurements of ϵ_I/ϵ_z during the PNC experiment was around 0.1% or less. We made three comparisons to confirm this accuracy. For the PNC experiment, we used two different $\lambda/4$ plates which had different values of retardance, φ. One of the plates was made of Mica (Karl Lambrecht, Inc.), the other from a thin polymer layer sandwiched between two pieces of fused silica (Meadowlark Optics). Both were AR-coated on both sides. The two $\lambda/4$ plates gave measurements of ϵ_I/ϵ_z that agreed to 0.1%. We also compared these values with the measurement obtained from the rotating polarizer technique and again observed 0.1% agreement.

Comparison of the rotating polarizer technique with the rotating $\lambda/4$ plate technique is important because the measured intensity $I(\theta)$ is very different for these two situations. For the PNC experiment, circular (or elliptical) polarization is always used. Since for the rotating polarizer method, $I(\theta) \simeq$ constant when $\epsilon_I/\epsilon_z \simeq 1$, factors such as linearity of the photodiode do not affect the results significantly.

©1999 NRC Canada

However, for the rotating $\lambda/4$ plate method, $I(\theta)$ varies from $I_{\max}$ to zero, so that photodiode linearity is a major factor. Also, the Fourier spectrum is different between the two methods. Finally, we also used a measured atomic quantity to evaluate the performance of the polarization measurements [50].

Appendix C. Pure Stark-induced 6S–7S transition rate including the effect of misaligned fields

Here the following notation is used:

- $e, p, b, m, a = \pm 1$ are the flipping parameters for the e,p,b,m, and a reversals.
- $f = \pm 1$ is the hyperfine flipping parameter: $\Delta F = +1 \rightarrow \Delta F = -1$.
- The terms shown here are fractional modulations of the transition rate.
- The $\Delta F = 0,\ \Delta m = \pm 1$ terms and the $\Delta F = \pm 1,\ \Delta m = 0$ (hyperfine mixed) terms are given in ref. 27.
- ϵ_{R} can have a flipping part ($p\epsilon_{\mathrm{R}}$) and a nonflipping part ($\Delta\epsilon_{\mathrm{R}}$).
- Substitution of $aA_{i=x,y,z}$ for bB_i leads to terms from the OP magnetic field.

$\boldsymbol{\Delta F = 0,\ \Delta m = 0}$:

$$\begin{aligned}\frac{R}{\alpha^2 E_x^2 \mid \epsilon_x \mid^2} = &\left(1 + 2e\frac{\Delta E_x}{E_x} + 2e\frac{\Delta E_x}{E_x}\frac{\epsilon_{\mathrm{R}}\epsilon_z}{\mid \epsilon_x \mid^2}\right) \times (2F+1) \\ &+ 2\frac{\beta}{\alpha}\left\{-\left(1 + 2e\frac{\Delta E_x}{E_x}\right)\left(\frac{B_y}{B} + b\frac{\Delta B_y}{B}\right)\frac{p\epsilon_I\epsilon_z}{\mid \epsilon_x \mid^2} + ep\frac{E_y}{E_x}\frac{\Delta E_z}{E_x}\frac{\epsilon_I\epsilon_z}{\mid \epsilon_x \mid^2}\right. \\ &\left. -\left(\frac{E_y}{E_x} + e\frac{\Delta E_y}{E_x}\right)\left(\frac{B_x}{B} + b\frac{\Delta B_x}{B}\right)\frac{p\epsilon_I\epsilon_z}{\mid \epsilon_x \mid^2}\right\} \\ &\times \left[C_{Fm}^{Fm} + bf(\delta_6 + \delta_7)\sum_m \left(C_{Fm}^{F'm}\right)^2\right] \end{aligned} \tag{C.1}$$

$\boldsymbol{\Delta F = \pm 1,\ \Delta m = \pm 1}$:

$$\begin{aligned}\frac{R}{\beta^2 E_x^2 {\epsilon_z}^2} = &\left\{1 + 2e\frac{\Delta E_x}{E_x} - 2e\frac{\Delta E_x}{E_x}\frac{\epsilon_{\mathrm{R}}}{\epsilon_z} - 2epmab\frac{E_y}{E_x}\frac{\Delta E_z}{E_x}\frac{\epsilon_I}{\epsilon_z}\right. \\ &+ 2\left(\frac{B_x^2}{B^2} + 2b\frac{B_x\Delta B_x}{B^2}\right) - 2pmab\left(\frac{E_y}{E_x} + e\frac{\Delta E_y}{E_x}\right)\left(\frac{B_x}{B} + b\frac{\Delta B_x}{B}\right)\frac{\epsilon_I}{\epsilon_z} \\ &\left. - 2\left(\frac{E_y}{E_x} + e\frac{\Delta E_y}{E_x}\right)\left(\frac{B_y}{B} + b\frac{\Delta B_y}{B}\right)\frac{\epsilon_{\mathrm{R}}}{\epsilon_z}\right\} \\ &\times \left[\left(C_{Fm}^{F'm'}\right)^2 + 2bfC_{Fm}^{F'm'}\left(\delta_6 C_{Fm}^{F'm}C_{F'm}^{F'm'} - \delta_7 C_{Fm}^{Fm'}C_{Fm'}^{F'm'}\right)\right] \end{aligned} \tag{C.2}$$

©1999 NRC Canada